

<sup>1</sup> Study of the multi-strange resonance  $\Xi(1530)^0$  production  
<sup>2</sup> with ALICE at the LHC energies

<sup>3</sup> Jihye Song

## **4** Contents

<b>5</b>	<b>List of Figures</b>	<b>4</b>
<b>6</b>	<b>List of Tables</b>	<b>8</b>
<b>7</b>	<b>1 The physics of relativistic heavy-ion collisions</b>	<b>9</b>
8	1.1 Standard model . . . . .	9
9	1.2 QCD and Quark-Gluon plasma . . . . .	10
10	1.3 Heavy Ion Collisions . . . . .	16
<b>11</b>	<b>2 Theoretical models</b>	<b>19</b>
12	2.1 Statistical-Thermal model . . . . .	19
13	2.1.1 Calculations . . . . .	21
14	2.1.2 Results and comparison with data . . . . .	23
15	2.2 EPOS, UrQMD . . . . .	25
<b>16</b>	<b>3 Production of resonance with strangeness</b>	<b>27</b>
17	3.1 Strange quark and hyperons . . . . .	29
18	3.2 Resonance production . . . . .	31
<b>19</b>	<b>4 A Large Ion Collider Experiment at the LHC</b>	<b>33</b>
20	4.1 The Large Hadron Collider . . . . .	33
21	4.2 The ALICE project . . . . .	36
22	4.2.1 ALICE detector . . . . .	36
23	4.2.2 Data Acquisition (DAQ) and trigger system . . . . .	46
24	4.2.3 ALICE offline software frame work . . . . .	48
<b>25</b>	<b>5 Measurement of <math>\Xi(1530)^0</math> production in p-Pb and Pb-Pb</b>	<b>50</b>
26	5.1 $\Xi(1530)^0$ -reconstruction . . . . .	50
27	5.1.1 Data sample and event selection . . . . .	50
28	5.1.2 Track and topological selection . . . . .	54
29	5.1.3 Particle identification . . . . .	57
30	5.1.4 Signal extraction . . . . .	60
31	5.2 Efficiency correction . . . . .	69
32	5.3 Corrected $p_T$ -spectra . . . . .	72
33	5.4 Systematic uncertainties . . . . .	74
34	5.5 $\Xi(1530)^0$ transverse momentum spectra . . . . .	79
<b>35</b>	<b>6 Further results and discussion</b>	<b>82</b>
36	6.1 Mean transverse momentum . . . . .	82
37	6.2 Particle yield ratios . . . . .	86

38	6.2.1 Integrated yield ratios of excited to ground-state hadrons . . . . .	86
39	6.3 Integrated yield ratios to pion . . . . .	89
40	<b>References</b>	<b>93</b>

<sup>41</sup> **List of Figures**

42	1	QCD coupling constant as a function of momentum transfer. Experimental data and also theoretical prediction are presented. [1] . . . . .	13
43	2	Phase diagram of partonic and hadronic matter. The chemical freeze out points are determined from thermal models fit to heavy ion data at SIS, AGS, and SPS energies. ( <a href="http://na49info.web.cern.ch/na49info/Public/Press/findings.html">http://na49info.web.cern.ch/na49info/Public/Press/findings.html</a> )	15
44	3	The time evolution of a high energy heavy ion collision. [2] . . . . .	16
45	4	Hydrodynamic evolution of a heavy ion collision with and without the for- mation of a QGP. . . . .	18
46	5	Grand canonical thermal fit of 0-10% central Pb-Pb collisions, with 3 models (THERMUS, GSI, SHARE). . . . .	19
47	6	Ratio of baryonic and mesonic resonances over their stable partner as a function of temperature. . . . .	24
48	7	Ratio of resonances over their stable partner as a function of $\sqrt(s)$ . . . . .	25
49	8	The $J^P = 1/2^+$ ground state baryon octet . . . . .	28
50	9	The $J^P = 3/2^+$ baryon decuplet . . . . .	28
51	10	Enhancements in the rapidity range $ y  < 0.5$ as a function of the mean number of participants $\langle N_{part} \rangle$ , showing LHC (ALICE, full symbols), RHIC and SPS (open symbols) data. Boxes on the dashed line at unity indicate statistical and systematic uncertainties on the pp or p-Be reference. Error bars on the data points represent the corresponding uncertainties for all the heavy-ion measurements and those for p-Pb at the SPS. . . . .	30
52	11	Hadronic phase . . . . .	31
53	12	The CERN accelerator complex [3] . . . . .	34
54	13	The ALICE detector . . . . .	38
55	14	Schematic view of the ITS [4] . . . . .	39
56	15	Track impact parameter resolution in the transverse plane ( $r\phi$ ) vs $p_T$ for charged particle . . . . .	40
57	16	Schematic view of the TPC . . . . .	41
58	17	Specific energy loss ( $dE/dx$ ) in the TPC vs. particle momentum in Pb-Pb collisions at $\sqrt{s_{NN}} = 2.76$ TeV. The lines show the parametrisations of the expected mean energy loss. . . . .	42
59	18	Correlation between the sum and difference of signal times in V0A and V0C. Three classes of events collisions at (8.3 ns, 14.3 ns), background from Beam 1 at (-14.3 ns, -8.3 ns), and background from Beam 2 at (14.3 ns, 8.3 ns) can be clearly distinguished. . . . .	44
60	19	Distribution of the V0 amplitude (sum of V0A and V0C in top, V0A in bottom). The inset shows a magnified version of the most peripheral region.	45
61	20	The overall architecture of the ALICE DAQ and the interface to the HLT system. . . . .	46

81	21	Schematic view of the AliRoot framework . . . . .	49
82	22	Vertex-z coordinate distribution of the accepted events in p–Pb collision(Left) and in Pb–Pb collisions(Right). The red dashed line indicates vertex cut . . . . .	52
83	23	Multiplicity distribution of accepted events in p–Pb collision in percentile. The each color and labels define the four intervals in which the analysis is performed. . . . .	52
87	24	Centrality distribution of three different trigger classes. . . . .	53
88	25	Sketch of the decay modes for $\Xi^{*0}$ and depiction of the track and topological selection criteria. . . . .	55
90	26	TPC $dE/dx$ as function of transverse momentum for total (top) and selected first emitted $\pi$ in $3\sigma$ (bottom) . . . . .	57
91	27	TPC $dE/dx$ as function of transverse momentum for total (top) and selected second emitted $\pi$ in $3\sigma$ (bottom) . . . . .	57
94	28	TPC $dE/dx$ as function of transverse momentum for total (top) and selected last emitted $\pi$ in $3\sigma$ (bottom) . . . . .	58
96	29	TPC $dE/dx$ as function of transverse momentum for total (top) and selected proton in $3\sigma$ (bottom) . . . . .	58
99	30	TPC $dE/dx$ as function of transverse momentum for total (top) and selected first emitted $\pi$ in $3\sigma$ (bottom) . . . . .	58
100	31	TPC $dE/dx$ as function of transverse momentum for total (top) and selected second emitted $\pi$ in $3\sigma$ (bottom) . . . . .	59
102	32	TPC $dE/dx$ as function of transverse momentum for total (top) and selected last emitted $\pi$ in $3\sigma$ (bottom) . . . . .	59
104	33	TPC $dE/dx$ as function of transverse momentum for total (top) and selected proton in $3\sigma$ (bottom) . . . . .	60
106	34	The $\Xi^\mp\pi^\pm$ invariant mass distribution (Same-event pairs) in $1.8 < p_T < 2.2 \text{ GeV}/c$ and for the multiplicity class 20-40%. The background shape, using pairs from different events (Mixed-event background), is normalised to the counts in $1.49 < M_{\Xi\pi} < 1.51 \text{ GeV}/c^2$ and $1.56 < M_{\Xi\pi} < 1.58 \text{ GeV}/c^2$ . . . . .	61
109	35	The $\Xi^\mp\pi^\pm$ invariant mass distribution (Same-event pairs) in $3.0 < p_T < 3.5 \text{ GeV}/c$ and for the centrality class 0-10%. The background shape, using pairs from different events (Mixed-event background), is normalised to the counts in $1.49 < M_{\Xi\pi} < 1.51 \text{ GeV}/c^2$ and $1.56 < M_{\Xi\pi} < 1.58 \text{ GeV}/c^2$ . . . . .	62
111	36	The invariant mass distribution after subtraction of the mixed-event background in p–Pb collisions. The solid curve represents the combined fit, while the dashed line describes the residual background. . . . .	63
113	37	The invariant mass distribution after subtraction of the mixed-event background in Pb–Pb collisions. The solid curve represents the combined fit, while the dashed line describes the residual background. . . . .	64
120	38	$\sigma$ fit parameters as a function of $p_{T\text{in}}$ MB in p–Pb collisions (top) and in Pb–Pb collisions (bottom). . . . .	66

122	39	$\Xi(1530)^0$ -mass obtained from fit of the Voigtian peak as a function of $p_{\text{T}}$ in each multiplicity classes in p–Pb collisions (top) and the different centrality classes in Pb–Pb (bottom). . . . .	67
123			
124	40	$\Xi(1530)^0$ -raw spectra obtained from fit of the Voigtian peak and a polynomial residual background for different multiplicities in p–Pb collisions (top) and Pb–Pb collisions (bottom). Only the statistical error is reported. . . . .	68
125			
126	41	$\Xi(1530)^0$ -raw spectra obtained from fit of the Voigtian peak and a polynomial residual background for different multiplicities. Only the statistical error is reported. . . . .	69
127			
128	42	Real corrected $\Xi(1530)^0$ spectrum (black) for the minimum bias with Levy fit (black curve). Also shown are the unweighted generated (blue) and reconstructed (red) $\Xi(1530)^0$ spectra. . . . .	70
129			
130	43	Efficiency as a function of $p_{\text{T}}$ in minimum bias events in p–Pb collisions. . . . .	71
131			
132	44	Efficiency as a function of $p_{\text{T}}$ in different centrality classes in Pb–Pb collisions . . . . .	72
133			
134	45	Corrected $p_{\text{T}}$ -spectra of $\Xi(1530)^0$ in NSD and different multiplicity classes in p–Pb collisions. . . . .	73
135			
136	46	Corrected $p_{\text{T}}$ -spectra of $\Xi(1530)^0$ in different centrality classes in Pb–Pb collisions. . . . .	73
137			
138	47	Summary of the contributions to the systematic uncertainty in minimum bias events in p–Pb collisions. The dashed black line is the sum in quadrature of all the contributions. . . . .	77
139			
140	48	Systematic uncertainties for each multiplicity classes in p–Pb collisions. . . . .	77
141			
142	49	Summary of the contributions to the systematic uncertainty in minimum bias events in Pb–Pb collisions. The dashed black line is the sum in quadrature of all the contributions. . . . .	78
143			
144	50	Systematic uncertainties for each multiplicity classes. . . . .	78
145			
146	51	Corrected yields as function of $p_{\text{T}}$ in NSD events and multiplicity dependent event classes in p–Pb collision system. Statistical uncertainties are presented as bar and systematical uncertainties are plotted as boxes. . . . .	80
147			
148	52	Corrected yields as function of $p_{\text{T}}$ in different centrality classes in Pb–Pb collision system. Statistical uncertainties are presented as bar and systematical uncertainties are plotted as boxes. . . . .	81
149			
150	53	Mean transverse momenta $\langle p_{\text{T}} \rangle$ of $\Lambda$ , $\Xi^-$ , $\Sigma^{*\pm}$ , $\Xi^{*0}$ and $\Omega^-$ in p–Pb collisions at $\sqrt{s_{\text{NN}}} = 5.02$ TeV as a function of mean charged-particle multiplicity density $\langle dN_{\text{ch}}/d\eta_{\text{lab}} \rangle$ , measured in the pseudorapidity range $ \eta_{\text{lab}}  < 0.5$ . The results for $\Lambda$ , $\Xi^-$ and $\Omega^-$ are taken from [5, 6, 7]. Statistical and systematic uncertainties are represented as bars and boxes, respectively. The $\Omega^-$ and $\Xi^-$ points in the 3rd and 4th lowest multiplicity bins are slightly displaced along the abscissa to avoid superposition with the $\Xi(1530)^0$ points. . . . .	83
151			
152			
153			
154			
155			
156			
157			
158			
159			
160			

161	54	Mass dependence of the mean transverse momenta of identified particles for the 0 – 20% V0A multiplicity class and with $-0.5 < y_{\text{CMS}} < 0$ in p– Pb collisions at $\sqrt{s_{\text{NN}}} = 5.02$ TeV [5, 7], and in minimum-bias pp collisions at $\sqrt{s} = 7$ TeV [8] with $ y_{\text{CMS}}  < 0.5$ . Additionally, $D^0$ and $J/\psi$ results are plotted. The $D^0$ and $J/\psi$ were measured in different rapidity ranges: $ y_{\text{CMS}}  < 0.5$ [9] ( $ y_{\text{CMS}}  < 0.9$ [10]) for $D^0$ ( $J/\psi$ ) in pp and $-0.96 < y_{\text{CMS}} <$ $0.04$ [9] ( $-1.37 < y_{\text{CMS}} < 0.43$ [11]) for $D^0$ ( $J/\psi$ ) in p–Pb. Note also that the results for $D^0$ and $J/\psi$ in p–Pb collisions are for the 0–100% multiplicity class. . . . .	84
170	55	Ratio of $\Xi(1530)^0$ to $\Xi^-$ measured in pp [8], p–Pb [5, 7] and Pb–Pb collisions as a function of $\langle dN_{\text{ch}}/d\eta_{\text{lab}} \rangle$ measured at midrapidity. Statistical uncer- tainties (bars) are shown as well as total systematic uncertainties (hollow boxes) and systematic uncertainties uncorrelated across multiplicity (shaded boxes). A few model predictions are also shown as lines at their appropriate abscissa. . . . .	87
176	56	Ratio of $\rho/\pi(\text{Up})$ , $K^*/K$ , $\phi/K(\text{Left bottom})$ and $\Lambda^*/\Lambda$ with system size measured at mid-rapidity. Statistical uncertainties (bars) are shown as well as total systematic uncertainties (hollow boxes) and systematic uncertainties uncorrelated across multiplicity (shaded boxes). A few model predictions are also shown as lines at their appropriate abscissa. . . . .	88
181	57	Ratio of $\Xi(1530)^0$ to $\pi^\pm$ , measured in pp [12] and p–Pb [8] collisions, as a function of the average charged particle density ( $\langle dN_{\text{ch}}/d\eta_{\text{lab}} \rangle$ ) measured at mid-rapidity. Statistical uncertainties (bars) are shown as well as total systematic uncertainties (hollow boxes) and systematic uncertainties uncor- related across multiplicity (shaded boxes). A few model predictions are also shown as lines at their appropriate abscissa. . . . .	90
187	58	Particle yield ratios to pions of strange and multi-strange hadrons normal- ized to the values measured in pp collisions, both in pp and in p–Pb colli- sions. The common systematic uncertainties cancel in the double-ratio. The empty boxes represent the remaining uncorrelated uncertainties. The lines represent a simultaneous fit of the results with the empirical scaling formula in Equation ???. . . . .	91
193	59	$p_{\text{T}}$ -integrated yield ratios of strange and multi-strange hadrons to $(\pi^+ + \pi^-)$ as a function of $\langle dN_{\text{ch}}/d\eta_{\text{lab}} \rangle$ measured in the rapidity interval $ \eta  < 0.5$ . The empty and dark-shaded boxes show the total systematic uncertainty and the contribution uncorrelated across multiplicity bins, respectively. The values are compared to calculations from MC models and to results obtained in Pb–Pb and p–Pb collisions at the LHC. . . . .	92

<sup>199</sup> **List of Tables**

200	1	Constituents of matter in the Standard Model . . . . .	9
201	2	Fundamental forces . . . . .	10
202	3	Parameters used in the thermal-model calculations. . . . .	20
203	4	Properties of particles used in the ratio calculations. . . . .	22
204	5	Difference of mass ( $\Delta M$ ), baryon number ( $\Delta B$ ), strangeness ( $\Delta S$ ) and charge ( $\Delta Q$ ) of the ratios. . . . .	23
205	6	Quantum numbers and masses associated to the three lighter quarks: u, d and s . . . . .	27
206	7	Lifetime of hadronic resonances . . . . .	29
207	8	Number of accepted and analyzed events per multiplicity/centrality interval	54
208	9	Track selections common to all decay daughters and primary track selections applied to the charged pions from decays of $\Xi^{*0}$ . . . . .	54
209	10	Topological and track selection criteria. . . . .	55
210	11	Summary of the systematic uncertainties on the differential yield, $d^2N/(dp_T dy)$ . Minimum and maximum values in all $p_T$ intervals and multiplicity classes in p–Pb, centrality classes in Pb–Pb are shown for each source. . . . .	79

216 **1 The physics of relativistic heavy-ion collisions**

217 The main objective of relativistic heavy ion physics is to study the nuclear matter under  
 218 extreme conditions which are high temperature and energy density. In these conditions,  
 219 the Standard Model anticipates that the nuclear matter undergo a new phase, where the  
 220 quarks and the gluons are expected to be de-confined called quark-gluon plasma (QGP)  
 221 and to freely move.

222 **1.1 Standard model**

223 If one have question "what the world is made of", our current answer to the question is  
 224 Standard Model (SM) families [13] reported in Table 1. The SM explains the way how  
 225 those basic blocks of matter interact and how they are ruled by four fundamental forces.  
 226 In this explanation, the matter consist of 12 particles, which have a spin of 1/2 (fermions)  
 227 and can be categorized in accordance with way how they interact or equivalently to what  
 228 charges they carry. The basic particles are six quarks (up, down, charm, strange, top and  
 229 bottom) that carry fractional charge of  $+\frac{2}{3}e$  or  $-\frac{1}{3}e$ , and six leptons (electron, electron  
 230 neutrino, muon, muon neutrino, tau, tau neutrino) with integer charge.

Family	Quarks			Leptons		
	Name	Charge[e]	Mass	Name	Charge[e]	Mass
1	u	2/3	$2.2^{+0.6}_{-0.4}$ MeV/c <sup>2</sup>	$e^-$	-e	0.511 MeV/c <sup>2</sup>
	d	-1/3	$4.7^{+0.5}_{-0.4}$ MeV/c <sup>2</sup>	$\nu_e$	0	< 2 eV/c <sup>2</sup>
2	c	2/3	$1.27^{+0.03}$ GeV/c <sup>2</sup>	$\mu^-$	-e	105.66 MeV/c <sup>2</sup>
	s	-1/3	$96^{+8}_{-4}$ MeV/c <sup>2</sup>	$\nu_\mu$	-e	< 0.19 eV/c <sup>2</sup>
3	t	2/3	$173.21 \pm 1.22$ GeV/c <sup>2</sup>	$\tau^-$	-e	1.777 GeV/c <sup>2</sup>
	b	-1/3	$4.18^{+0.04}_{-0.03}$ GeV/c <sup>2</sup>	$\nu_\tau$	-e	< 18.2 MeV/c <sup>2</sup>

Table 1: Constituents of matter in the Standard Model

231 The interactions between elementary particles are described by the exchange of gauge  
 232 bosons(gluon, photon, Z-boson, W-boson), reported in Table 2 together with their relative  
 233 coupling strengths. The leptons are governed the weak force and the electromagnetic force.  
 234 Quarks have color property which is the character of charge in the strong force. The color  
 235 could take one out of three possible values (conventionally red, green and blue). The color  
 236 can not be appeared freely. After they are confined they come out in the form of hadron  
 237 which are colorless. Further explaination on color is described in Section 1.2. Then, the  
 238 hadrons are grouped into baryon and mesons. Baryons consist of three quarks,  $qqq$  or  $(\bar{q}\bar{q}\bar{q})$   
 239 while mesons consist of two quarks ( $q\bar{q}$ ).

240 The models that describe these interactions are listed as follows:

241

Force	Strength	Gauge Boson(s)	Applies on
Strong force	1	8 Gluons( $g$ )	Quarks, gluons
Electromagnetic force	$\simeq 10^{-2}$	Photon ( $\gamma$ )	All charged particles
Weak force	$\simeq 10^{-7}$	$W^\pm, Z^0$	Quarks, leptons
Gravitation	$\simeq 10^{-39}$	Gravitons	All particles

Table 2: Fundamental forces

242     **Quantum Electro-Dynamics (QED)** is a quantum field theory of the electromagnetic  
 243 force and describes how light and matter interact. This is the first theory where  
 244 full agreement between quantum mechanics and special relativity is achieved. It explains  
 245 mathematically not only all interactions of light with matter but also those of charged  
 246 particles with one another.

247     **Electroweak Theory (EW)** is the unified description of two of the four known fundamental  
 248 interactions of nature: electromagnetism and the weak interaction. The first  
 249 measurement of the existence of the weak bosons  $W^+$ ,  $W^-$  and  $Z^0$  was performed in 1983,  
 250 when they were produced and directly observed in  $Spp\bar{S}$  collisions at CERN.

252     **Quantum Chromo-dynamics (QCD)** is the theory of the strong interaction (color  
 253 force), describing the interactions between quarks and gluons which make up the hadrons.  
 255 Starting from the classification of the large amount of particles discovered during the fifties,  
 256 the original idea of the quark model by Gell-Mann (Nobel Prize in 1969) has been developed  
 257 during the sixties until 1973, when David J. Gross, H. David Politzer and Frank Wilczek  
 258 discovered the asymptotic freedom property of the strong nuclear interaction.

## 259     1.2 QCD and Quark-Gluon plasma

260 As the number of known particle species became large, the idea that these could be the  
 261 elementary constituents of matter was replaced by the notion that these species could in  
 262 fact be composite objects made up of fewer, more elementary particles, in a similar way to  
 263 what had already happened to the elements of Mendeleev's Periodic Table. The original  
 264 idea by Gell-Mann (1964) was that the hadrons could be obtained as combination of the  
 265 fundamental representation of an  $SU_f(3)$  group, where three different flavors of quark ( $q$   
 266 = u, d, s) combine to build mesons ( $q\bar{q}$ ) and hadrons ( $qqq$ ). However, when cataloging  
 267 hadrons using the  $SU_f(3)$  group, there are anomalous states, such as the  $\Omega^-(sss)$  and the  
 268  $\Delta^{++}(uuu)$ , that are combinations of three quarks of the same flavor, in clear contrast  
 269 with the Pauli exclusion principle for fermions. A solution was proposed in 1965 by Moo-  
 270 Young Han with Yoichiro Nambu and Oscar W. Greenberg, who independently solved the  
 271 problem by proposing that quarks possess an additional  $SU(3)$  gauge quantum number,

272 later called color charge. This new quantum number may assume three states, represented  
 273 by the three primary colors: red, green and blue (denoted symbolically by R, G and B,  
 274 respectively). The introduction of this new quantum number also provides an explanation  
 275 to other empirical evidence, such as the fact that no  $qq$ ,  $\bar{q}q$  or the single quark have never  
 276 been observed directly. On the other hand, the existence of color charge gives rise to the  
 277 possible existence of differently colored states for each particle. Thus, we could have many  
 278 states for the proton, such as  $u_R u_G d_B$ ,  $u_R u_G d_G$ ,  $u_B u_R d_R$ , and so on. The fundamental  
 279 rule that solves such contradictions is that all the particle states observed in nature are  
 280 "colorless" or "white" (or, to be more precise, unchanged under  $SU_c(3)$  rotations). The  
 281 dynamics of the quarks and gluons are controlled by the gauge invariant QCD Lagrangian:

$$\mathcal{L}_{QCD} = \underbrace{i\delta_{ij}\bar{\Psi}_q^i\gamma^\mu\partial_\mu\Psi_q^j}_{\mathcal{L}_1} + \underbrace{g_s\bar{\Psi}_q^i\gamma^\mu t_{ij}^a A_\mu^a\Psi_q^j}_{\mathcal{L}_2} + \underbrace{m_q\bar{\Psi}_q^i\Psi_q^j}_{\mathcal{L}_3} + \underbrace{\frac{1}{4}F_{\mu\nu}^a F^{a\mu\nu}}_{\mathcal{L}_4} \quad (1)$$

282 where the coloured gluon field tensor,  $F_{\mu\nu}^a$  (with color index  $a$ ) and the squared gauge  
 283 coupling parameter,  $g_s^2$  (associated to the strong coupling constant  $\alpha_s$ ) are defined as:

$$F_{\mu\nu}^a = \partial_\mu A_\nu^a - \partial_\nu A_\mu^a + g_s f^{abc} A_\mu^b A_\nu^c \quad (2)$$

284 and

$$g_s^2 = 4\pi\alpha_s \quad (3)$$

285 where:

- $\Psi_q^i$ : the quark field with flavor q and color index  $i \in [1;3]$ , such as  $\Psi_q = (\Psi_{qR}, \Psi_{qG}, \Psi_{qB})^T$  and  $A_\mu^a$  is the gluon field with color index  $a$  (adjoint representation)
- $\gamma^\mu$ : Dirac matrices that express the vector nature of the strong interaction, with  $\mu$  being the Lorentz vector associated index
- $m_q$ : quark mass, a priori not equal to zero (resulting from the Higgs mechanism or equivalent)
- $t_{ij}^a$ : generator matrices of the group  $SU_c(3)$ , proportional to the Gell-Mann matrices, that perform revolutions in color space, representing interaction of quarks and gluons
- $f^{abc}$ : structure constant of QCD

295 Each of the four terms of the QCD Lagrangian expresses and aspect of the interaction,  
 296 specifically:

- 297 •  $\mathcal{L}_1$ : gives the kinetic energy of the quark field  $\Psi_q^i$

- 298     •  $\mathcal{L}_2$ : gives the interaction between quarks (fermions) and gluons (the bosons of the  
299       interaction)
- 300     •  $\mathcal{L}_3$ : gives the mass of the quarks
- 301     •  $\mathcal{L}_4$ : gives the kinetic energy of the gluons

302     The terms of this equation, together with the fundamental parameters  $\alpha_s$  and  $m_q$ ,  
303     summarize in just one expression all the features of the strong interaction. The first three  
304     terms describe the free propagation of quarks and gluons and the quark-gluon interaction.  
305     The remaining two terms show the presence of three and four gluon vertices in QCD and  
306     reflect the fact that gluons themselves carry color charge. This is a consequence of the non-  
307     abelian<sup>4</sup> character of the gauge group. This peculiarity of the QCD interaction imposes the  
308     evolution of the strong coupling constant,  $\alpha_s$ . The corresponding trend has been measured  
309     experimentally, and compared in Figure 1 with predictions. A practical consequence of  
310     this behavior is that the corresponding potential has a completely different shape than the  
311     other fundamental interactions and can be expressed by the following equation:

$$V(r) = -4 \frac{\alpha_s}{3r} + kr \quad (4)$$

312     where  $r$  is the separation distance between the two quarks and  $k$  is a constant that is  
313     approximately 1 GeV/fm.

314     Three are main properties of the QCD interaction:

315     **Confinement** At large distances between quarks and gluons (i.e. small values of trans-  
316     ferred momentum  $Q$  in Figure 1) the coupling constant is large and the associated force  
317     is strong enough to keep these elementary con- stituents (usually called partons) confined  
318     in bounded states. As expressed in the Equation 4, the attractive potential increases with  
319     the increasing of the relative distance between the two partons preventing the separation  
320     of an individual quark or gluon. This explains the meaning of the term "confinement"  
321     adopted to describe this energy regime. From the theoretical point of view, the large value  
322     of  $\alpha_s$  make impossible any perturbative approach in the solution of the Hamilton equation  
323     of the system. A successful solution is to perform the study of the system on a discrete  
324     space. Such techniques are known as lattice QCD and are based on numerical Monte Carlo  
325     simulations. The challenge for the calculations is to reduce the lattice spacing in order to  
326     approach the continuum.

328     **Asymptotic freedom** Reducing the distance between quarks and gluons (i.e. increas-  
329     ing  $Q$  in Figure 1) the coupling constant  $\alpha_s$  becomes smaller. As anticipated, this is a  
330     unique feature among the forces and comes from the non-abelian nature of the QCD gauge  
331     symmetry. Such a phenomenon is also depicted by the weakening of the anti-screening  
332     effect of the surround- ing virtual gluons with decreasing distance. In this way two quarks

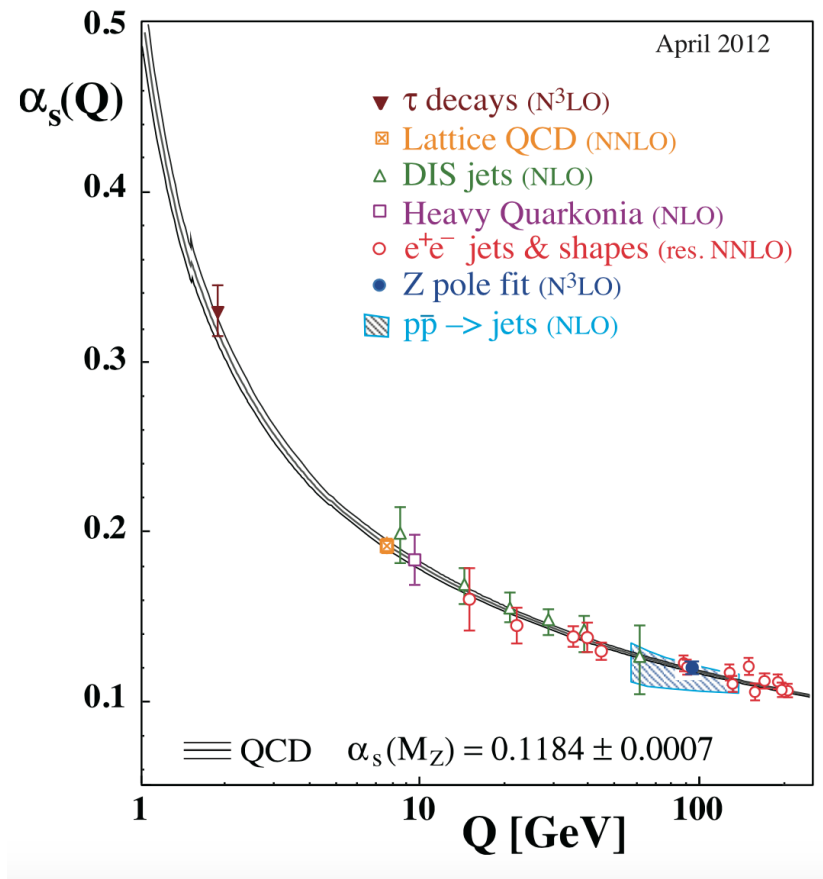


Figure 1: QCD coupling constant as a function of momentum transfer. Experimental data and also theoretical prediction are presented. [1]

334 closer and closer in space show each other a smaller and smaller color charge.

335

336 **Chiral symmetry** One further property of interest is connected to the chirality of  
337 the quark. It can be verified that the QCD lagrangian for massless quarks is invariant  
338 under a chiral rotation ( $SU_L(N_f) \times SU_R(N_f)$ ), while the operator  $\bar{q}q = \bar{q}_L q_R + \bar{q}_R q_L$  is  
339 not invariant (in the axial part), meaning that the mesons (state  $\bar{q}q$ ) should have the same  
340 mass. Experimentally this is clearly not true, and it could be shown that the axial current  
341 is conserved (PCAC and the Goldberger-Treiman relation). The solution to this puzzle  
342 is that the chiral (axial-vector) symmetry is spontaneously broken; this means that the  
343 symmetry of the Hamiltonian is not a symmetry of the corresponding ground state. It  
344 has also been shown, by G. t'Hooft, that the confinement implies a dynamical breaking  
345 of the chiral symmetry. This means that the breaking comes from the interaction between  
346 the objects in the system. From this follows that the masses of the quarks are strongly  
347 increased because of the interaction with the constituents of the system. This mechanism,  
348 known as dynamical chiral symmetry breaking justifies the mass of the hadrons, reducing  
349 the role of the Higgs mechanism in the mass explanation at least for the light hadrons.

350 The asymptotic freedom property suggests the existence of a state of matter, called  
351 Quark-Gluon Plasma (QGP), in which the constituents of the hadrons are de-confined.  
352 The hatched region in Figure 2 presents the expected phase boundary between partonic  
353 and hadronic matter from lattice QCD calculations.

354 Two relevant thermodynamical observables of the system are plotted in the figure. One  
355 is temperature  $T$  and another one is the baryonic chemical potential  $\mu_B$ . The red points  
356 have been measured from thermal models fit on data from different experiment [14] and  
357 lie along a line that represent the limit between the two phases. As one can see in Figure  
358 2, there are different ways to achieve the transition. It can be performed by changing the  
359 temperature and/or the net baryonic density ( $\mu_B$ ).

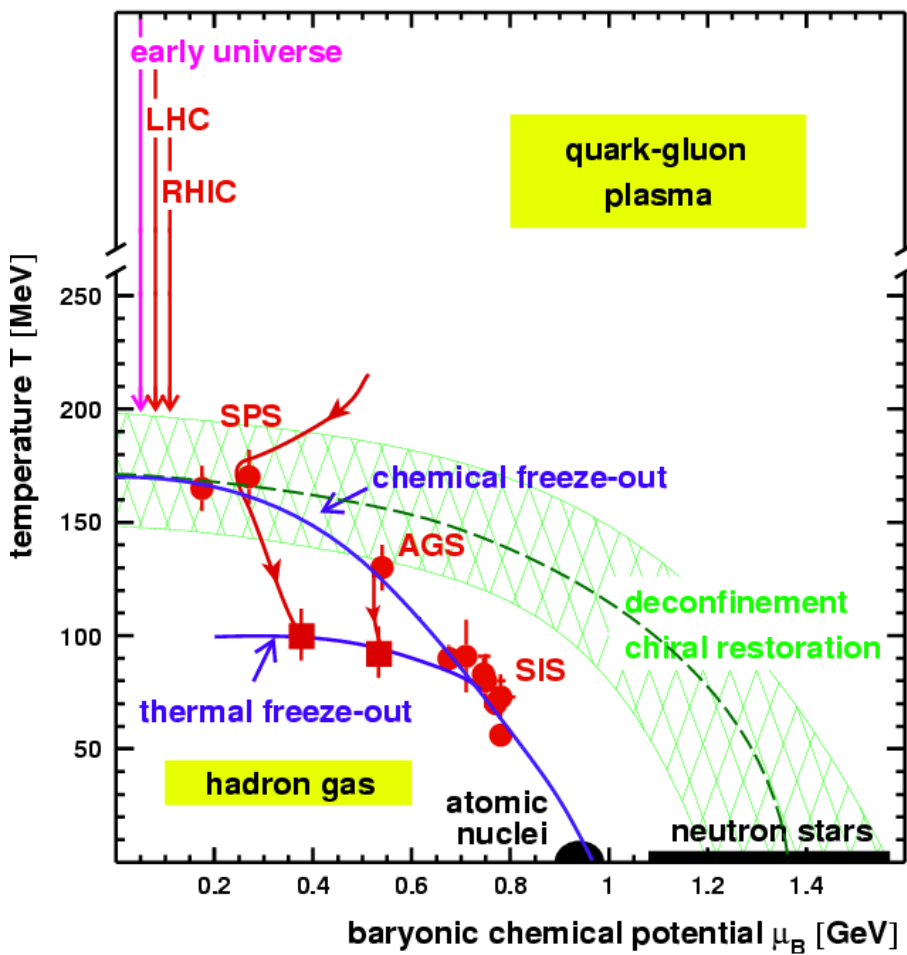


Figure 2: Phase diagram of partonic and hadronic matter. The chemical freeze out points are determined from thermal models fit to heavy ion data at SIS, AGS, and SPS energies. (<http://na49info.web.cern.ch/na49info/Public/Press/findings.html>)

360 **1.3 Heavy Ion Collisions**

361 Knowledge of the space-time evolution of the system created in high energy heavy ion  
 362 collisions help to understand the dynamics of nuclear matter under extreme conditions.  
 363 The Figure 3 presents the schematic of the time evolution in case of collision of two Lorentz  
 364 contracted nuclei at very high energy. After the colliding, a large amount of energy can be  
 365 deposited in a small area of space and in a short duration of time. The matter produced  
 366 might have very high energy density and temperature so that it is sufficiently able to reach  
 367 to QGP that is baryon free region.

368 Just after the colliding, the medium may not be in thermal equilibrium which can be  
 369 reached after that the evolution is governed by the law of thermodynamics. As the system  
 370 expands and cools, the hadronization takes place and the freeze out comes after some  
 371 time. Different stages during the collisions can be studied by various observables, such as,  
 372 Electromagnetic probes, Quarkonia and heavy flavour, Hard probes, Electroweak probes,  
 373 global properties and Freeze-out condition as well. Most of the produced particles in the  
 374 high energy heavy-ion collisions are emitted at freeze-out. In order to estimate the energy  
 375 density, pressure, temperature and baryon chemical potential, the study of particle after  
 376 freeze-out gives crucial information. Those quantities could be derived from measurement  
 377 of multiplicity and rapidity distribution, transverse momentum ( $p_T$ ) distributions.

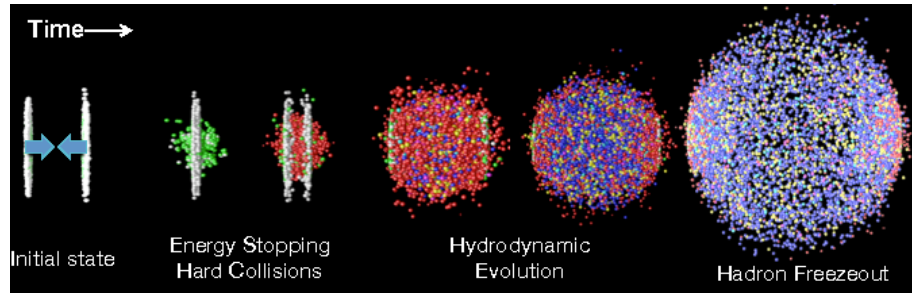


Figure 3: The time evolution of a high energy heavy ion collision. [2]

378 In the case a QGP is formed, it will eventually expand because of its internal pressure.  
 379 As the system expands it also cools. The space-time evolution of the expansion can be  
 380 seen in Figure 4 (right side). A and B represent the two incoming ion beams. After a pre-  
 381 equilibrium phase a QGP is formed. As it expands, the system will eventually reach what  
 382 is known as the critical temperature ( $T_c$ ). At this point partons begin to hadronize and this  
 383 will continue until the chemical freeze-out ( $T_{ch}$ ) takes place, when inelastic collisions cease.  
 384 At this stage the distribution of hadrons is frozen. As cooling and expansion continue the  
 385 hadrons reach what is called thermal freeze out ( $T_{fo}$ ). Here the elastic collisions stop and  
 386 the hadrons carry fixed momenta. The QGP state can not be directly observed, because of  
 387 its short lifetime. Instead, through experiment we measure the final state hadrons, which

388 have a fixed momentum after  $T_{fo}$ . The observables of interest should tell us about the  
389 de-confinement and the thermodynamic properties of the matter. Moreover, experimental  
390 measurements include yields and  $p_T$ spectra of various particle species, azimuthal studies  
391 of high  $p_T$ particles, phase space distributions, and particle correlations.

392 A practical way to reach a critical condition in which a nuclear system should undergo  
393 a phase transition to the QGP, at high temperature and/or matter density, is to collide  
394 two nuclei at sufficiently high energy. Therefore, relativistic and ultra-relativistic heavy-ion  
395 collisions are a unique tool to study nuclear matter under extreme conditions.

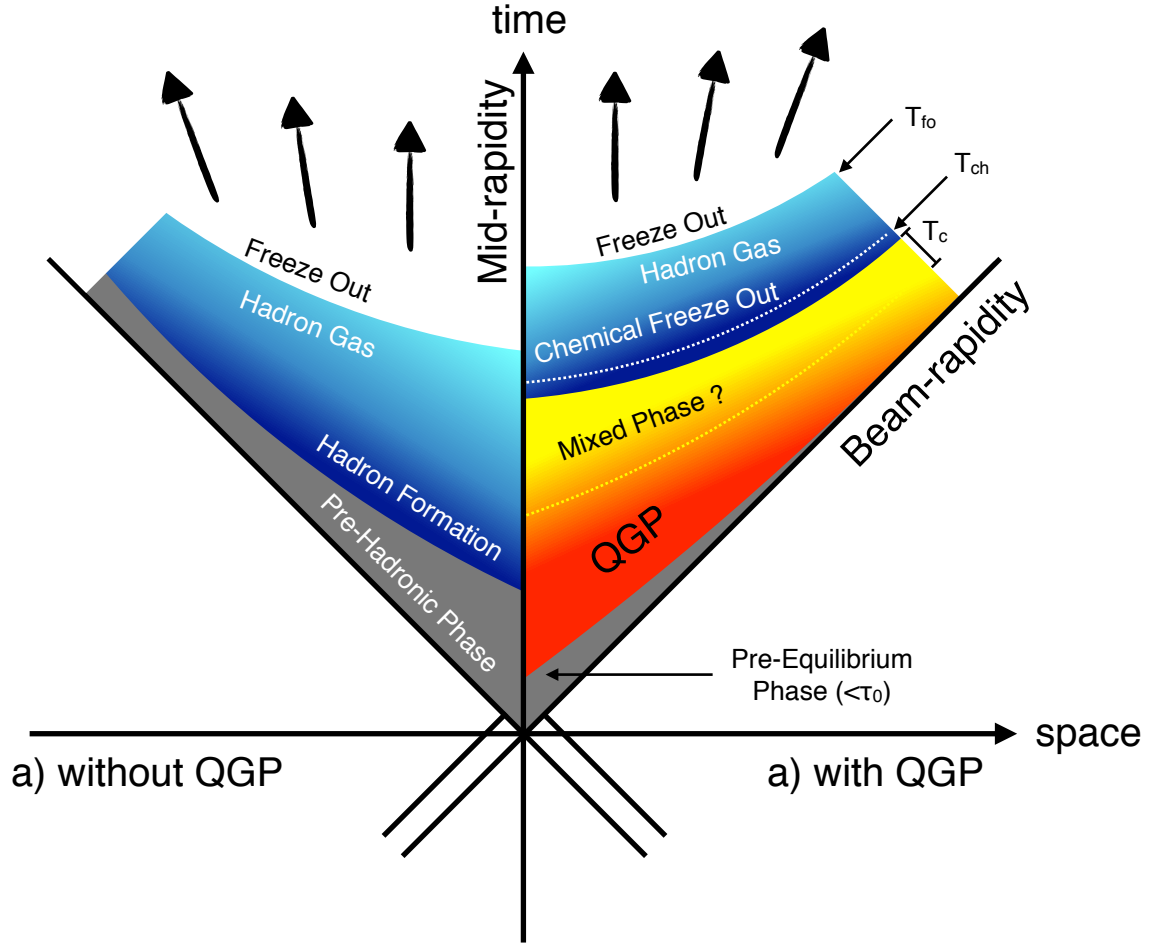


Figure 4: Hydrodynamic evolution of a heavy ion collision with and without the formation of a QGP.

## 396 2 Theoretical models

### 397 2.1 Statistical-Thermal model

398 The statistical-thermal model deal with the fireball created from high energy collisions as  
 399 an ideal gas of hadrons including resonances. These hadrons are described by local thermal  
 400 distributions at freeze-out with the parameters common to all particle species. The  
 401 model has proved successful in applications to relativistic collisions of both heavy ions and  
 402 elementary particles. The comparison between prediction and data obtained from Pb–Pb  
 403 collisions are shown in Figure 5. In light of this success, THERMUS, a thermal model  
 404 analysis package, has been developed for incorporation into the object-oriented ROOT  
 405 framework [15].

406

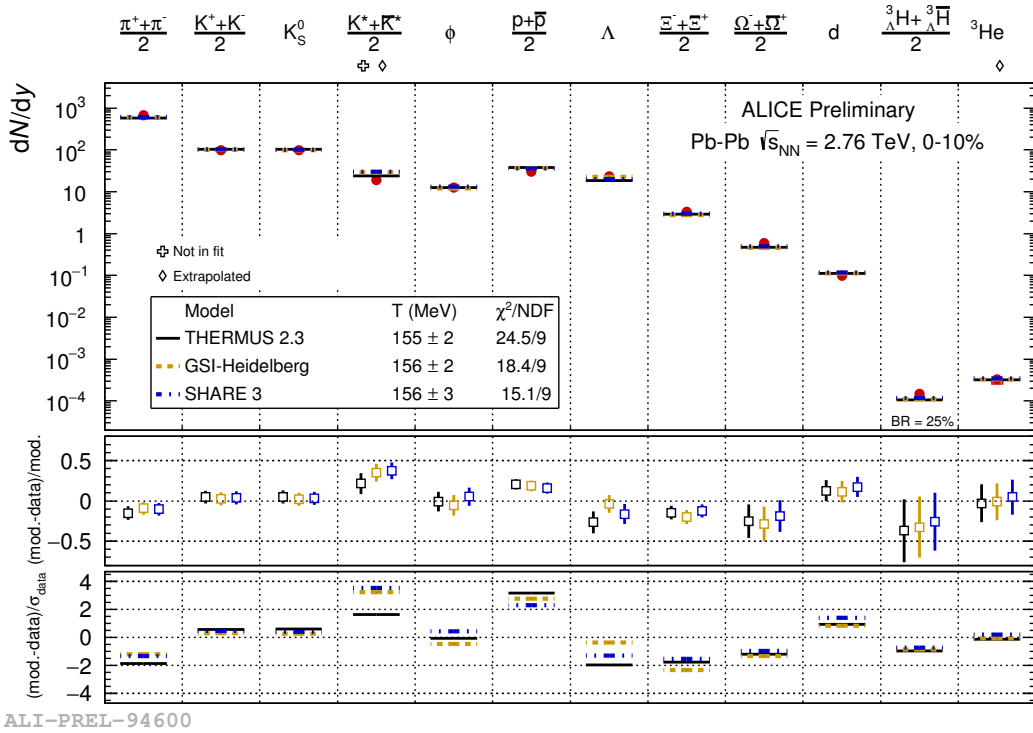


Figure 5: Grand canonical thermal fit of 0-10% central Pb-Pb collisions, with 3 models (THERMUS, GSI, SHARE).

407 There are three types of statistical-thermal models in explaining data in high energy  
 408 nuclear physics and THERMUS treats the system quantum numbers B (baryon number),

409 S (strangeness) and Q (charge) within three distinct formalisms:

- 410 1. **Grand-Canonical Ensemble:** Because the hot dense matter produced in nucleus-  
411 nucleus collisions is large enough, this ensemble is the most widely used in applica-  
412 tions to heavy-ion collisions, in which the quantum numbers or particle numbers are  
413 conserved on average through the temperature and chemical potential.
- 414 2. **Fully-Canonical Ensemble:** In which B, S and Q are exactly conserved and this  
415 ensemble used in high-energy elementary collisions such as pp, p $\bar{p}$  and e $^-$ e $^+$  collisions.
- 416 3. **Strangeness-Canonical Ensemble:** In heavy-ion collisions, the large numbers of  
417 baryons and charged particles generally allows baryon number and charge to be  
418 treated grand-canonically. However, in small systems or at low temperatures, a  
419 canonical treatment leads to a suppression of hadrons carrying non-zero quantum  
420 numbers, since these particles have to be created in pairs and the resulting low pro-  
421 duction of strange particles needs a canonical treatment of strangeness. Within this  
422 ensemble the strangeness in the system is fixed exactly by its initial value of S, while  
423 the baryon and charge content are treated grand-canonically.

424 In order to calculate the thermal properties of a system, the partition function requires to  
425 be evaluated. The form of it clearly depends on the choice of ensemble. In the present  
426 analysis the strangeness-canonical ensemble used and statistical-thermal model requires six  
427 parameters as input: the chemical freeze-out temperature  $T$ , baryon and charge chemical  
428 potentials  $\mu_B$  and  $\mu_Q$  respectively, canonical or correlation radius,  $R_C$ ; the radius inside  
429 which strangeness is exactly conserved and the fireball radius  $R$ . An additional strangeness  
430 saturation factor  $\gamma_S$  has been used as indicator of a possible departure from equilibrium  
431 and  $\gamma_S = 1.0$  corresponds to complete strangeness equilibration.

432 The volume dependence cancels out when studying the particle ratios as well as strangeness  
433 canonical equivalent to grand canonical formalism if  $\Delta S = 0$  in the ratios and  $\gamma_S$  also can-  
434 cels out. Parameters used in the analysis reported in Table 3.

Table 3: Parameters used in the thermal-model calculations.

Parameter	Value
$T$ (MeV)	varied
$\mu_B$ (MeV)	0.1
$\mu_Q$ (MeV)	0.0
$\gamma_S$	1.0

435

436 **2.1.1 Calculations**

437 *Concept:*

438 In order to calculate the particle ratios within strangeness canonical formalism of THER-  
439 MUS, temperature varied between 60 MeV to 180 MeV and particle yields extracted for  
440 each temperature value and then primary particle ratios calculated for each case.

441

442 *Feed-Down Correction:*

443 Since the particle yields measured by the detectors in collision experiments include feed-  
444 down from heavier hadrons and hadronic resonances, the primitive hadrons are allowed to  
445 decay to particles considered stable by the experiment before model predictions are com-  
446 compared with experimental data. In the analysis only  $\Lambda$  particles counted as stable (do not  
447 allowed to decay) so there is no feed-down contribution from these particles to the other  
448 ratios.

449

450 Properties of studied particles and their particle ratios listed in Table 4 and Table 5,  
451 respectively.

452

453

Table 4: Properties of particles used in the ratio calculations.

Particle	$\Delta^{++}$	$\Delta^{++}$	$p$	$K^{*0}$	$K^+$	$\Lambda^*$	$\Lambda$	$\Sigma^{*+}$	$\Sigma^+$	$\Sigma^0$	$\Xi^{*0}$	$\Xi^-$
Mass (MeV/ $c^2$ )	1232	938.27	895.92	493.67	1519.5	1115.68	1382.8	1189.37	1192.64	1531.80	1321.31	-
Width (MeV/ $c^2$ )	120	-	50.7	-	15.6	-	37.6	-	-	9.1	-	-
$c\tau$ (fm)	1.6	-	3.9	-12.6	-	5.51	-	-	21.6	-	-	-
Ang. Momentum ( $J$ )	$3/2$	$1/2$	1	0	$3/2$	$1/2$	$3/2$	$1/2$	$1/2$	$3/2$	$1/2$	$1/2$
$^{22}_N$ Isospin ( $I$ )	$3/2$	$1/2$	$1/2$	$1/2$	0	0	1	1	1	$1/2$	$1/2$	$1/2$
Parity ( $P$ )	+1	+1	-1	0	-1	+1	+1	+1	+1	+1	+1	+1
Strangeness ( $S$ )	0	0	1	1	-1	-1	-1	-1	-1	-2	-2	-2
Baryon Number ( $B$ )	1	1	0	0	1	1	1	1	1	1	1	1
Decay Channel	$p\pi^+$	-	$\pi^-$	$\mu^+\nu_\mu$	$pK^-$	$p\pi^-$	$\Lambda\pi^+$	$p\pi^0$	$\Lambda\gamma$	$\Xi^-\pi^+$	$\Lambda\pi^-$	-
Branching Ratio (%)	$\sim 100$	-	$\sim 66.7$	$\sim 63.54$	$\sim 45$	$\sim 63.9$	$\sim 87$	$\sim 51.6$	$\sim 100$	$\sim 64$	$\sim 99.9$	-
Q-Value(MeV/ $c^2$ )	154.16	-	262.68	-	87.55	37.84	127.55	111.53	76.96	70.92	70.66	-

Table 5: Difference of mass ( $\Delta M$ ), baryon number ( $\Delta B$ ), strangeness ( $\Delta S$ ) and charge ( $\Delta Q$ ) of the ratios.

Particle	$\Delta^{++}/p$	$K^*/K^+$	$\Lambda^*/\Lambda$	$\Sigma^{*+}/\Lambda$	$\Sigma^0/\Lambda$	$\Sigma^{*+}/\Sigma^+$	$\Xi^{*0}/\Xi^-$
$\Delta M$ (MeV/ $c^2$ )	293.8	402.25	403.82	267.12	76.96	193.43	210.49
$\Delta B$	0	0	0	0	0	0	0
$\Delta S$	0	0	0	0	0	0	0
$\Delta Q$	+1	-1	0	+1	0	0	-1
Slope (%) per MeV	0.19	0.76	0.98	0.25	-0.08	0.37	0.42

454    **2.1.2 Results and comparison with data**

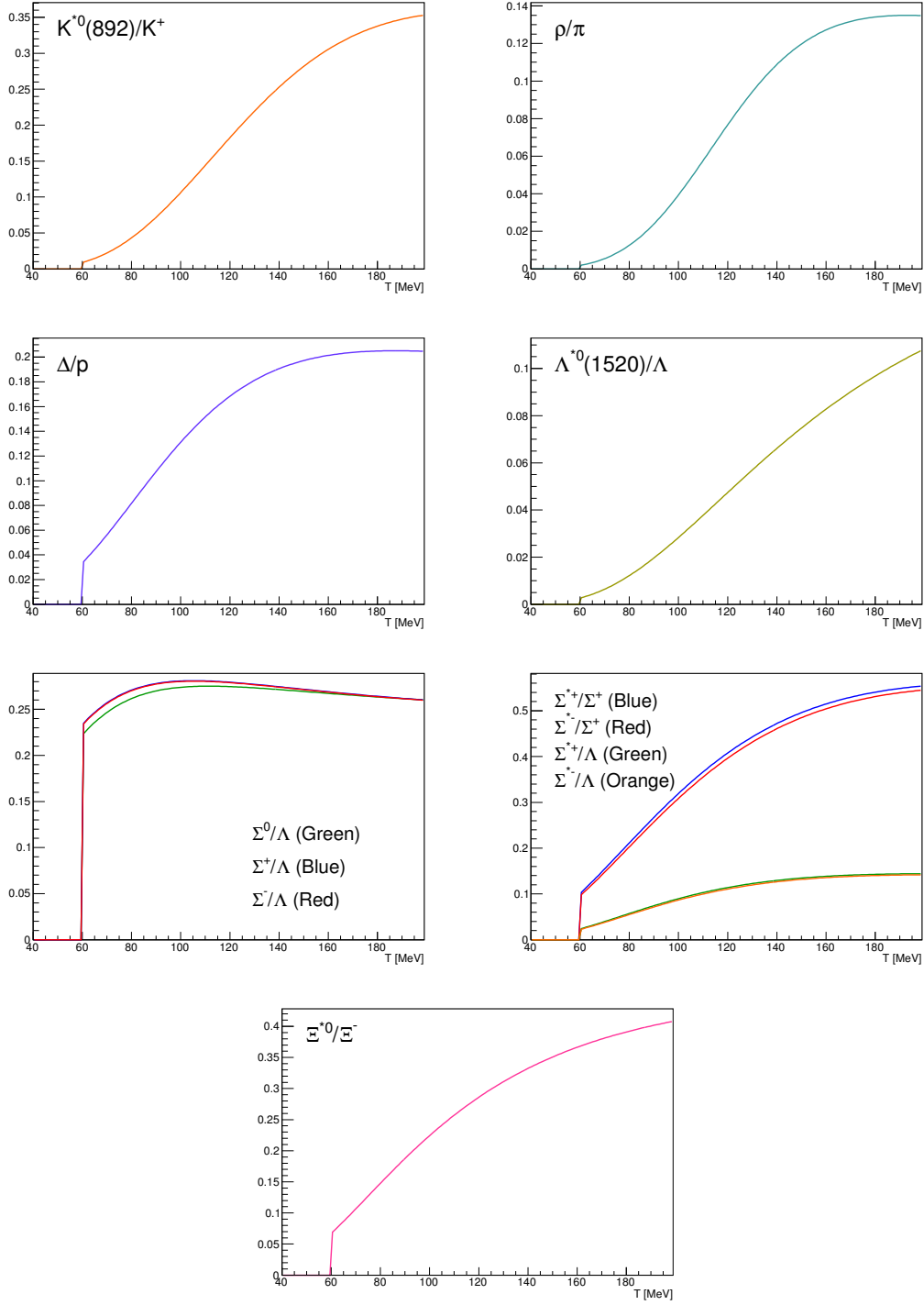


Figure 6: Ratio of baryonic and mesonic resonances over their stable partner as a function of temperature.

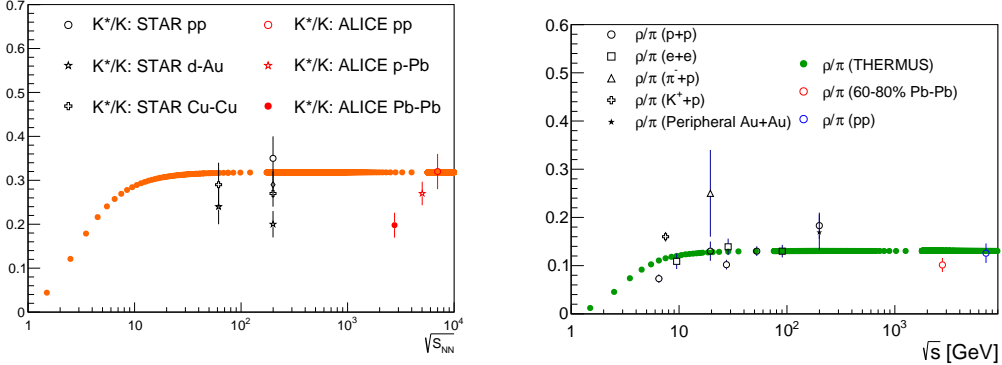


Figure 7: Ratio of resonances over their stable partner as a function of  $\sqrt{(s)}$ .

## 455 2.2 EPOS, UrQMD

456 The EPOS3 model [16, 17, 18] describes the full evolution of a heavy-ion collision. The  
 457 initial stage is treated via a multiple-scattering approach based on Pomerons and strings.  
 458 The reaction volume is divided into a core and a corona part [19]. The core is taken as  
 459 the initial condition for the QGP evolution, for which one employ viscous hydrodynamics.  
 460 The corona part is simply composed of hadrons from string decays. After hadronisation of  
 461 the fluid (core part), these hadrons and as well the corona hadrons are fed into UrQMD  
 462 [20, 21], which describes hadronic interactions in a microscopic approach. The chemical  
 463 and kinetic freeze-outs occur within this phase. The chemical freeze-out is expected to  
 464 occur shortly after the phase transition from partonic to hadronic matter and is followed  
 465 by the kinetic freeze-out.

466 As explained in [16, 17, 18, 19], EPOS3 is an event generator based on 3+1D vis-  
 467 cous hydrodynamical evolution starting from flux tube as an initial conditions, which are  
 468 produced in the Gribov-Regge multiple scattering framework. An individual scattering is  
 469 treated as a Pomeron, identified with a parton ladder, eventually showing up as flux tubes  
 470 (or strings). Each parton ladder is composed of a pQCD hard process, plus initial and final  
 471 state linear parton emission.

472 The final state partonic system (corresponding to a Pomeron) amounts to (usually two)  
 473 color flux tubes, being mainly longitudinal, with transversely moving pieces carrying the  
 474  $p_T$  of the partons from hard scatterings. One has two flux tubes based on the cylindrical  
 475 topology of the Pomerons. Each quark- antiquark pair in the parton ladder will cut a string  
 476 into two; in this sense one may have more than two flux tubes. In any case, these flux  
 477 tubes eventually constitute both bulk matter, also referred to as "core" (which thermalizes,  
 478 flows, and finally hadronizes) and jets (also referred to as "corona"), according to some

479 criteria based on the energy of the string segments and the local string density. For the  
480 core, we use a 3+1D viscous hydrodynamic approach, employing a realistic equation of  
481 state, compatible with lQCD results. We employ for all calculations in this paper a value  
482 of  $\eta/s = 0.08$ . Whenever a hadronization temperature of  $T_H$  is reached, we apply the  
483 usual Cooper-Frye freeze-out procedure, to convert the fluid into particles. We use  $T_H =$   
484 166MeV. From this point on, we apply the hadronic cascade UrQMD [20, 21], about which  
485 more details are given later. All hadrons participate in the cascade, including those from  
486 the core (after freeze- out) and the corona. The corona particles, from string decay, are only  
487 "visible" after a certain formation time (some constant of order one fm/c), multiplied by  
488 the corresponding gamma factor), so very high  $p_T$  particles have a good chance to escape.

489 The UrQMD model is a non-equilibrium transport approach. The interactions of  
490 hadrons in the current version include binary elastic and  $2 \rightarrow n$  inelastic scatterings, res-  
491 onance creations and decays, string excitations, particle + antiparticle annihilations as  
492 well as strangeness exchange reactions. The cross sections and branching ratios for the  
493 corresponding interactions are taken from experimental measurements (where available),  
494 detailed balance relations and the additive quark model. The model describes the full  
495 phase-space evolution of all hadrons, including resonances, in a heavy- ion collision based  
496 on their hadronic interactions and their decay products. Due to the short lifetime of res-  
497 onances, their decay products may interact in the hadronic phase. This is not the case  
498 for weak decays, where the system has already decoupled at the time of the decay. As  
499 discussed previously, the experimental reconstruction of resonances will be influenced by  
500 the final state interactions of the decay products. Resonance signals have been previously  
501 studied using the UrQMD model.

502 **3 Production of resonance with strangeness**

503 The Quark Model, proposed independently by Murray Gell-Mann and Yuval Ne?eman in  
 504 1964 [22], enables the classification of hadrons in terms of their constituent quarks. In  
 505 this model, the lighter mesons and baryons are representations of an  $SU_f(3)$  group, whose  
 506 fundamental representation is the three dimensional vector (u, d, s). These are the three  
 507 lighter quarks whose characteristics are reported in Table reftable:quark.

Light flavor	d	u	s
Baryon number (B)	+1/3	+1/3	+1/3
Electric charge (Q)	-1/3	+2/3	-1/3
Isospin (I)	-1/2	+1/2	0
Strangeness (S)	0	0	-1
mass ( $\text{MeV}/c^2$ )	$2.3^{+0.7}_{-0.5}$	$4.8^{+0.5}_{-0.3}$	$95 \pm 5$

Table 6: Quantum numbers and masses associated to the three lighter quarks: u, d and s

508 The hadronic state are obtained from the decomposition of the following scalar prod-  
 509 ucts of the fundamental representations of the group:

510      Meson ( $q\bar{q}$ )  $3 \otimes \bar{3} = 1 \oplus 8$

512      Baryon ( $qqq$ )  $3 \otimes 3 \otimes 3 = 10_S \oplus 8_M \oplus 8_M \oplus 1_A$

515 For the baryons without *c* or *b* quark, flavor and spin may be combined in an approxi-  
 516 mate flavor-spin  $SU(6)$ , in which the six basic states are  $d \uparrow, d \downarrow, \dots, s \downarrow$  ( $\uparrow, \downarrow$  = spin up,  
 517 down). Then the baryons belong to the multiplets on the right side of

519       $6 \otimes 6 \otimes 6 = 56_S \oplus 70_M \oplus 70_M \oplus 20_A$

521 Here, the 56 representation can be decompose in an octet ( $J^P = 1/2^+$ ) and a decuplet  
 522 ( $J^P = 3/2^+$ ), as can be seen in Figure 8 and Figure 9.

523 Among the hadrons, the special family of particles that contain at least one strange  
 524 quark but not heavier quarks (like charm or bottom), are called hyperons. These are:  
 525 the  $\Lambda$ (uds), the triplet  $\Sigma^+(uus)$ ,  $\Sigma^0(uds)$ ,  $\Sigma^-(dds)$ , the doublet  $\Xi^-(dss)$ ,  $\Xi^0(uss)$  and the  
 526  $\Omega(sss)$  and the corresponding antiparticles.  $\Xi$  and  $\Omega$  are the only hyperons containing more  
 527 than one strange quark, hence they are called multi-strange baryons. Resonances shown in  
 528 Figure reffig:decuplet having \* with its name (e.g.  $X^{*\pm}$ ) are particles with higher mass than  
 529 the corresponding ground state particle with the same quark content. Different resonances  
 530 with different lifetimes can probe different stages of the fireball expansion. The lifetime  
 531 of some short-lived resonances is reported in Table 7. The ratios between resonances and

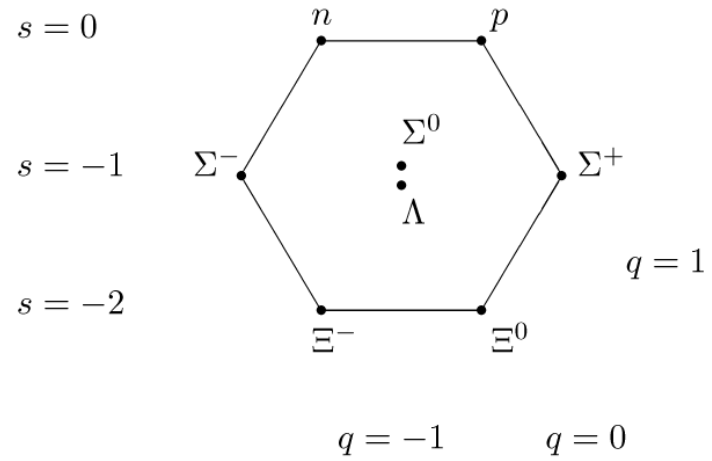


Figure 8: The  $J^P = 1/2^+$  ground state baryon octet

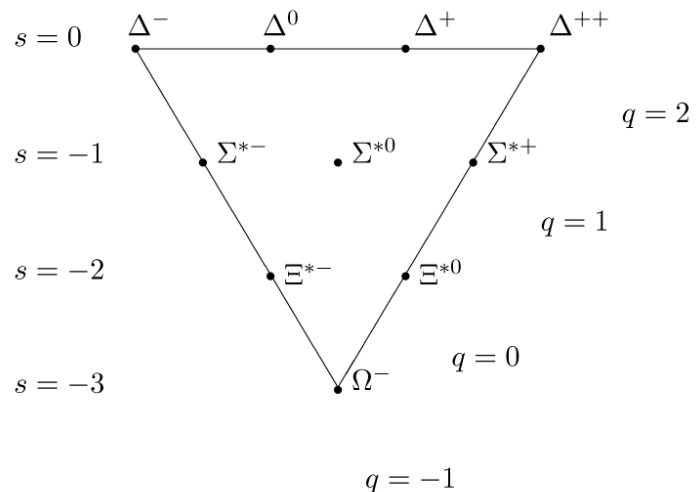


Figure 9: The  $J^P = 3/2^+$  baryon decuplet

stable hadrons can be compared for resonances with different lifetimes and provide insights on the role of the re-scattering effect between the two freeze-out phases.

Particle	$\rho(770)$	$\Delta(1232)$	$K^*(892)$	$\Sigma(1385)$	$\Lambda(1520)$	$\Xi(1530)$	$\Phi(1020)$
Lifetime[c $\tau$ ]	1.3 fm	1.7 fm	4.0 fm	5.5 fm	10.3 fm	22 fm	46 fm

Table 7: Lifetime of hadronic resonances

In the following, a general overview of the role of the strange quark within the QGP studies with heavy-ion collisions is given. And importance of the measurement of resonance is explained as probe of properties in hadronic phase between the chemical( $T_{ch}$ ) and the kinetic freeze-out( $T_{kin}$ ).

### 3.1 Strange quark and hyperons

The original interest in the strangeness in the context of the QGP comes from an idea by Johann Rafelski and Berndt Müller. In 1982, they suggested a possible signature for the formation of a QGP in a heavy-ion collision [23]. The key argument, at a fixed collision energy, rests on the different production mechanism of the s quark within two different systems:

- 1. **Hadron Gas (HG)** , where the degrees of freedom are the hadronic ones, as quark and gluons are confined
- 2. **QGP** , where the degrees of freedom are partonic ones, with quarks and gluons free with respect to each other

The mass of the hadrons is only partly due to the mass of the constituent valence quarks.

Naively speaking, the quarks ?dress up? due to the strong interaction that keeps them confined. Once they are free, as in a QGP, the quarks recover their bare masses. It was predicted that, if the QGP is formed, an enhancement of the strange quarks should occur, because the production of  $s\bar{s}$  pairs becomes easier due to the lower energy needed. When the QGP cools down, these strange quarks eventually recombine into hadrons favoring also an enhancement of the number of strange hadrons. This effect is larger for hadrons with higher strangeness, with the following scaling for the number type:

$N_\Omega > N_\Xi > N_\Lambda$   
where  $N_\Omega$ ,  $N_\Xi$ ,  $N_\Lambda$  are the number of produced  $\Omega$ ,  $\Xi$  and  $\Lambda$ . A certain enhancement of strange hadrons can occur also in a hadron gas system, but the processes of hadronisation in this case are relatively easy for K and  $\Lambda$ . and progressively harder for hadrons with higher strangeness, hence the relation would be:

564       $N_\Omega < N_\Xi < N_\Lambda$ .

565      The production of multi-strange hadrons with respect to pp - like collisions is considered  
 566      to be a signature of the formation of the QGP and it was observed at SPS, RHIC and LHC.  
 567      [24]

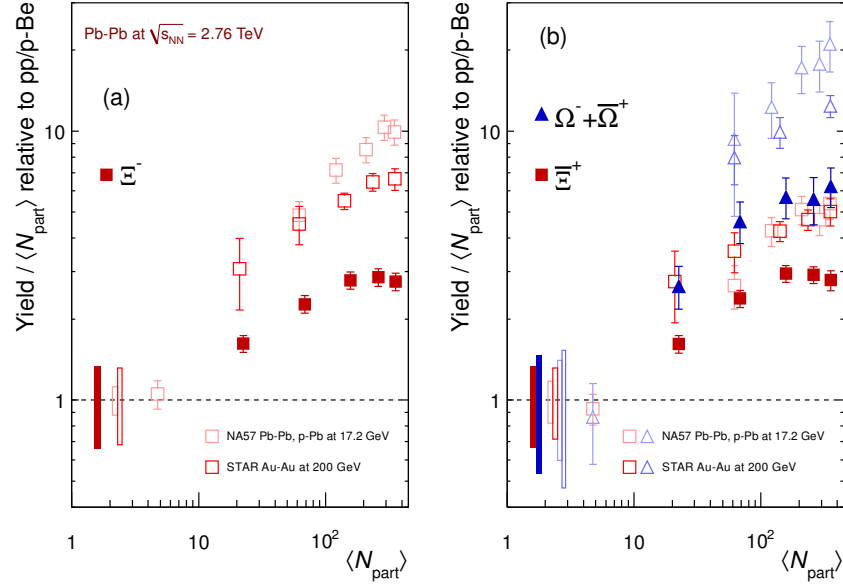


Figure 10: Enhancements in the rapidity range  $|y| < 0.5$  as a function of the mean number of participants  $\langle N_{part} \rangle$ , showing LHC (ALICE, full symbols), RHIC and SPS (open symbols) data. Boxes on the dashed line at unity indicate statistical and systematic uncertainties on the pp or p-Be reference. Error bars on the data points represent the corresponding uncertainties for all the heavy-ion measurements and those for p-Pb at the SPS.

568      The measured enhancement factors of baryons with increasing strangeness content are  
 569      reported in Figure 10 as a function of the number of participant nucleons,  $\langle N_{part} \rangle$ , in  
 570      comparison with similar measurements at SPS and RHIC. For p-Pb collisions there is no  
 571      evidence of enhancement. For Pb-Pb collisions the enhancement increases with centrality  
 572      and the effect is larger for particles with higher strangeness content, up to a factor ?20 for  
 573      ?s. No hadronic model has reproduced these observations and they can be interpreted as  
 574      clear signal of QGP state formation. The comparison with results from the previous ex-  
 575      periments shows that the relative enhancements decrease with increasing collision energy.  
 576      An explanation of this behavior is given in terms of a statistical model, with canonical  
 577      strangeness conservation. In a small system, with small particles multiplicities, quantum  
 578      numbers conservation laws (such as strangeness) must be applied locally, event-by-event,

579 whereas in a large system, with many degrees of freedom, they can be applied in average,  
 580 by means of the corresponding chemical potential. The conservation of quantum numbers  
 581 is known to reduce the phase space available for particle production. This canonical sup-  
 582 pression factor decreases with lower energy in the centre of mass of the collisions and could  
 583 explain the larger enhancement for lower energy systems.

584 **3.2 Resonance production**

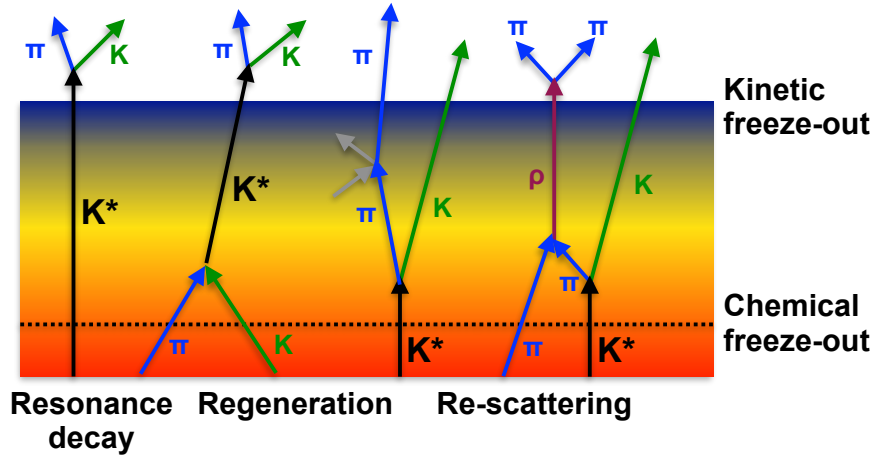


Figure 11: Hadronic phase

585 Resonances are particles with higher mass than the corresponding ground state particle  
 586 with the same quark content. Hadronic resonances decay strongly, thus with a short  
 587 lifetime,  $\tau \sim$  few tenths of fm/c. The resonance natural width is given by  $\Gamma = \bar{h}/\tau$ , that  
 588 is inversely proportional to the lifetime. Broad states with finite  $\Gamma$  decay very shortly  
 589 after being produced and can be measured only by reconstruction of their decay products  
 590 (or "daughters") in a detector. In heavy-ion collisions, hadronic resonances are produced  
 591 within the bulk of the expanding medium, where they can decay while still traversing its  
 592 volume. Decay products may interact with the other particles of the medium (mostly pions  
 593 at the LHC), resulting in the impossibility of reconstructing the resonance, because the  
 594 invariant mass of the daughters does not match that of the parent particle. Conversely,  
 595 resonances may be regenerated as a consequence of pseudo-elastic collisions in the time  
 596 lapse between the chemical ( $T_{ch}$ ) and the kinetic freeze-out ( $T_{kin}$ ). Re-scattering and  
 597 regeneration depend on the individual cross section, hence lifetime, of the resonances and  
 598 affect the measurement of their yield and momentum spectrum. The yield is decreased if the  
 599 re-scattering dominates, vice versa the regeneration feeds the system with more particles.

600 The two effects may even compensate. Different resonances with different lifetimes can  
601 probe different stages of the fireball expansion. The ratios between resonances and stable  
602 hadrons can be compared for resonances with different lifetimes and provide insights on  
603 the role of the re-scattering effect between the two freeze-out phases.

604 **4 A Large Ion Collider Experiment at the LHC**

605 ALICE (A Large Ion Collider Experiment) has been collecting data during the whole first  
606 phase of the Large Hadron Collider operations, from its startup on the 23 November 2009  
607 to the beginning of the first long technical shutdown in February 2013. During the first  
608 three years of operations LHC provided pp collisions at 0.9, 2.76, 7 and 8 TeV, Pb–Pb colli-  
609 sions at 2.76A TeV and finally p–Pb collisions at 5.02 TeV. The first section of this chapter  
610 focuses on the LHC performance during this phase and includes details on the accelerator  
611 parameters that allow the LHC to perform as a lead ion collider. A detailed description  
612 of the ALICE detector follows in the section 4.2.1. ALICE has been designed and op-  
613 timized to study the high particle-multiplicity environment of ultra-relativistic heavy-ion  
614 collisions and its tracking and particle identification performance in Pb–Pb collisions are  
615 discussed. The attention is drawn in particular on the central barrel detectors. Section  
616 4.2.2 describes the ALICE Data Acquisition (DAQ) system, that also embeds tools for the  
617 online Data Quality Monitoring (DQM). The final part of the chapter is dedicated to the  
618 offline computing and reconstruction system based on the GRID framework.

619 **4.1 The Large Hadron Collider**

620 The Large Hadron Collider (LHC) [25] at CERN is the biggest particle accelerator world-  
621 wide. The LHC project was approved in 1994 and construction works in the existing  
622 underground tunnel started in 2001 after the dismantling of the LEP collider, which had  
623 previously been built in the tunnel which is located under the Swiss-French border area  
624 close to Geneva at a depth of 50 to 175 m. The LHC has a circumference of 26.7 km. By  
625 design, its maximum achievable energies are 7 TeV for beam of protons and 2.76 TeV per  
626 nucleon for beam of lead ions, thus providing collisions at  $\sqrt{s} = 14$  TeV and  $\sqrt{s_{NN}} = 5.5$   
627 TeV, respectively. These would be the largest energies ever achieved in particle collision  
628 experiments. The LHC is a synchrotron that accelerates two counter-rotating beams in  
629 separate parallel beam pipes. In each of them bunches of particles travel many times  
630 around the accelerator ring before the collision energy is reached. The accelerator has to  
631 bend the beams around the ring, keep the bunches focused and accelerate them to their  
632 collision energy. Finally, the spatial dimension of the bunches has to be minimized in order  
633 to attain high luminosity, which ensure a high number of collisions per time interval at  
634 the collision points, i.e. a high luminosity. A combination of magnetic and electric field  
635 components performs the mentioned tasks. Despite the high luminosity reached, only a  
636 very small fraction of the particles of two bunches collides in a single bunch crossing. The  
637 others leave the interaction region essentially uninfluenced, are defocused, and continue to  
638 circulate in the accelerator.

639 Injection of bunches into the LHC (Figure 12) is preceded by acceleration in the  
640 LINAC2, PS booster, PS, and SPS accelerators. The acceleration sequence is slightly  
641 different for heavy-ions, in which case bunches pass the LINAC3, LEIR, PS, and SPS

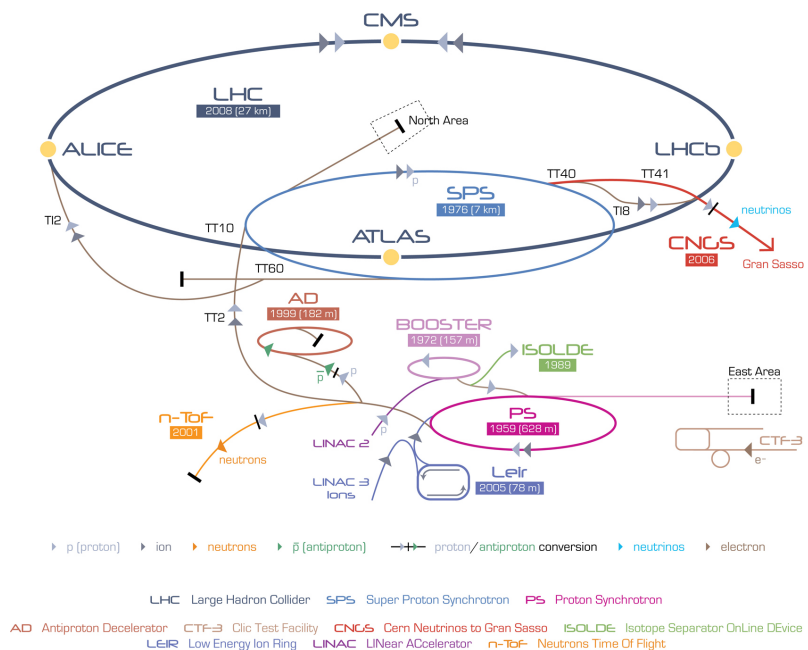


Figure 12: The CERN accelerator complex [3]

accelerators (more information can be found in [90]). Several injections to the LHC are needed until all bunches of both beams are filled. The first pp collisions at 900 GeV centre-of-mass energy were delivered by the LHC on September 10th 2008. Nine days later, the operations were interrupted due to a failure in an electrical connection between two magnets. The machine operators spent over a year repairing and consolidating the accelerator. On November 20th 2009 low energy proton beams circulated again, and a few days later, by achieving the energy of 1.18 TeV per proton beam, LHC became the most powerful accelerator in the world. The first pp collisions at centre-of-mass energy of 7 TeV were delivered in March 2010, and the first Pb?Pb collisions at centre-of-mass energy of 2.76 TeV per nucleon pair in November 2010. In 2010 the integrated luminosity delivered by the LHC was  $\sim 48 \text{ pb}^{-1}$  for pp collisions at  $\sqrt{s}= 7 \text{ TeV}$  ( $\sim 0.5 \text{ pb}^{-1}$  in ALICE) and  $\sim 10 \mu\text{b}^{-1}$  for Pb?Pb at  $\sqrt{s_{\text{NN}}}= 2.76 \text{ TeV}$  ( $\sim 10 \mu\text{b}^{-1}$  in ALICE). In 2011 the beam energy was the same as in 2010 both for pp and Pb-Pb. The performance of the LHC improved in terms of luminosity with  $\sim 5.61 \text{ fb}^{-1}$  for pp ( $\sim 2 \text{ pb}^{-1}$  in ALICE) and  $\sim 166 \mu\text{b}^{-1}$  for Pb-Pb collisions ( $\sim 143.62 \mu\text{b}^{-1}$  in ALICE). In 2012, the centre-of-mass energy for pp collisions was brought to 8 TeV and the integrated luminosity (up to December 2012, end of the pp program) was  $\sim 23.3 \text{ fb}^{-1}$  ( $\sim 10 \text{ pb}^{-1}$  in ALICE). A pilot p-Pb run operated at  $\sqrt{s_{\text{NN}}}= 5.02 \text{ TeV}$  on September 2012, followed by a long p-Pb run on February 2013 with a delivered luminosity of  $31.2 \text{ nb}^{-1}$ . A very short pp run at  $\sqrt{s}= 2.76 \text{ TeV}$  ended the Run1 of the LHC program, marking the start of the first long shutdown (LS1) until the end of 2014. Despite its excellent performance, the LHC has not yet achieved the nominal parameters ( $\sqrt{s}, L$ ), that is the main goal for the next ignition of the machine in 2015. The LHC produces collisions in four so called Interaction Points (IPs) in correspondence of which are located six detectors of different dimensions and with different goals, all able to study the products of the interactions. These are:

**ALICE (A Large Ion Collider Experiment-IP<sub>2</sub>)** [26] is a dedicated heavy-ion experiment designed to study strongly-interacting matter at very high energy density. It explores the phase transition to the QGP, its phase diagram, and its properties. Furthermore, ALICE will also study collisions of protons, on one hand as a baseline for heavy-ion measurements and on the other hand it contributes to measurements of identified particles by making use of its excellent particle identification capability and its acceptance at very low transverse momenta.

**ATLAS (A Toroidal LHC ApparatuS-IP<sub>1</sub>) and CMS (Compact Muon Solenoid - IP<sub>5</sub>)** [27][28] are general-purpose detectors for pp collisions that are built to cover the widest possible range of physics at the LHC. Specific topics are the search for the Higgs boson and physics beyond the Standard Model, e.g. new heavy particles postulated by supersymmetric extensions (SUSY) of the Standard Model and evidence of extra dimensions.

**LHCb (The Large Hadron Collider beauty experiment-IP<sub>8</sub>)** [29] is a dedicated

683 experiment for the study of heavy flavor physics at the LHC. In particular, the experiment  
684 focuses on the study of CP violation and rare decays of beauty and charm particles, to  
685 test the Standard Model and to search for evidence of New Physics. The LHCb physics  
686 program is complementary to the flavor physics studies conducted at the B-factories and  
687 to the direct searches for new particles performed at ATLAS and CMS.

688

689 **LHCf (Large Hadron Collider forward experiment-IP<sub>1</sub>)** [30] measures forward  
690 particles created during LHC collisions to provide further understanding of high energy  
691 cosmic rays. The detector is placed close to the ATLAS experiment.

692

693 **TOTEM (TOTal Elastic and diffractive cross-section Measurement-IP<sub>5</sub>)** [31]  
694 measures the total cross-section, elastic scattering, and diffractive processes. The detector  
695 is located close to the CMS experiment.

696

## 697 4.2 The ALICE project

698 The ALICE experiment at the LHC [32] has as main goal the study of nuclear matter  
699 under extreme conditions of temperature and energy density such as those reached in ultra-  
700 relativistic heavy-ion collisions. The aim is to verify the QCD prediction of the existence of  
701 a phase transition from the common hadronic matter to the Quark-Gluon Plasma. Since  
702 ALICE is the only LHC experiment specifically designed for Pb–Pb collisions, it has to  
703 be able to cope with the large multiplicities associated with these collision systems and at  
704 the same time has to cover as many QGP-related observables as possible. ALICE is also  
705 interested in the study of pp interactions, as these are crucial for a comparison with Pb–Pb  
706 collisions, to tune Monte Carlo models and per se, like the other LHC experiments. With  
707 respect to these experiments, ALICE is endowed with an excellent Particle IDentification  
708 (PID) performance, obtained combining different PID techniques from different detectors  
709 that are optimized in different momentum ( $p$ ) regions.

### 710 4.2.1 ALICE detector

711 ALICE is a complex of 14 detector subsystems (Figure 13) that can be classified in three  
712 groups:

713

714 **Central detectors** are housed in a solenoid magnet which provides the experiment  
715 with a 0.5 T magnetic field and covers the pseudo-rapidity interval  $-0.9 < \eta < 0.9$  (corre-  
716 sponding to a polar acceptance  $\pi/4 < \theta < 3\pi/4$ ). The azimuthal acceptance is  $2\pi$ . They  
717 are mainly dedicated to vertex reconstruction, tracking, particle identification and momen-  
718 tum measurement. Starting from the interaction region and going outward, we find the  
719 following detectors:

- Inner Tracking System (ITS)
- Time Projection Chamber (TPC)
- Transition Radiation Detector (TRD)
- Time Of Flight (TOF)

724 In the mid-rapidity region there are also three detectors with limited azimuthal accep-  
 725 tance:

- High Momentum Particle Identification Detector (HMPID)
- PHOton Spectrometer (POHS)
- ElectroMagnetic CALorimeter (EMCAL)

729 **Muon spectrometer** is placed in the forward pseudo-rapidity region ( $-4.0 < \eta < -2.5$ ) and consists of a dipole magnet and tracking and trigger chambers. It is optimized to  
 730 reconstruct heavy quark resonances (such as  $J/\Psi$  through their  $\mu^+\mu^-$  decay channel) and  
 731 single muons.

733 **Forward detectors** are placed in the high pseudo-rapidity region (small angles with  
 734 respect to the beam pipe). They are small and specialized detector systems used for  
 735 triggering or to measure global event characteristics. They are:

- Time Zero (T0) to measure the event time with precision of the order of tens of picoseconds, as needed by TOF
- VZERO (V0) to reject the beam-gas background and to trigger minimum bias events
- Forward Multiplicity Detector (FMD) to provide multiplicity information over a large fraction of the solid angle ( $-3.4 < \eta < -1.7$  and  $1.7 < \eta < 5$ )
- Photon Multiplicity Detector (PMD) to measure the multiplicity and the spatial distribution of photons on an event-by-event basis in the  $2.3 < \eta < 3.7$  region
- Zero Degree Calorimeter (ZDC) to measure and trigger on the impact parameter. The ZDC consists of two calorimeters, one for neutrons (ZDC:ZN) and one for protons (ZDC:ZP), and includes also an electromagnetic calorimeter (ZEM)

747 The ALICE global coordinate system [33] is a right-handed orthogonal Cartesian system  
 748 with the origin X, Y, Z = 0 at the centre of the detector. The three Cartesian axes are  
 749 defined as follows: the X axis pointing towards the centre of the LHC, the Y axis pointing  
 750 upward and the Z axis parallel to the local mean beam line pointing in the direction opposite

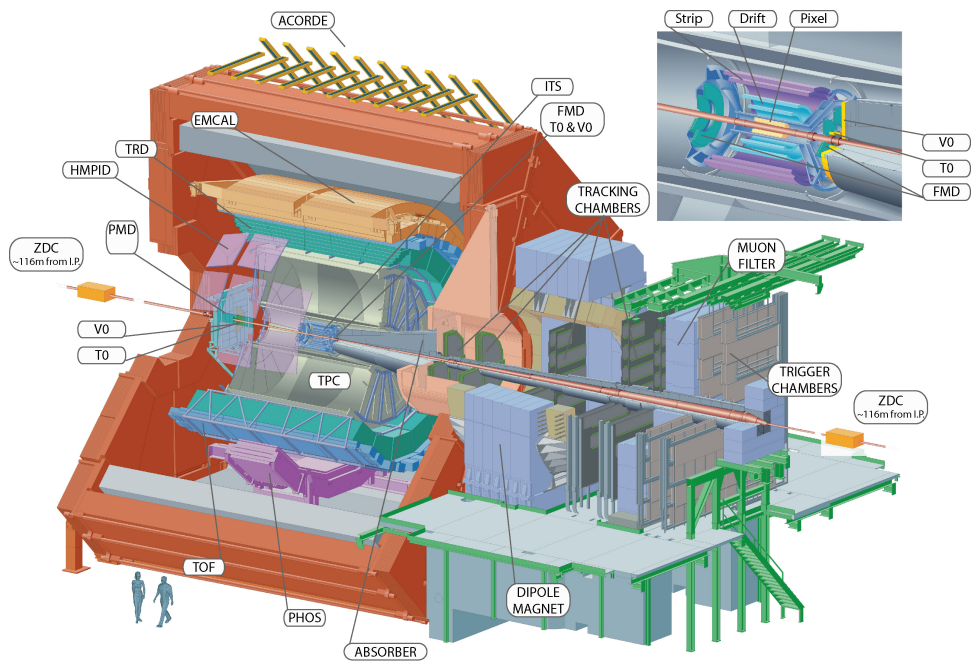


Figure 13: The ALICE detector

751 to the muon spectrometer. The azimuthal angle increases counter-clockwise from the  
752 positive X axis ( $\Phi = 0$ ) to the positive Y axis ( $\Phi = \pi/2$ ) with the observer standing at  
753 positive Z and looking at negative Z; the polar angle increases from the positive Z axis ( $\theta$   
754 = 0) to the X-Y plane ( $\theta = \pi/2$ ) and to the negative Z axis ( $\theta = \pi$ ).

755 In the following Sections more specific descriptions of the detectors used in the identifi-  
756 cation of the  $\Xi(1530)^0$  baryons and in the determination of the characteristics of typical  
757 collisions will be given.

758

### 759 ITS

760 The ITS [32] (Figure 14) is the barrel detector closest to the beam pipe. Its main goals  
761 are:

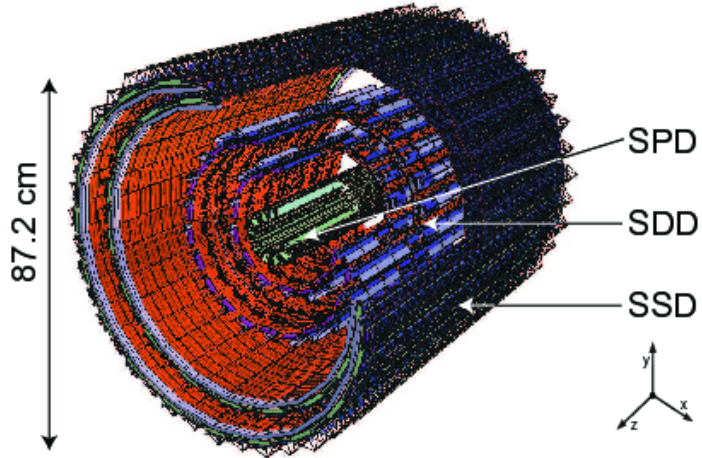


Figure 14: Schematic view of the ITS [4]

761

- 762 • to contribute with the TPC to the global tracking of ALICE by improving the angle  
763 and momentum resolution
- 764 • to reconstruct the position of the primary interaction vertex
- 765 • to reconstruct secondary vertices from decays of heavy-flavor and strange particle  
766 decays;
- 767 • to track and identify particles with momentum below  $100 \text{ MeV}/c^2$
- 768 • to improve the momentum, impact parameter and angle resolution for the measure-  
769 ment of high  $p_T$  particles performed with the TPC

- 770 • to reconstruct particles traversing dead regions of the TPC

771 The ITS surrounds the beam pipe (which is a 800  $\mu\text{m}$  thick cylinder with an outer  
 772 diameter of 2.9 cm) and consists of six cylindrical layers of silicon detectors located at radii  
 773 between 4 cm and 43 cm. Due to the high track density, the two innermost layers are  
 774 Silicon Pixel Detectors (SPD) which guarantee a high granularity. They are followed by  
 775 two layers of Silicon Drift Detectors (SDD), while the two outmost layers are double-sided  
 776 Silicon micro-Strip Detectors (SSD).

777 Since the momentum and impact parameter resolutions for low momentum particles  
 778 are dominated by multiple scattering effects, the amount of material in the active volume  
 779 has been minimized as much as possible. The granularity of the detector was optimized to  
 780 keep the occupancy low in all the layers. With the technology chosen, the ITS detectors  
 781 reach a spatial resolution of the order of a few tens of  $\text{m}$  resulting in a resolution on the  
 782 impact-parameter<sup>5</sup> better than 70  $\text{m}$  in the  $r$  plane for  $p_T > 1 \text{ GeV}/c$  and thus well suited  
 783 for the reconstruction of heavy-flavor decays (see Figure 15).

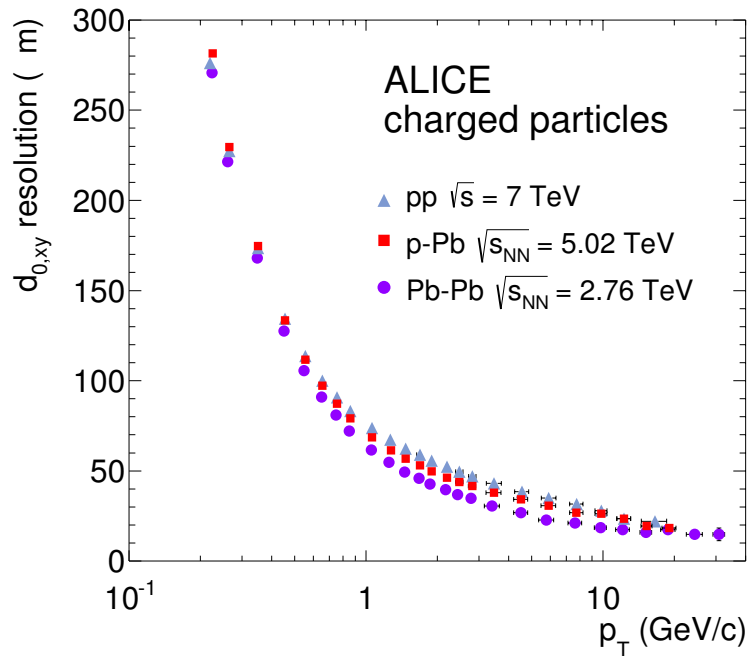


Figure 15: Track impact parameter resolution in the transverse plane ( $r\phi$ ) vs  $p_T$  for charged particle

784 **TPC**

785 The TPC [34] (Figure 16) is the main tracking detector of the central barrel, optimized

786 to provide, together with the other central barrel detectors, charged-particle momentum  
 787 measurements with good two-track separation, particle identification and vertex determina-  
 788 tion. The TPC was designed for an excellent tracking performance in the high multiplicity  
 789 environment of Pb–Pb collisions. For this reason, it was chosen to be a drift chamber,  
 790 cylindrical in shape, 5 m long, with the inner radius ( $r_{in} \sim 85$  cm) determined by the  
 791 maximum acceptable track density, and the external one ( $r_{ext} \sim 250$  cm) by the minimum  
 792 track length for which  $dE/dx$  resolution is  $< 10\%$ . The TPC volume is filled with  $90\text{ m}^3$  of  
 793 Ne/CO<sub>2</sub>/N<sub>2</sub> (90/10/5). The readout planes are divided in 18 sectors in which multi-wire  
 794 proportional chambers (with cathode pad readout) are housed. Because of its good  $dE/dx$   
 795 resolution, the TPC can identify particles with  $p_T < 1\text{ GeV}/c$  on a track-by-track basis.

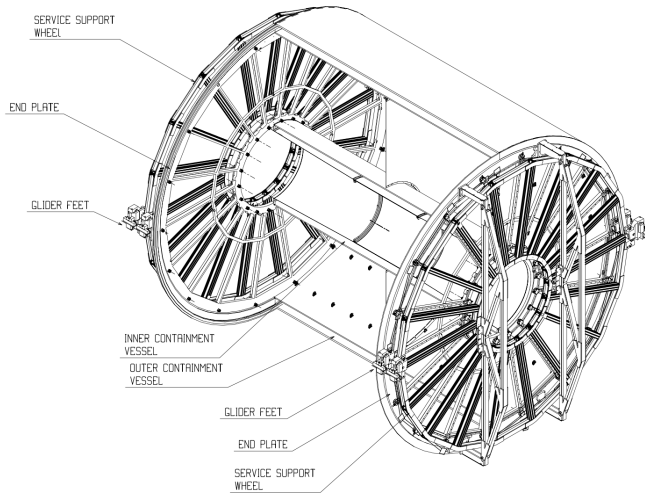


Figure 16: Schematic view of the TPC

796 Charged particles traveling through the TPC ionize the detector's gas; the measure-  
 797 ment of this loss of energy is what we need to identify a particle. The physics observable  
 798 in this case is the energy loss per unit length, within the matter crossed by the charged  
 799 particle, which we call specific energy loss, also denoted by  $dE/dx$ . This is described by  
 800 the Bethe–Bloch equation, 5, that highlights the key of the identification technique: this  
 801 observable depends only on the charge and on velocity ( $\beta$ ) of the particle, which, in turn,  
 802 depends only on the momentum and the mass of the ionizing particle. Since momentum is  
 803 already known due to track curvature and charge is unitary for most measured tracks, mea-  
 804 suring the  $dE/dx$  allows us to indirectly determine mass and thus determine the particle  
 805 species. The Bethe-Bloch equation gives the mean specific energy loss:

$$-\langle \frac{dE}{dx} \rangle = k_1 \cdot z^2 \frac{Z}{A} \cdot \frac{1}{\beta^2} \left[ \frac{1}{2} \ln(k_2 \cdot m_e c^2 \cdot \beta^2 \gamma^2) - \beta^2 + k_3 \right] \quad (5)$$

806 where  $\beta\gamma = p/Mc$  and: Z: atomic number of the ionized gas (in this case Ne/CO<sub>2</sub>/N<sub>2</sub>)  
 807 A: mass number of the ionized gas (g/mol)  
 808 m<sub>e</sub>: electron mass  
 809 z: electric charge of the ionizing particle in unit of electron charge e  
 810 M: ionizing particle mass  
 811 p: ionizing particle momentum  
 812 β: ionizing particle velocity normalized to the light velocity c  
 813 γ = 1/√(1 - β<sup>2</sup>), Lorentz factor  
 814 k<sub>1</sub>, k<sub>2</sub>, k<sub>3</sub>: constants depending on the ionized medium  
 815

816 For a given ionizing particle mass hypothesis, a given momentum and a given length  
 817 of the trajectory in the ionizing medium, the total charge deposited along the trajectory  
 818 is subject to statistical fluctuations. This random variable follows a Landau distribution,  
 819 that give us the opportunity to measure the mean value  $hdE/dx$ . The long tail of the  
 820 Landau distribution is usually truncated at 50%-70% of the collected signal.

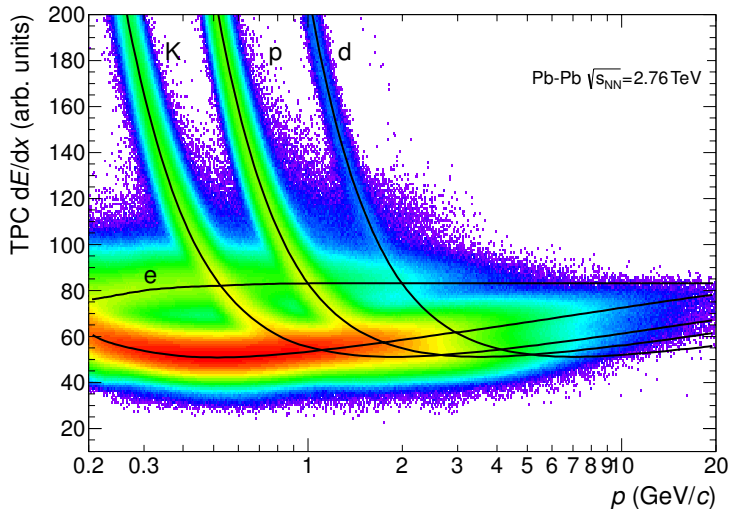


Figure 17: Specific energy loss (dE/dx) in the TPC vs. particle momentum in Pb–Pb collisions at  $\sqrt{s_{NN}} = 2.76$  TeV. The different bands characteristic for  $e^\pm$ ,  $\pi^\pm$ ,  $K^\pm$ ,  $p^\pm$  are clearly visible. These are the evidence of the statistical distribution of the measured energy loss around the expected mean value. The expected value correspond to the prediction by a Bethe–Bloch experimental parametrization (superimposed as black lines in the Figure). For a track

821 The specific energy loss in the TPC as a function of momentum is shown in Figure  
 822 17. The different bands characteristic for  $e^\pm$ ,  $\pi^\pm$ ,  $K^\pm$ ,  $p^\pm$  are clearly visible. These  
 823 are the evidence of the statistical distribution of the measured energy loss around the  
 824 expected mean value. The expected value correspond to the prediction by a Bethe–Bloch  
 825 experimental parametrization (superimposed as black lines in the Figure). For a track

826 within the TPC the relevant quantity to be considered for PID is the difference between  
 827 the measured specific energy loss and the corresponding predicted value, by the Bethe-  
 828 Bloch parametrization for a given measured momentum. If normalized to the resolution  
 829 of the  $dE/dx$  measurement in the TPC, this difference could be expressed in number of  
 830  $\sigma$ (see Equation 6). In this way it is possible to estimate more quantitatively the goodness  
 831 of a mass hypothesis. This also gives us the possibility to choose the strictness we want to  
 832 adopt in the identification of a particle ( $n_\sigma$  ,  $n = 2, 3, 4$ ):

$$n_\sigma = \frac{(dE/dx)_{measured} - (dE/dx)_{Bethe-Bloch}}{\sigma_{TPC}} \quad (6)$$

## V0

833 The VZERO detector [35] consists of two segmented arrays of plastic scintillator counters,  
 834 called VZERO-A and VZERO-C, placed around the beam-pipe on either side of the IP:  
 835 one at  $Z = 340$  cm, covering the pseudo-rapidity range [2.8; 5.1], and the other at  $Z = -90$   
 836 cm (in front of the absorber), covering the pseudo-rapidity range [-3.7; -1.7]. They consist  
 837 of 32 counters distributed in four rings, each divided in eight 45 sectors. Each counter  
 838 is made of scintillator material embedded with WaveLength Shifting fibers. Clear fibers  
 839 collect and transport the signal to photomultipliers 3 - 5 m far from the detector, inside  
 840 the L3 magnet. The counters have a time resolution better than 1 ns. Their response is  
 841 recorded in a time window of 25 ns around the nominal beam crossing time. The VZERO  
 842 has an important role in rejecting background from beam-gas collisions (see, Figure 18)  
 843 exploiting the relative time-of-flight measurement between the two arrays: when the beam-  
 844 gas collision takes place outside the region between the two arrays, particles arrive 6 ns  
 845 before or after the time of a beam-beam collision.

846 The VZERO is a trigger detector that will provide a minimum-bias trigger for all  
 847 colliding systems to the central barrel detectors and three centrality triggers in p-Pb and  
 848 Pb-Pb collisions (multiplicity, central and semi-central).

849 The first parameter to be determined in A-A(p-A) collisions is the centrality(multipliciy).  
 850 This is defined according to the value of the impact parameter,  $b$ , and provides a geomet-  
 851 rical scale of the overlapping region between the colliding nuclei: a collision will be defined  
 852 from central to peripheral, as the impact parameter increases. The centrality of a collision  
 853 is not directly available and must be deduced from a combination of experimentally mea-  
 854 sured quantities and Monte Carlo simulations. There are a number of observables that can  
 855 be measured and used as centrality estimators. The charged-particle multiplicity  $N_{ch}$  and  
 856 the transverse energy  $E_T$  measured around mid-rapidity are measurable quantities related  
 857 to the energy deposited in the interaction region (these are therefore related to  $N_{part}$ ).  
 858 These variables increase significantly increasing the centrality of the collisions. Another  
 859 measurable quantity to estimate the centrality is the zero-degree energy EZDC, namely  
 860 the energy carried by spectator nucleons  $N_{spec} = 2A - N_{part} = E_{ZDC}/E_A$ , where  $E_A$  is  
 861 the beam energy per nucleon. Typically a measured distribution of one of the previous  
 862 observables is mapped to the corresponding distribution obtained from phenomenological

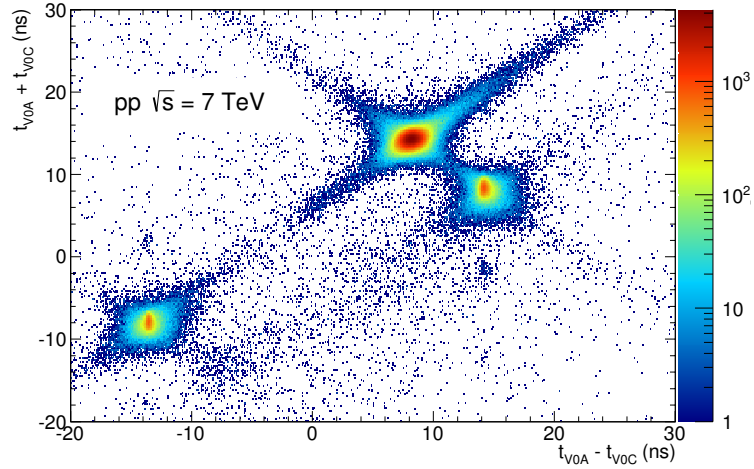


Figure 18: Correlation between the sum and difference of signal times in V0A and V0C. Three classes of events collisions at (8.3 ns, 14.3 ns), background from Beam 1 at (-14.3 ns, -8.3 ns), and background from Beam 2 at (14.3 ns, 8.3 ns) can be clearly distinguished.

864 Glauber calculations. The Glauber model [36, 37] uses a semi-classical approach: the A?A  
 865 collision is assumed to be an incoherent superposition of N elementary nucleon- nucleon  
 866 collisions. The main parameters of the model are the inelastic nucleon- nucleon collision  
 867 cross-section  $\sigma_n$  and the nuclear density distribution  $\rho(r)$ . In practice, the simulated dis-  
 868 tribution well reproduce the measured distribution or the latter is fitted with an analytical  
 869 function. The experimental distribution can then be divided in classes with sharp cuts on  
 870 the measured observable ( $E_{ZDC}$ ,  $E_T$  or  $N_{ch}$ ). These "centrality" classes will correspond to  
 871 well defined percentage of the integral of the distribution. A given centrality class in the  
 872 measured distribution, corresponds to the same class in the simulated distribution, where  
 873 the main geometrical variables ( $N_{part}$ ,  $N_{coll}$  and  $T_{AA}$ ) can be determined. The number of  
 874 classes that can be defined depends on the resolution achievable on the selection variable.  
 875 In the analysis described in this thesis the centrality(multiplicity) estimation is based on  
 876 the measurement of the multiplicities from the VZERO scintillators [38][39]. This is the  
 877 method that achieve the best centrality resolution: it ranges from 0.5% in central to 2%  
 878 in peripheral collisions. Other methods, as the ones based on the  $E_{ZDC}$  measurement or  
 879 based on the estimate of the number of tracks in the SPD or TPC, are used to asses a  
 880 systematic uncertainty on the centrality determination. The distribution of the VZERO  
 881 amplitudes is shown in Figure 19 where the centrality(multiplicity) percentiles are also  
 882 indicated.

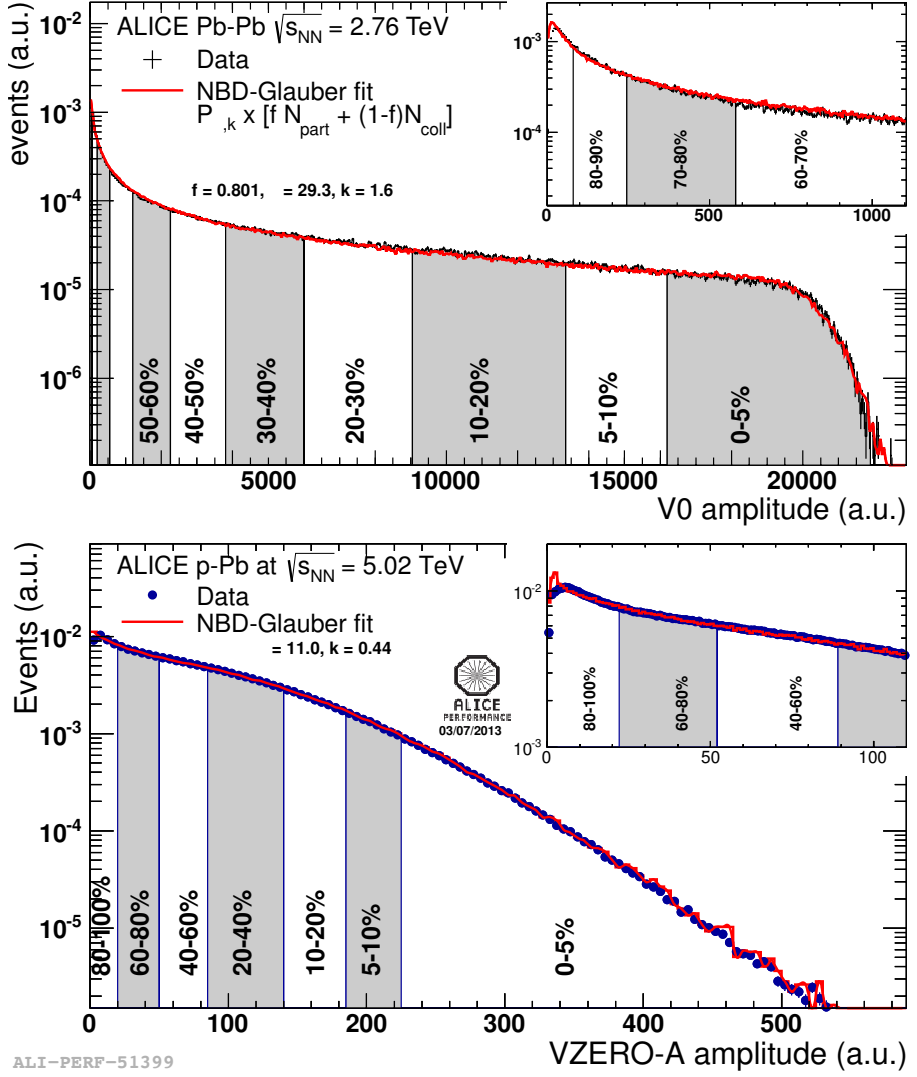


Figure 19: Distribution of the V0 amplitude (sum of V0A and V0C in top, V0A in bottom). The inset shows a magnified version of the most peripheral region.

883 **4.2.2 Data Acquisition (DAQ) and trigger system**

884 The architecture of data acquisition is shown in Figure 20. The tasks of the ALICE DAQ  
 885 system are the assembly of event informations from individual detectors into complete  
 886 events (event building) as well as buffering and export of assembled events to permanent  
 887 storage. The DAQ is designed to process a data rate up to 1.25 GB/s in heavy-ion runs.  
 888 Event building is done in two steps. Data from the detectors is received by Detector Data  
 889 Links (DDLs) on Local Data Concentrators (LDCs). The LDCs assemble the data into  
 890 sub-events that are then shipped to Global Data Collectors (GDCs). A GDC re- ceives all  
 891 sub-events from a given event and assembles them into a complete event. These events are  
 892 subsequently stored on a system called Transient Data Storage (TDS).

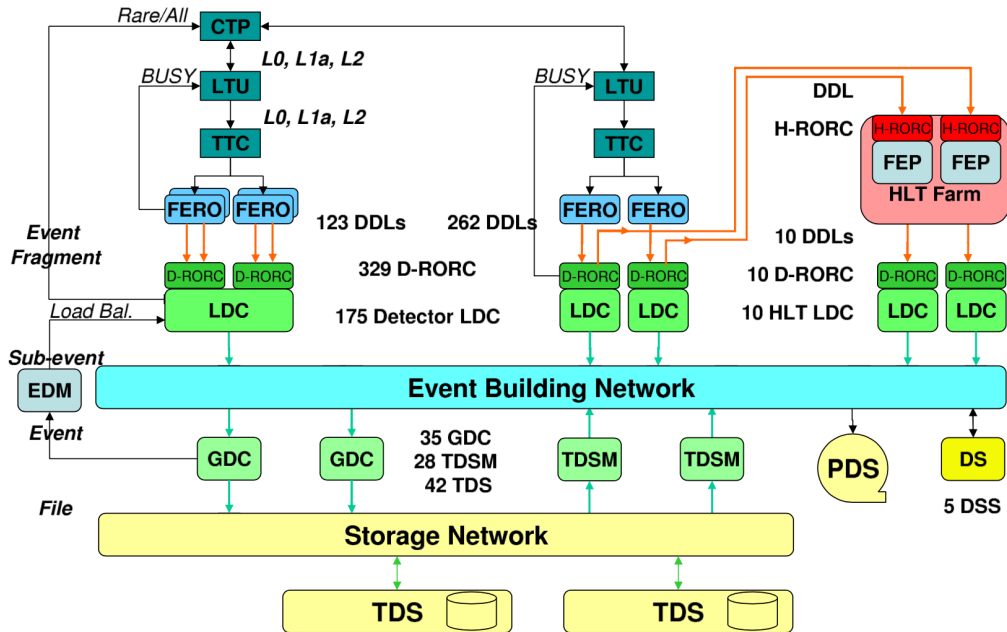


Figure 20: The overall architecture of the ALICE DAQ and the interface to the HLT system.

893 ALICE can simultaneously take data in several partitions, where a set of detec-  
 894 tors can store their outputs. Since a partition is a group of commonly controlled detectors, a  
 895 given detector can only be active in one partition at a time. The ac- tive detectors in a  
 896 given partition may be assigned to data taking groups called clusters, for which triggers

897 can be defined. Therefore, upon a trigger only a sub-set of the whole partition may  
898 be read out. Furthermore, a triggering detector does not have to be necessarily part of  
899 the partition. ALICE has a two-layer trigger architecture [40]. The low-level trigger is a  
900 hardware trigger called Central Trigger Processor (CTP). The High-Level Trigger (HLT)  
901 is implemented as a pure software trigger. The CTP combines inputs from different trigger  
902 sources, namely the various detectors. These inputs are single signals, like a hit in the  
903 detector, or, can be the result of fast calculation performed directly in the detectors. The  
904 HLT allows the implementation of sophisticated logic for the triggering. In contrast to the  
905 CTP which governs the readout of the detectors, the HLT receives a copy of the data read  
906 out from the detectors and processes them. The hardware trigger combines the trigger  
907 signals of the various detectors to decide if an event is accepted, that means it is read out  
908 and written to disk. Several trigger levels reduce the event rate depending on the input  
909 signals. The first level, called L0, is delivered after 1.2 ?s, while the second, called L1,  
910 after 6.5 ?s. The final trigger, L2, is delivered after 100 ?s, upon completion of the drift  
911 time in the TPC. Only after an L2 trigger the event is finally stored. The rates of different  
912 trigger classes are very different. By definition minimum-bias triggers have the highest  
913 rate; other triggers that look for rare signals are characterized by much lower rates. In  
914 order to cope with different scenarios, downscaling factors can be applied to the trigger  
915 classes individually, i.e. only every nth event fulfilling the trigger condition is read out. The  
916 total recording rate is limited by the maximum bandwidth of data that can be recorded  
917 to disk and tape. The ALICE software trigger, called HLT, is a farm of multiprocessor  
918 computers. The aim is to have about 1000 PCs processing the data in parallel allowing  
919 an online analysis of the events. A trigger decision comes from the analysis of a more  
920 comprehensive set of information than what happens for the hardware trigger, giving the  
921 possibility to apply more sophisticated triggers. Examples include triggers on high energy  
922 jets or on muon pairs. Furthermore, the HLT can significantly reduce the event size by  
923 selecting regions of interest (partial readout of detectors) and by further compression of the  
924 data. The HLT receives a copy of the raw data and performs per detector reconstruction,  
925 partly aided by hardware coprocessors. Subsequently, the trigger decision is based on the  
926 global reconstructed event. In the same step a region of interest can be selected. In the  
927 last optional step, if the trigger decision is positive, the data are compressed. The trigger  
928 decision, partial readout information, compressed data, and the re-construction output  
929 is sent to LDCs and subsequently processed by the DAQ. In terms of the overall DAQ  
930 architecture, data sent by HLT is treated like stemming from a detector.

931   **4.2.3 ALICE offline software frame work**

932   The required computing resources for the reconstruction and analysis of the raw data as  
933   well as the production of simulated events needed for the understanding of the data exceed  
934   the computing power of single institutes and even centers like CERN. Therefore, institutes  
935   that are part of the Collaboration also provide storage and computing resources. Distribu-  
936   tion of the data for reconstruction and analysis cannot be performed manually and this  
937   led to the need for an automated system. The concept of a decentralized computing model  
938   called Grid [41] was identified as a solution.

939

940   *The AliEn Framework*

941   The Grid paradigm implies the unification of resources of distributed computing center,  
942   in particular computing power and storage, to provide them to users all over the World.  
943   It allows computing center to offer their resources to a wider community and the local re-  
944   sources to be shared by an entire collaboration. Software that implements the Grid concept  
945   is called Grid middleware. ALICE has developed a Grid middleware called AliEn [42] since  
946   2001. An ALICE user employs AliEn to connect to the ALICE Grid which is composed  
947   of a combination of general services that are provided by many Grid middleware solutions  
948   and ALICE-specific services provided by AliEn. Parts of the ALICE Grid are: i) a global  
949   file catalog that is a directory of files in storage elements distributed over the Globe, ii)  
950   the automatic matching of jobs for execution to a suitable location in one of the connected  
951   sites, iii) a shell-like user interface and iv) API9 services for the ROOT framework [43].

952

953   *AliRoot Framework*

954   AliRoot [32] is the offline framework for simulation, alignment, calibration, reconstruction,  
955   visualization, quality assurance, and analysis of experimental and simulated data. It is  
956   based on the ROOT framework. Most of the code is written in C++ with some parts in  
957   Fortran that are wrapped inside C++ code. Re-usability and modularity are the basic  
958   features of the AliRoot framework. Modularity allows parts of the code to be replaced,  
959   with minimum or no impact on the rest (for example changing the event generator, the  
960   transport Monte Carlo or the reconstruction algorithms). This is achieved implementing  
961   abstract interfaces. In addition codes for each detector subsystem are independent modules  
962   with their specific code for simulation and reconstruction and the code can be developed  
963   concurrently with minimum interference. Re-usability is meant to maintain a maximum  
964   amount of backward compatibility as the system evolves.

965   The central module of the AliRoot framework is STEER (Figure 21) which provides  
966   several common functions such as: steering of program execution for simulation, reconstruc-  
967   tion and analysis; general run management, creation and destruction of data structures,  
968   initialization and termination of program phases; base classes for simulation, event genera-  
969   tion, reconstruction, detectors elements. For event simulation the framework provides the  
970   following functionality:

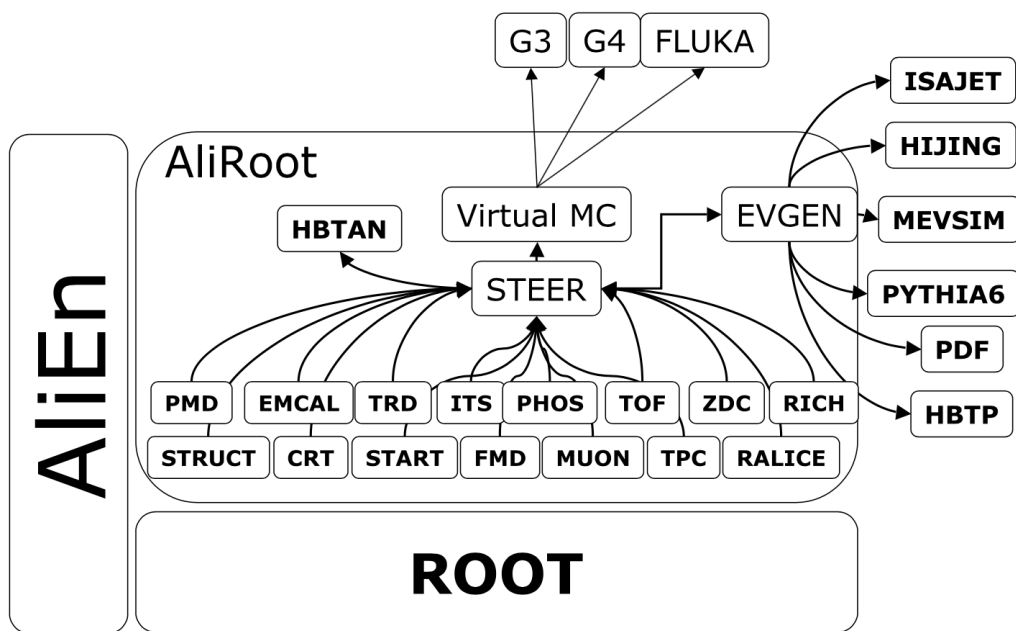


Figure 21: Schematic view of the AliRoot framework

971    **5 Measurement of  $\Xi(1530)^0$  production in p–Pb and Pb–Pb**

972    The measurement of resonance production in p–Pb collisions helps to disentangle cold  
973    nuclear matter effects from genuine hot medium effects and contribute to the study of  
974    the system size dependence of re-scattering in the hadronic phase. And the measurement  
975    in ultra-relativistic heavy-ion collisions such as Pb–Pb collisions, provide information on  
976    the properties of hadronic medium and different stage of its evolution. In order to study  
977    the particle production mechanism in the hadronic phase between the chemical and ki-  
978    netic freeze-out, the  $\Xi(1530)^0$  resonance production at mid-rapidity ( $-0.5 < y_{\text{CMS}} < 0$ ) is  
979    measured in p–Pb collisions  $\sqrt{s_{\text{NN}}} = 5.02$  TeV and in Pb–Pb collisions with  $|y| < 0.5$  at  
980     $\sqrt{s_{\text{NN}}} = 2.76$  TeV with the ALICE experiment, via the reconstruction of its hadronic decay  
981    into  $\Xi\pi$ .

982    **5.1  $\Xi(1530)^0$  -reconstruction**

983    The  $\Xi^{*0}$  production in p–Pb and Pb–Pb collisions at mid-rapidity has been studied in dif-  
984    ferent multiplicity classes, from very central to peripheral collisions. The analysis strategy  
985    is based on the invariant mass study of the reconstructed pairs (referred to as the candi-  
986    dates) whose provenance could be the decay of a  $\Xi^{*0}$  baryon into charged particles. The  
987    decay products (also called daughters in the text) are identified as oppositely charged  $\Xi$  and  
988     $\pi$  among the tracks reconstructed in the central barrel. The event selection, track selec-  
989    tion and the particle identification strategy is described. The raw signal yield is extracted  
990    by fitting the background-subtracted invariant mass distribution in several transverse mo-  
991    mentum intervals. In order to extract the  $p_{\text{T}}$ -dependent cross section, these yields are  
992    corrected for efficiency. The  $p_{\text{T}}$ -dependent correction due to the detector acceptance and  
993    reconstruction efficiency,  $(\text{Acc} \times \epsilon_{\text{rec}})(p_{\text{T}})$ , is computed from a Monte Carlo simulation.  
994    The absolute normalisation is then performed, by dividing for the number of the events in  
995    each multiplicity and centrality classes.

996    **5.1.1 Data sample and event selection**

997    A description of the ALICE detector and of its performance during the LHC Run 1 (2010–  
998    2013) can be found in [32, 44]. The data sample in the analysis from Pb–Pb collisions with  
999    energy of  $\sqrt{s_{\text{NN}}} = 2.76$  obtained during 2011 and the sample of p–Pb run at  $\sqrt{s_{\text{NN}}} = 5.02$   
1000    TeV was recorded in 2013.

1001    Due to the asymmetric energies of the proton (4 TeV) and lead ion (1.57 A TeV) beams,  
1002    the centre-of-mass system in the nucleon-nucleon frame is shifted in rapidity by  $\Delta y_{\text{NN}} =$   
1003    0.465 towards the direction of the proton beam with respect to the laboratory frame of  
1004    the ALICE detector [6]. For the analysed p–Pb data set, the direction of the proton beam  
1005    was towards the ALICE muon spectrometer, the so-called “C” side, standing for negative  
1006    rapidities; conversely, the Pb beam circulated towards positive rapidities, labelled as “A”

1007 side in the following. The analysis in this paper was carried out at midrapidity, in the  
1008 rapidity window  $-0.5 < y_{\text{CMS}} < 0$ .

1009 The minimum-bias trigger during the p–Pb run was configured to select events by  
1010 requiring a logical OR of signals in V0A and V0C [44], two arrays of 32 scintillator detectors  
1011 covering the full azimuthal angle in the pseudo-rapidity regions  $2.8 < \eta_{\text{lab}} < 5.1$  and  
1012  $-3.7 < \eta_{\text{lab}} < -1.7$ , respectively [45]. In the data analysis it was required to have a  
1013 coincidence of signals in both V0A and V0C in order to reduce the contamination from  
1014 single-diffractive and electromagnetic interactions. Out of this sample in p–Pb collision  
1015 events about 109.3 million events, 93.9 million events satisfy the following selection criteria  
1016 and have been actually used for the analysis.

1017 The Pb–Pb collisions data sample was selected by online centrality trigger requiring a  
1018 signal in the forward V0 detectors[39] to record enhanced data in central collision. The  
1019 data consists of 24.8 million events in most central collisions (0-10%), 21.8 million events in  
1020 semi-central collisions (10-50%) and 3.5 million events with minimum-bas trigger (0-90%).  
1021 Among 49.6 million events in total, 43.0 million events have been analyzed as passed the  
1022 criteria below.

- 1023     • Events with z-coordinate of primary vertex ( $V_z$ ) falling within  $\pm 10$  cm from the  
1024       interaction point
- 1025     • Rejection of pile-up event
- 1026     • Requiring primary tracks to have at least one hit in one of the two innermost layers  
1027       of the ITS (silicon pixel detector, SPD)
- 1028     • p–Pb: multiplicity ranges in percentile (V0A): 0-20%, 20-40%, 40-60%, 60-100% and  
1029       MB(0-100%)
- 1030     • Pb–Pb: centrallity classes (V0A and V0C): 0-10%, 10-40%, 40-80% and MB (0-80%)

1031 The distribution of the vertex z position of the accepted events in p–Pb collision is  
1032 reported on left panel in Figure 22 and corresponding figure but obtained from Pb–Pb  
1033 collisions is shown on right panel in Figure. 22. Events with  $|V_z| < 10$  cm have been used  
1034 to ensure a uniform acceptance in the central pseudo-rapidity region,  $|\eta| < 0.8$ , where the  
1035 analysis is performed. This cut reduces the total number of events to 97.5 million events,  
1036 that is the  $\sim 89.2\%$  of the initial sample in p–Pb collisions and 43.04 million events which  
1037 is  $\sim 86.8\%$  of the initial sample in Pb–Pb collisions are survived.

1038 Fig. 23 shows the multiplicity distribution of the accepted events in p–Pb collision  
1039 divided in bins of percentile. The each color on the histogram indicate the multiplicity  
1040 ranges used in this analysis. Corresponding events for each multiplicity range are in Table  
1041 8.

1042 The distribution of centrality in each trigger used to select the events in Pb–Pb collision  
1043 is shown in Fig. 24 and the reason why the centrality has step structure is that there are

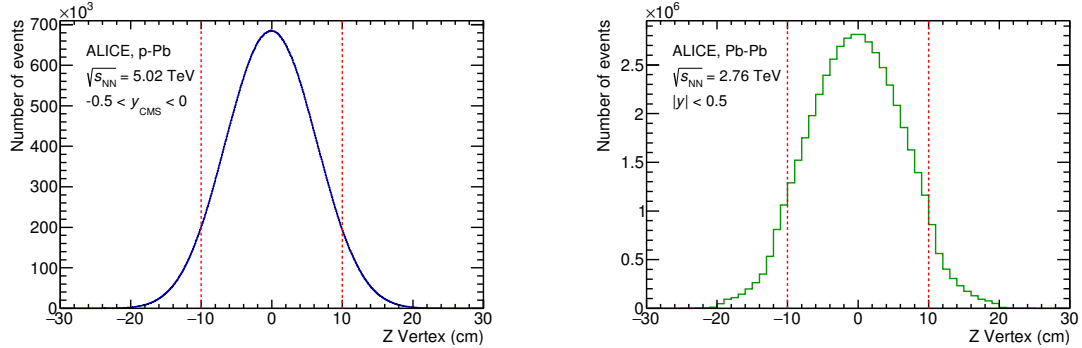


Figure 22: Vertex-z coordinate distribution of the accepted events in p–Pb collision(Left) and in Pb–Pb collisions(Right). The red dashed line indicates vertex cut

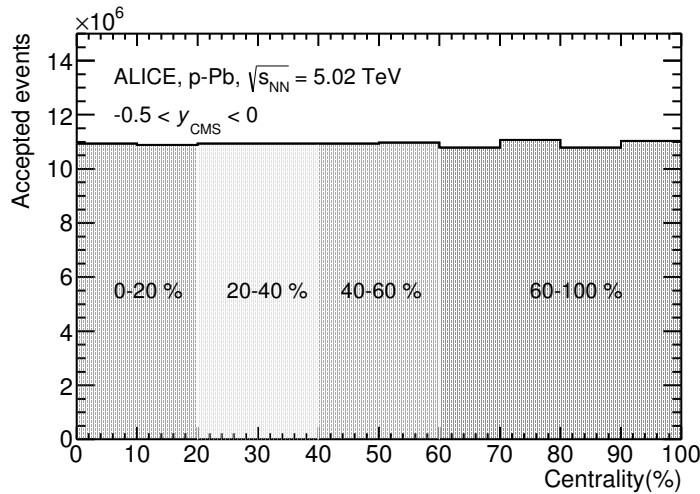


Figure 23: Multiplicity distribution of accepted events in p–Pb collision in percentile. The each color and labels define the four intervals in which the analysis is performed.

1044 three different trigger classes classified by the amplitude threshold on VZERO detector.  
 1045 Because the distribution of events as function of centrality is not a flat, this may lead to  
 1046 additional bias, in particular when one needs to combine the results from different triggers.  
 1047 For example, events from 40-80% centrality bin have bias with high statistics in 40-60%. In  
 1048 order to avoid this effect, we have applied a flattening procedure to have flat distribution  
 1049 of events as function of centrality. A brief explanation of the method is below :

- 1050     1. Histograms are obtained for the effective mass distribution in 1% centrality bins and  
 1051       for the centrality distribution  
  
 1052     2. The effective mass distributions are scaled in each 1% centrality bin by a factor:  
 1053       Factor = N<sub>event</sub> in 20-40% / 20 / N<sub>event</sub> in current 1% bin  
  
 1054     3. Each bin in the centrality distribution is scaled using the factor described above  
  
 1055     4. Histograms are added for centrality bins of interest: 0-10%, 10-40%, 40-80%, 0-80%

1056     The resulting number of events in each centrality classes is summarized in Table 8.

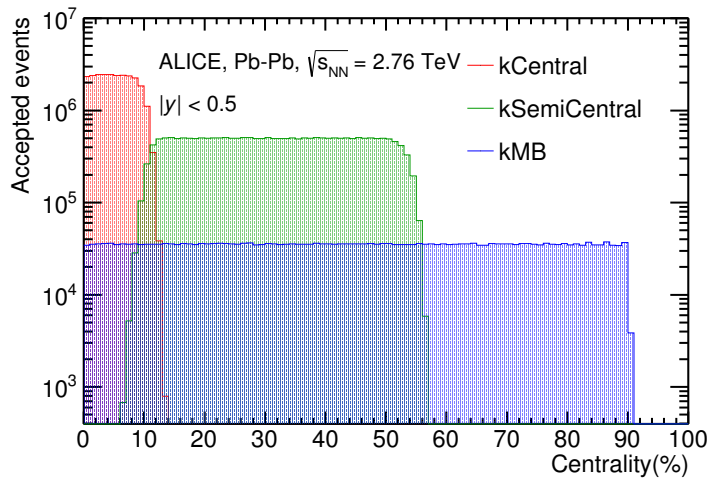


Figure 24: Centrality distribution of three different trigger classes.

p-Pb	0-20%	$21.82 \times 10^6$
	20-40%	$21.86 \times 10^6$
	40-60%	$21.91 \times 10^6$
	60-100%	$43.68 \times 10^6$
Pb-Pb	0-10%	$5.58 \times 10^6$
	10-40%	$16.73 \times 10^6$
	40-80%	$22.31 \times 10^6$

Table 8: Number of accepted and analyzed events per multiplicity/centrality interval

### 1057 5.1.2 Track and topological selection

1058 In comparison with the  $\Xi^{*0}$  analysis carried out in pp collisions at  $\sqrt{s} = 7$  TeV [8], track  
 1059 and topological selections were revised and adapted to the p-Pb dataset. Pions from strong  
 1060 decays of  $\Xi^{*0}$  were selected according to the criteria for primary tracks. As summarized  
 1061 in Table 9, all charged tracks were selected with  $p_T > 0.15$  GeV/c and  $|\eta_{\text{lab}}| < 0.8$ ,  
 1062 as described in Ref. [44]. The primary tracks were chosen with the Distance of Closest  
 1063 Approach (DCA) to PV of less than 2 cm along the longitudinal direction ( $\text{DCA}_z$ ) and  
 1064 lower than  $7\sigma_r$  in the transverse plane ( $\text{DCA}_r$ ), where  $\sigma_r$  is the resolution of  $\text{DCA}_r$ . The  $\sigma_r$   
 1065 is strongly  $p_T$ -dependent and lower than 100  $\mu\text{m}$  for  $p_T > 0.5$  GeV/c [44]. To ensure a good  
 1066 track reconstruction quality, candidate tracks were required to have at least one hit in one  
 1067 of the two innermost layers (SPD) of the ITS and to have at least 70 reconstructed points in  
 1068 the Time Projection Chamber (TPC), out of a maximum of 159. The Particle IDentification  
 1069 (PID) criteria for all decay daughters are based on the requirement that the specific energy  
 1070 loss ( $dE/dx$ ) is measured in the TPC within three standard deviations ( $\sigma_{\text{TPC}}$ ) from the  
 expected value ( $dE/dx_{\text{exp}}$ ), computed using a Bethe-Bloch parametrization [44].

Common track selections	$ \eta_{\text{lab}} $	$< 0.8$
	$p_T$	$> 0.15$ GeV/c
	PID $ (\text{d}E/\text{d}x) - (\text{d}E/\text{d}x)_{\text{exp}} $	$< 3 \sigma_{\text{TPC}}$
Primary track selections	$\text{DCA}_z$ to PV	$< 2$ cm
	$\text{DCA}_r$ to PV	$< 7\sigma_r$ - $10\sigma_r$ ( $p_T$ )
	number of SPD points	$\geq 1$
	number of TPC points	$> 70$
	$\chi^2$ per cluster	$< 4$

Table 9: Track selections common to all decay daughters and primary track selections applied to the charged pions from decays of  $\Xi^{*0}$ .

1071  
 1072 Since pions and protons from weak decay of  $\Lambda$  ( $c\tau = 7.89$  cm [1]) and pions from weak  
 1073 decay of  $\Xi^-$  ( $c\tau = 4.91$  cm [1]) are produced away from the PV, specific topological and

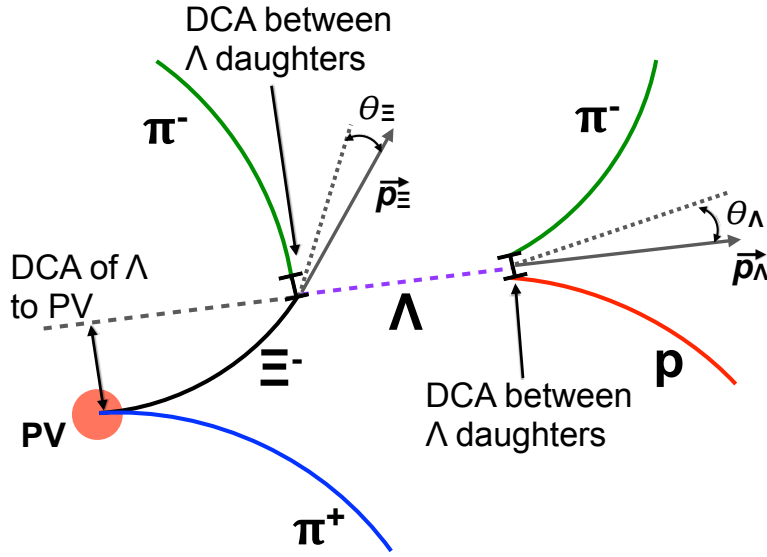


Figure 25: Sketch of the decay modes for  $\Xi^{*0}$  and depiction of the track and topological selection criteria.

1074 track selection criteria, as summarized in Table 10, were applied [7, 8, 46].

Topological cuts	p-Pb	Pb-Pb
DCA <sub>r</sub> of $\Lambda$ decay products to PV	> 0.06 cm	> 0.11 cm
DCA between $\Lambda$ decay products	< 1.4 cm	< 0.95 cm
DCA of $\Lambda$ to PV	> 0.015 cm	> 0.06
$\cos\theta_\Lambda$	> 0.875	> 0.998
$r(\Lambda)$	$0.2 < r(\Lambda) < 100$ cm	$0.2 < r(\Lambda) < 100$ cm
$ M_{p\pi} - m_\Lambda $	< 7 MeV/ $c^2$	< 7 MeV/ $c^2$
DCA <sub>r</sub> of pion (from $\Xi^-$ ) to PV	> 0.015 cm	> 0.035 cm
DCA between $\Xi^-$ decay products	< 1.9 cm	< 0.275
$\cos\theta_\Xi$	> 0.981	> 0.9992
$r(\Xi^-)$	$0.2 < r(\Xi^-) < 100$ cm	$0.2 < r(\Xi^-) < 100$ cm
$ M_{\Lambda\pi} - m_\Xi $	< 7 MeV/ $c^2$	< 7 MeV/ $c^2$

Table 10: Topological and track selection criteria.

1075 In the analysis of  $\Xi^{*0}$ ,  $\Lambda$  and  $\pi$  from  $\Xi^-$  were selected with a DCA of less than 1.9 cm  
 1076 and with a DCA<sub>r</sub> to the PV greater than 0.015 cm. The  $\Lambda$  daughter particles ( $\pi$  and p)

1077 were required to have a  $\text{DCA}_r$  to the PV greater than 0.06 cm, while the DCA between the  
1078 two particles was required to be less than 1.4 cm. Cuts on the invariant mass, the cosine of  
1079 the pointing angle ( $\theta_\Lambda, \theta_\Xi$ ) and the radius of the fiducial volume ( $r(\Lambda), r(\Xi)$ ) in Table 10  
1080 were applied to optimize the balance of purity and efficiency of each particle sample.

1081 **5.1.3 Particle identification**

1082 PID selection criteria are applied for

- 1083 1.  $\pi^\pm$  (last emitted  $\pi$ ) and proton from  $\Lambda$   
1084 2.  $\pi^\pm$  (second emitted  $\pi$ ) from  $\Xi^\pm$   
1085 3.  $\pi^\pm$  (first emitted  $\pi$ ) from  $\Xi(1530)^0$

1086 by using TPC. On TPC dE/dx versus momentum distribution,  $3\sigma$  cuts are applied to TPC  
1087 for selecting each of the particles. The TPC dE/dx selection allows to have better signal  
1088 with  $\sim 20\%$  increase of significance.

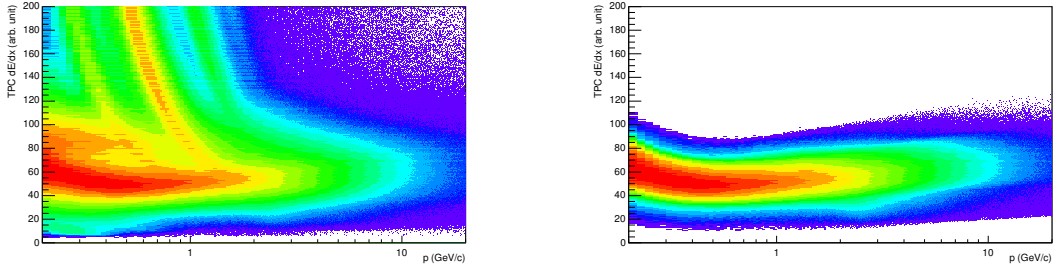


Figure 26: TPC dE/dx as function of transverse momentum for total (top) and selected first emitted  $\pi$  in  $3\sigma$  (bottom)

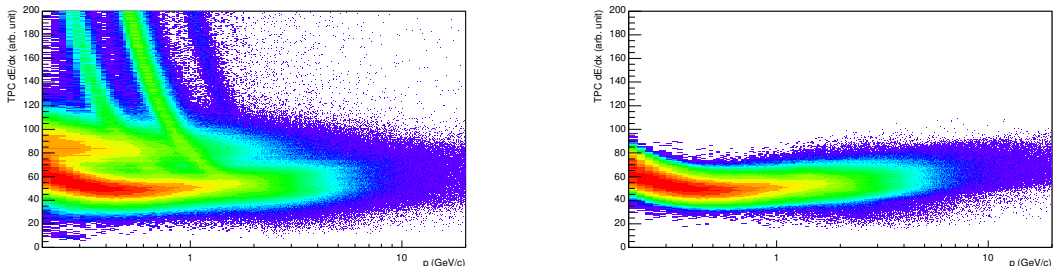


Figure 27: TPC dE/dx as function of transverse momentum for total (top) and selected second emitted  $\pi$  in  $3\sigma$  (bottom)

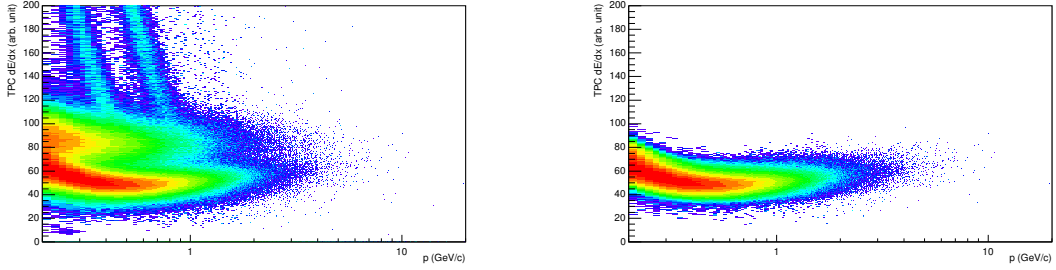


Figure 28: TPC  $dE/dx$  as function of transverse momentum for total (top) and selected last emitted  $\pi$  in  $3\sigma$ (bottom)

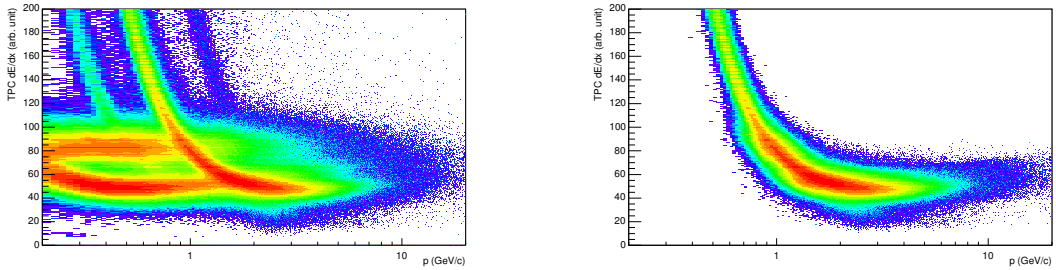


Figure 29: TPC  $dE/dx$  as function of transverse momentum for total (top) and selected proton in  $3\sigma$ (bottom)

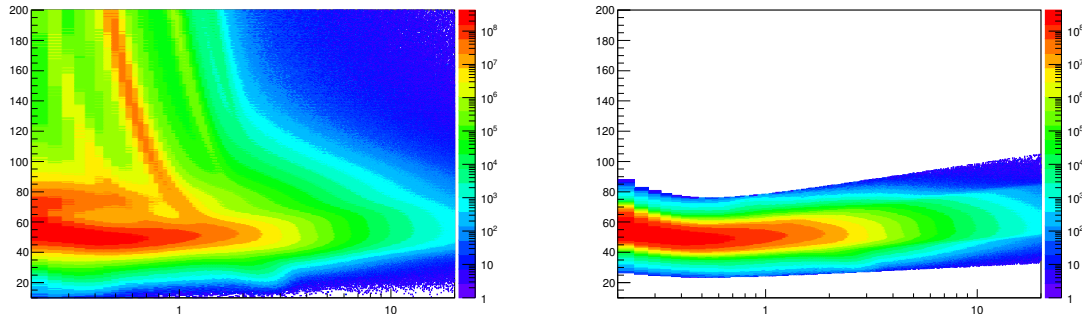


Figure 30: TPC  $dE/dx$  as function of transverse momentum for total (top) and selected first emitted  $\pi$  in  $3\sigma$  (bottom)

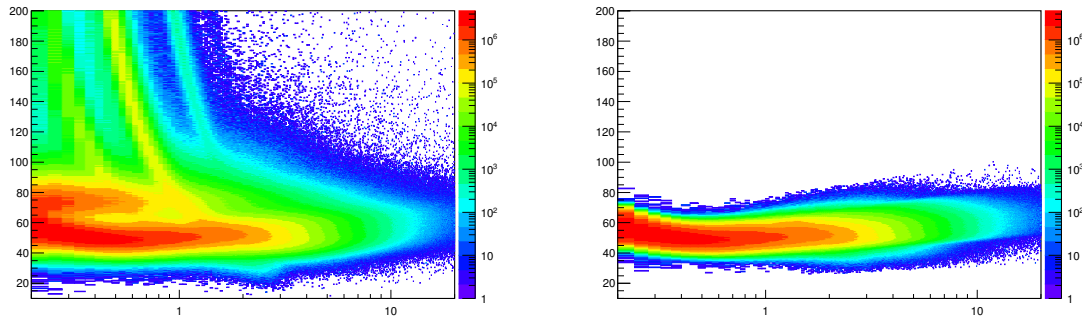


Figure 31: TPC  $dE/dx$  as function of transverse momentum for total (top) and selected second emitted  $\pi$  in  $3\sigma$ (bottom)

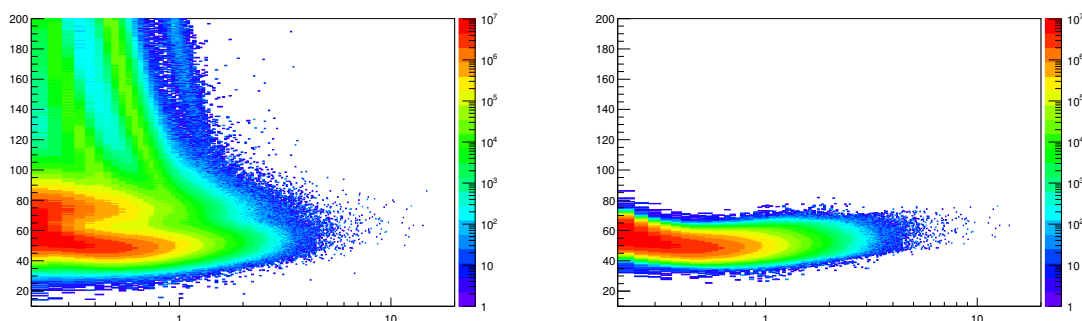


Figure 32: TPC  $dE/dx$  as function of transverse momentum for total (top) and selected last emitted  $\pi$  in  $3\sigma$ (bottom)

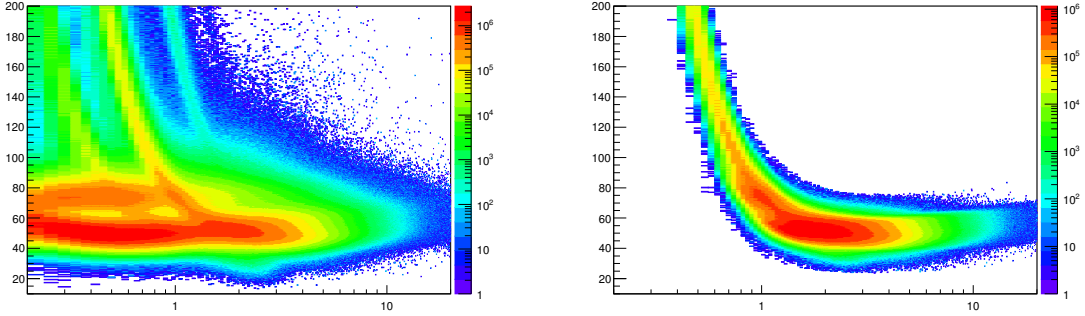


Figure 33: TPC  $dE/dx$  as function of transverse momentum for total (top) and selected proton in  $3\sigma$ (bottom)

#### 1089 5.1.4 Signal extraction

1090 The  $\Xi^{*0}$  signals were reconstructed by invariant-mass analysis of candidates for the decay  
 1091 products in each transverse momentum interval of the resonance particle, and for each  
 1092 multiplicity class. The  $\Xi^-\pi^+(\Xi^+\pi^-)$  invariant mass distribution is reported in Figure 5.1.4  
 1093 for semi-central events (20-40%) in p–Pb collisions and Figure 5.1.4 for central events(0-  
 1094 10%) in Pb–Pb collisions.

1095 Since the resonance decay products originate from a position which is indistinguishable  
 1096 from the PV, a significant combinatorial background is present. In order to extract  
 1097  $\Xi(1530)^0$  signal it is necessary to remove or, at least reduce, the combinatorial background.  
 1098 For this analysis, this has been done with the event mixing (EM) technique, by combining  
 1099 uncorrelated decay products 20 different events in p–Pb (5 different events in Pb–Pb). The  
 1100 events for the mixing have been selected by applying the similarity criteria to minimise  
 1101 distortions due to different acceptances and to ensure a similar event structure, only tracks  
 1102 from events with similar vertex positions  $z$  ( $|\Delta z| < 1$  cm) and track multiplicities  $n$  ( $|\Delta n| <$   
 1103 10) were taken.

1104 The mixed-event background distributions were normalised to two fixed regions,  
 1105  $1.49 < M_{\Xi\pi} < 1.51 \text{ GeV}/c^2$  and  $1.56 < M_{\Xi\pi} < 1.58 \text{ GeV}/c^2$ , around the  $\Xi^{*0}$  mass  
 1106 peak (Figure 5.1.4 and 5.1.4). These regions were used for all  $p_T$  intervals and multiplicity  
 1107 classes, because the background shape is reasonably well reproduced in these regions and  
 1108 the invariant-mass resolution of the reconstructed peaks appears stable, independently of  
 1109  $p_T$ . The uncertainty on the normalisation was estimated by varying the normalisation  
 1110 regions and is included in the quoted systematic uncertainty for the signal extraction (Section 5.4).

1112 After the background subtraction, the resulting distribution is shown in Figure 5.1.4  
 1113 and 5.1.4. In order to obtain raw yields, a combined fit of a first-order polynomial for

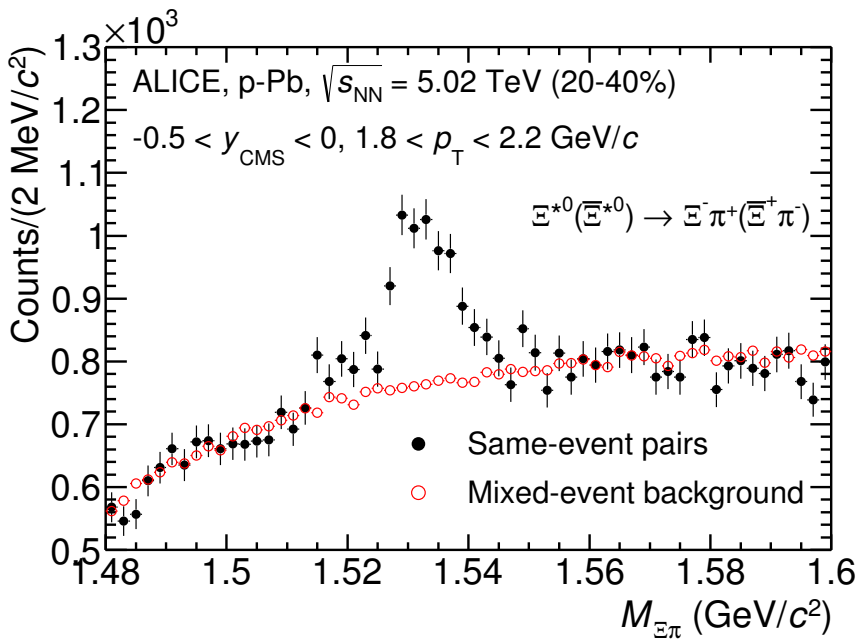


Figure 34: The  $\Xi^\pm\pi^\pm$  invariant mass distribution (Same-event pairs) in  $1.8 < p_T < 2.2 \text{ GeV}/c$  and for the multiplicity class 20-40%. The background shape, using pairs from different events (Mixed-event background), is normalised to the counts in  $1.49 < M_{\Xi\pi} < 1.51 \text{ GeV}/c^2$  and  $1.56 < M_{\Xi\pi} < 1.58 \text{ GeV}/c^2$ .

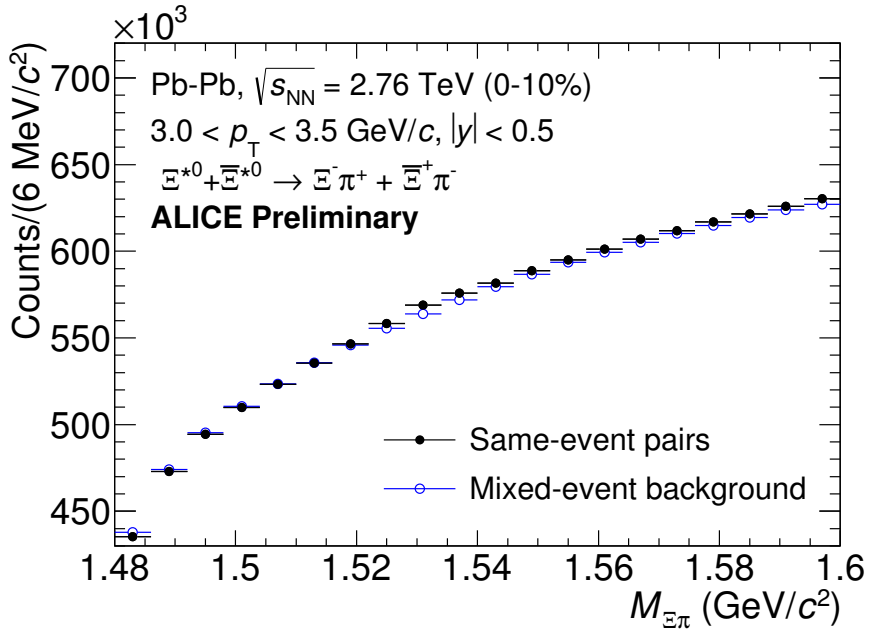


Figure 35: The  $\Xi^\pm \pi^\pm$  invariant mass distribution (Same-event pairs) in  $3.0 < p_T < 3.5 \text{ GeV}/c$  and for the centrality class 0-10%. The background shape, using pairs from different events (Mixed-event background), is normalised to the counts in  $1.49 < M_{\Xi\pi} < 1.51 \text{ GeV}/c^2$  and  $1.56 < M_{\Xi\pi} < 1.58 \text{ GeV}/c^2$ .

the residual background and a Voigtian function (a convolution of a Breit-Wigner and a Gaussian function accounting for the detector resolution) for the signal was used. The mathematical form of fit function used in analysis is:

$$f(M_{\Xi\pi}) = \frac{Y}{2\pi} \frac{\Gamma_0}{(M_{\Xi\pi} - M_0)^2 + \frac{\Gamma_0^2}{4}} \frac{e^{-(M_{\Xi\pi} - M_0)/2\sigma^2}}{\sigma\sqrt{2\pi}} + bg(M_{\Xi\pi}) \quad (7)$$

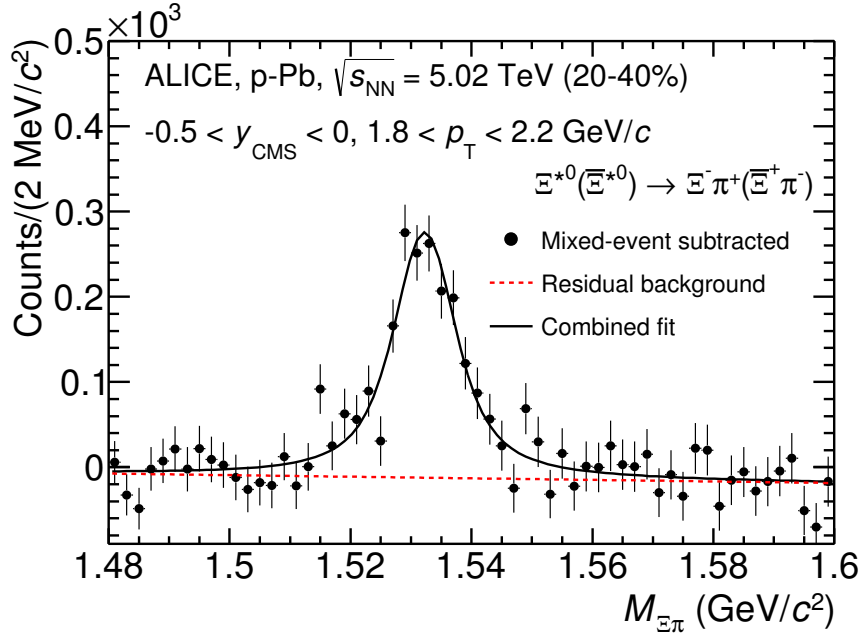


Figure 36: The invariant mass distribution after subtraction of the mixed-event background in p–Pb collisions. The solid curve represents the combined fit, while the dashed line describes the residual background.

The mass parameter of the Voigtian fit ( $M_0$ ) is left free within the fit range ( $1.48 \text{ GeV}/c^2$  and  $1.59 \text{ GeV}/c^2$ ). The overall invariant mass width of the Voigtian function is governed by 2 parameters:  $\sigma$  and  $\Gamma_0$ . The  $\sigma$  describes the broadening of the peak due to finite detector resolution while  $\Gamma$  describes the intrinsic width of the resonance itself. The  $\Gamma_0$  is fixed to the PDG value of  $9.1 \text{ MeV}/c$  for the  $\Xi(1530)^0$ . Because of lack of statistics, the  $\sigma$  can be over estimated. Therefore the  $\sigma$  parameter is fixed to value derived from  $\sigma$  in MB events which has largest statistics. The  $\sigma$  as function of  $p_T$  distribution in MB events is shown in Figure. 38 and we also report invariant mass of  $\Xi(1530)^0$  as function of  $p_T$  in Figure. 39. The  $\Xi(1530)^0$  raw yields have been extracted from the fit for the 4 multiplicity

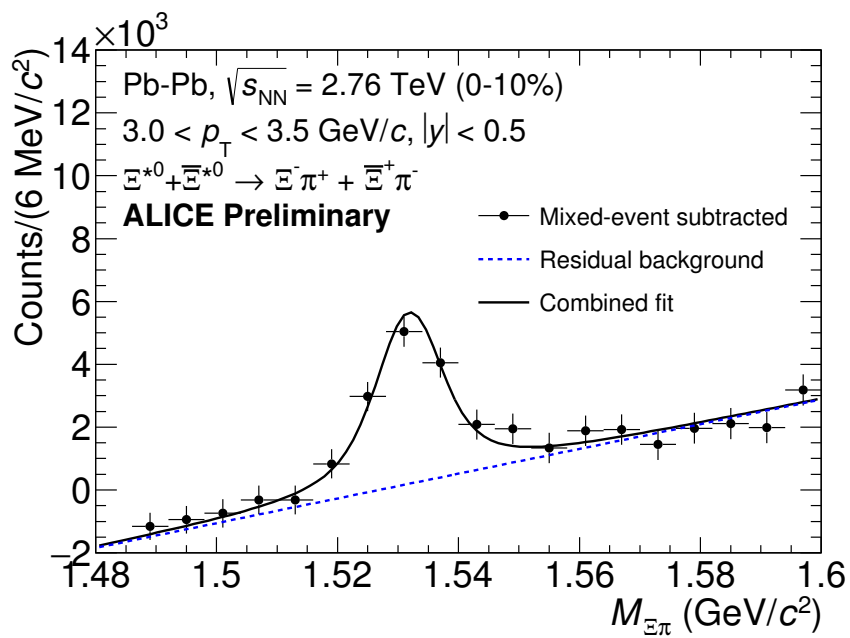


Figure 37: The invariant mass distribution after subtraction of the mixed-event background in Pb–Pb collisions. The solid curve represents the combined fit, while the dashed line describes the residual background.

<sub>1126</sub> bins (+ NSD events) in p–Pb and 4 centrality bins in Pb–Pb collisions and the yields as  
<sub>1127</sub> function of  $p_T$  are shown in Figure 40.

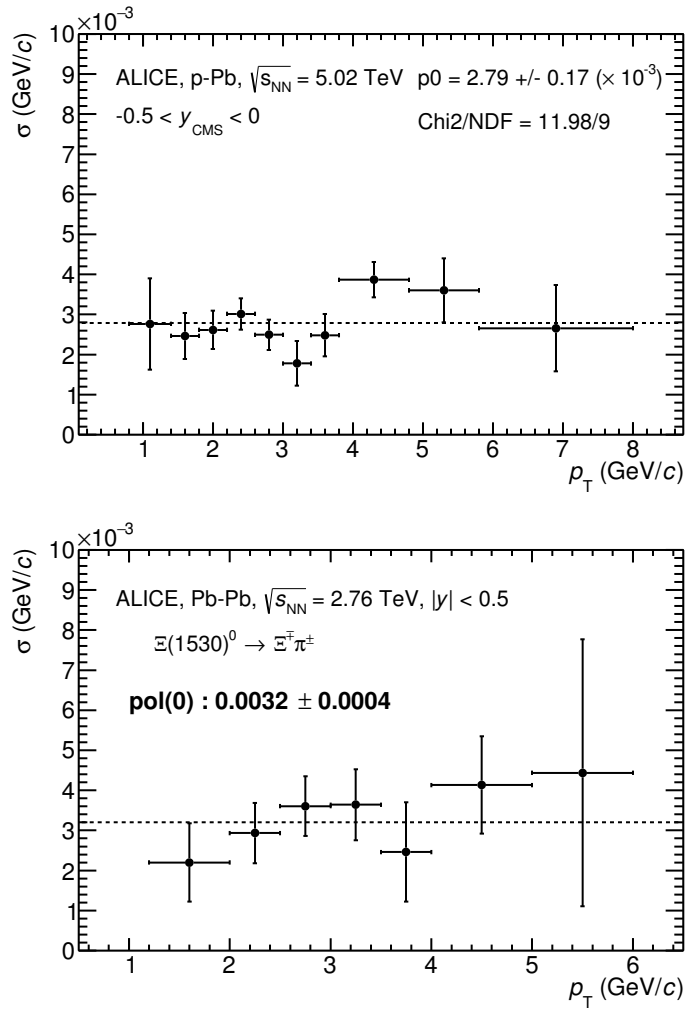


Figure 38:  $\sigma$  fit parameters as a function of  $p_T$  in MB in p–Pb collisions (top) and in Pb–Pb collisions (bottom).

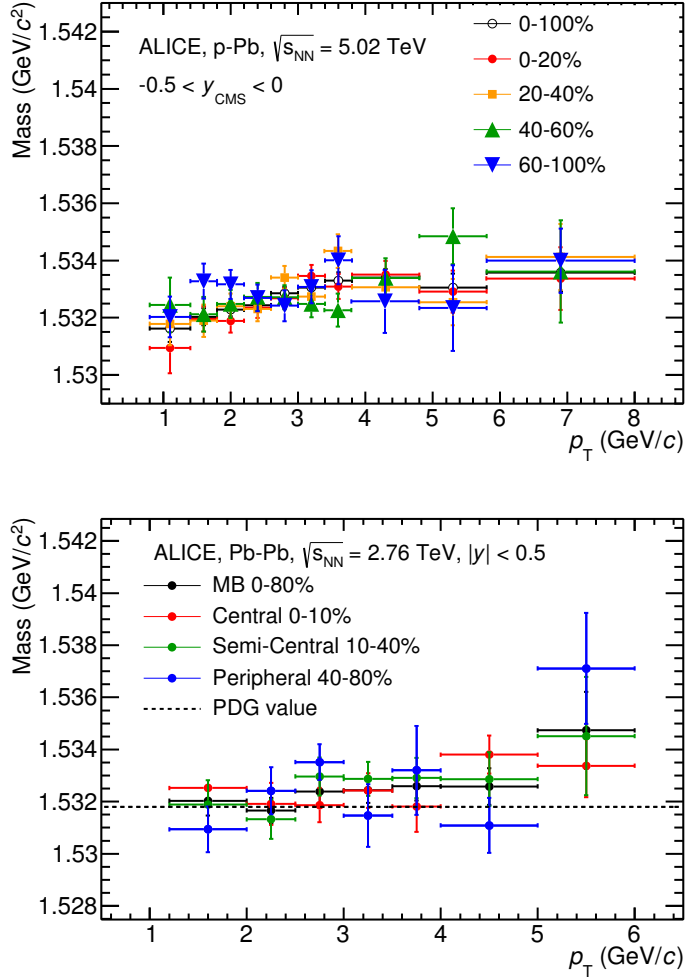


Figure 39:  $\Xi(1530)^0$ -mass obtained from fit of the Voigtian peak as a function of  $p_T$  in each multiplicity classes in p-Pb collisions (top) and the different centrality classes in Pb-Pb (bottom).

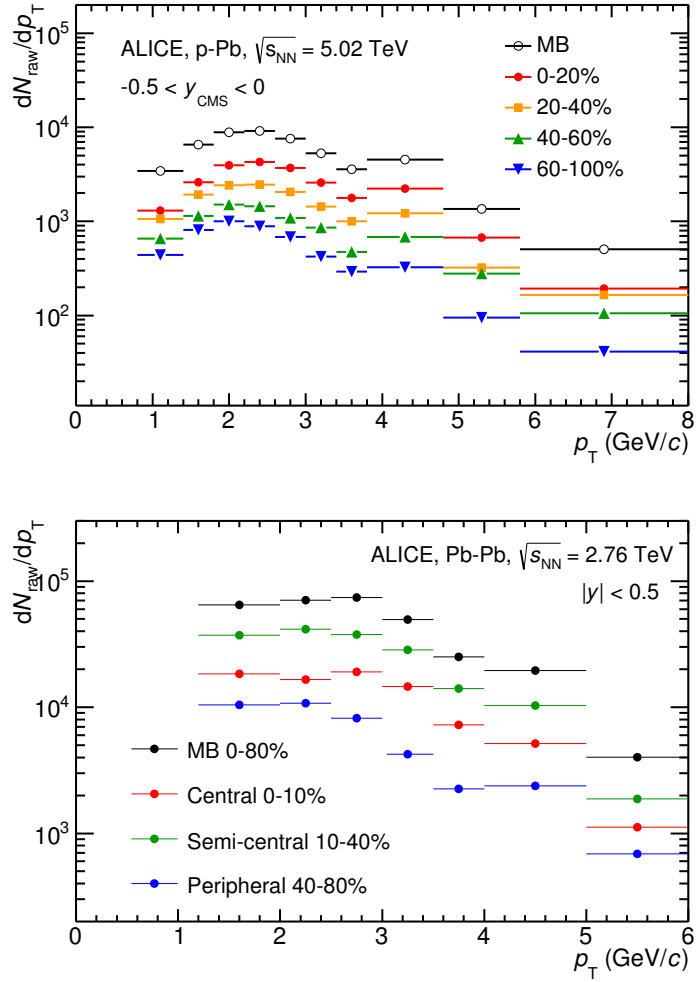


Figure 40:  $\Xi(1530)^0$  -raw spectra obtained from fit of the Voigtian peak and a polynomial residual background for different multiplicities in p-Pb collisions (top) and Pb-Pb collisions (bottom). Only the statistical error is reported.

1128 **5.2 Efficiency correction**

1129 The raw yields were corrected for the geometrical acceptance and the reconstruction effi-  
 1130 ciency ( $A \times \epsilon$ ) of the detector (Figure. 41). By using the DPMJET 3.05 event generator [47]  
 1131 and the GEANT 3.21 package [48], a sample of about 100 million p–Pb events was sim-  
 1132 ulated and reconstructed in order to compute the corrections. The distributions of  $A \times \epsilon$   
 1133 were obtained from the ratio between the number of reconstructed  $\Xi^{*0}$  and the number of  
 1134 generated particle in the same  $p_T$  and rapidity interval. Since the correction factors for  
 1135 different multiplicity classes are in agreement with those from MB events within statistical  
 1136 uncertainty, the latter were used for all multiplicity classes.

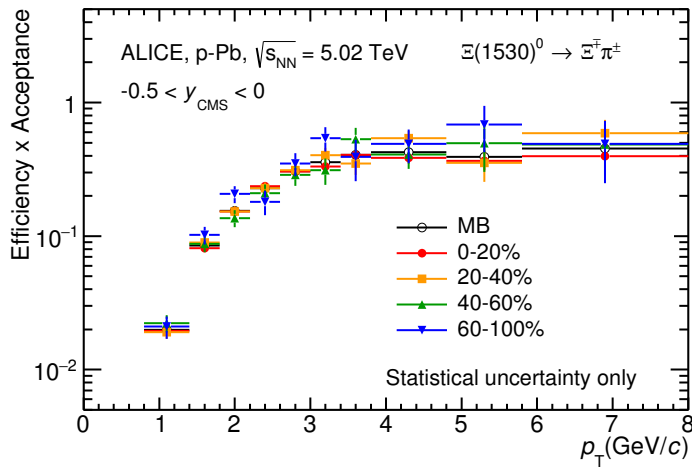


Figure 41:  $\Xi(1530)^0$ -raw spectra obtained from fit of the Voigtian peak and a polynomial residual background for different multiplicities. Only the statistical error is reported.

1137 Because the generated  $\Xi(1530)^0$  spectra have different shapes than the measured  $\Xi(1530)^0$   
 1138 spectra, it is necessary to weight the generated and reconstructed  $\Xi(1530)^0$  spectra in these  
 1139 simulations. Fig. 42 shows the generated and reconstructed  $\Xi(1530)^0$  spectra plotted with  
 1140 the (corrected) measured  $\Xi(1530)^0$  spectrum for MB events and the Levy fit of that mea-  
 1141 sured spectrum. The generated and measured  $\Xi(1530)^0$  spectra have different behaviours  
 1142 for the range  $0.5 < p_T < 1$  GeV/ $c$ . The generated  $\Xi(1530)^0$  spectrum decreases with  
 1143 increasing  $p_T$  over this range, while the fit of the measured  $\Xi(1530)^0$  spectrum reaches a  
 1144 local maximum in this range. The correction  $\epsilon$  is observed to change rapidly over this  
 1145  $p_T$  range. It is therefore necessary to weight the generated spectrum so that it has the  
 1146 shape of the measured  $\Xi(1530)^0$  spectrum (and to apply corresponding weights to the re-  
 1147 constructed  $\Xi(1530)^0$  spectrum). An iterative procedure is performed to determine the  
 1148 correct weighting (and therefore the correct  $\epsilon$ ).

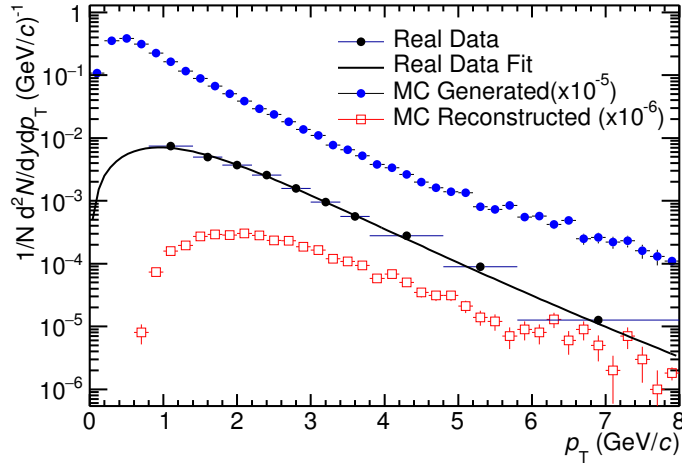


Figure 42: Real corrected  $\Xi(1530)^0$  spectrum (black) for the minimum bias with Levy fit (black curve). Also shown are the unweighted generated (blue) and reconstructed (red)  $\Xi(1530)^0$  spectra.

- 1149 1. The unweighted  $\epsilon$  is calculated.
- 1150 2. This  $\epsilon$  is used to correct the measured xis spectrum.
- 1151 3. The corrected  $\Xi(1530)^0$  spectrum is fit.
- 1152 4. This fit is used to weight the simulated xis spectra. A  $p_T$  dependent weight is applied  
1153 to the generated xis spectrum so that it follows the fit. The same weight is applied  
1154 to the reconstructed xis spectrum.
- 1155 5. The (weighted)  $\epsilon$  is calculated.
- 1156 6. Steps 2-5 are repeated (with the weighted  $\epsilon$  from step 5 used as the input for step 2)  
1157 until the  $\epsilon$  values are observed to change by  $< 0.1\%$  (relative) between iterations. It  
1158 is observed that four iterations are sufficient for this procedure to converge.

1159 Finally, the re-weighted efficiency is obtained and the distribution as function of  $p_T$  is  
1160 shown in Figure 43.

1161 In order to obtain the correction factor dedicated in Pb-Pb collisions, MC events are  
1162 generated using Heavy Ion Jet Interaction Generator (HIJING). The generated events are  
1163 passed through a GEANT3 model of the ALICE experiment with a realistic description of  
1164 the detector response. Because we have observed centrality dependent efficiency, the cen-  
1165 trality dependent efficiencies have been applied to get corrected raw yield. The reweighting

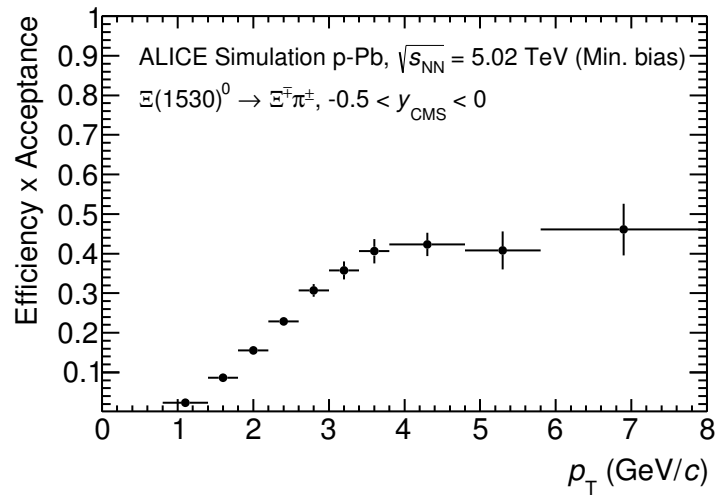


Figure 43: Efficiency as a function of  $p_T$  in minimum bias events in p–Pb collisions.

1166 approach which was used to correct the efficiency in p–Pb is also applied to the efficiency  
 1167 obtained in Pb–Pb.

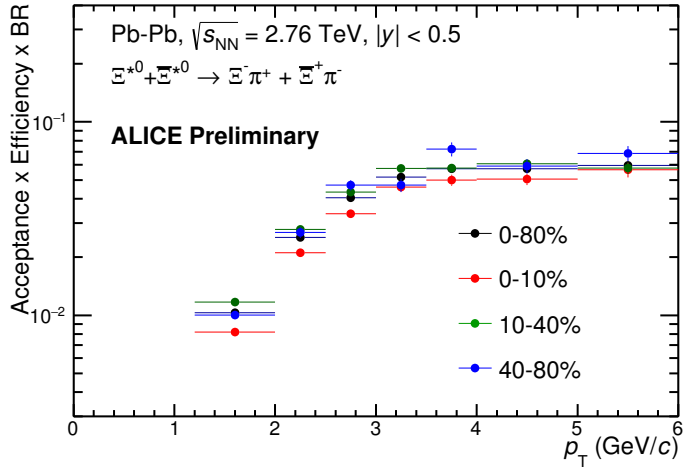


Figure 44: Efficiency as a function of  $p_T$  in different centrality classes in Pb–Pb collisions

### 1168 5.3 Corrected $p_T$ -spectra

1169 The  $p_T$  spectrum is by the number of produced particles of a given type in the desired  
 1170 interval of phase-space divided by the number of inelastic collisions. The spectrum is  
 1171 calculated as:

$$\frac{1}{N} \times \frac{d^2N}{dydp_T} = \frac{1}{N_{E,PhysSel}} \times \frac{N_{raw}}{dp_T dy} \epsilon \frac{N_{total}^{MC}}{N_{post-PVcut}^{MC}}, \quad (8)$$

1172 where  $N_E$  represent the number inelastic collisions, the  $\frac{dN}{dydp_T}$  is the yield per range of  
 1173 rapidity  $y$ , per range in  $p_T$ . On the right hand side  $N_{E,PhysSel}$  is the number of events  
 1174 counted by the physics selection trigger.  $N_{raw}$  is the raw extracted number of particle in the  
 1175 rapidity and  $p_T$  bin of width  $\Delta y = 0.5$  in p–Pb ( $\Delta y = 1.0$  in Pb–Pb) and  $\Delta p_T$ , respectively.  
 1176  $\epsilon$  is the reconstruction efficiency estimated from Monte Carlo simulations.  $\frac{N_{total}^{MC}}{N_{post-PVcut}^{MC}}$  is the  
 1177 ratio of the total number of particle from MC divided by the number of particle from MC  
 1178 after the Primary-Vertex cut is imposed. It takes into account the fraction of particle lost  
 1179 after imposing the PV cut. We notice that for minimum-bias results in p–Pb, we adopted  
 1180 a normalisation such that to provide result from non-single diffractive(NSD) cross-section.  
 1181 The normalisation factor is 0.964 [6]. The obtained spectrum at MB and the spectrums  
 1182 from different multiplicity classes in p–Pb are shown in Figure 45 and different centrality  
 1183 classes in Pb–Pb are shown in Figure 46.

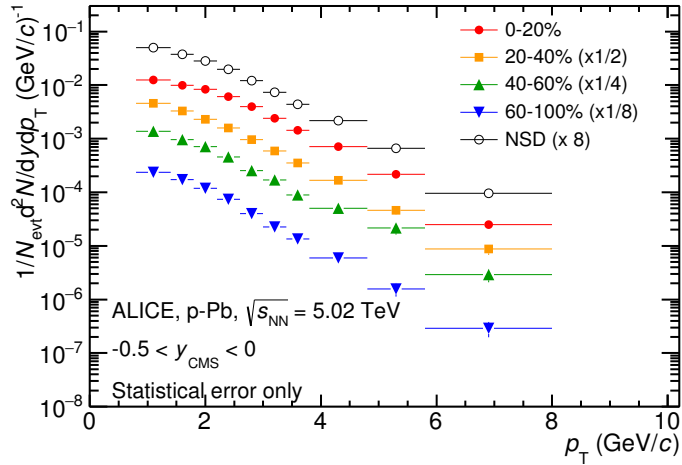


Figure 45: Corrected  $p_T$ -spectra of  $\Xi(1530)^0$  in NSD and different multiplicity classes in p-Pb collisions.

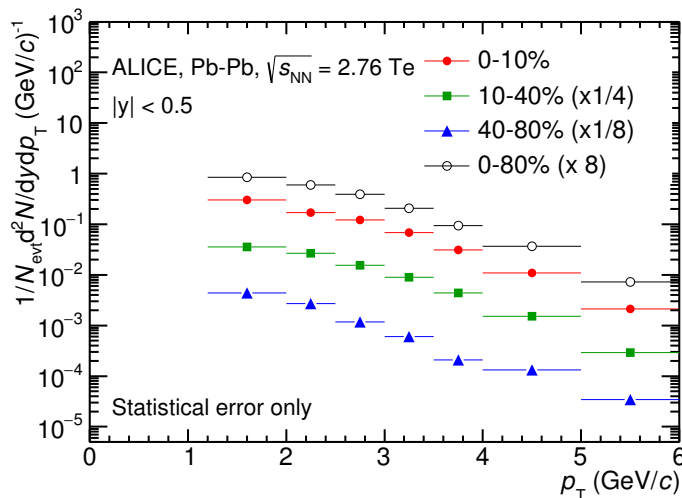


Figure 46: Corrected  $p_T$ -spectra of  $\Xi(1530)^0$  in different centrality classes in Pb-Pb collisions.

1184 **5.4 Systematic uncertainties**

1185 The systematic uncertainties are calculated in seven principle groups. The procedure to ob-  
1186 tain the systematic uncertainties is performed many times by varying the possible permuta-  
1187 tion of the analysis parameter. The general strategy for evaluating systematic uncertainties  
1188 is described as following:

- 1189 1. Choose one set of parameters for the analysis as default  
1190 2. Observe the deviation of yield when one parameter is changed  
1191 3. The systematic uncertainty is calculated for a given source as the RMS deviation of  
1192 the available sources.  
1193 4. The total systematic uncertainty, taking into account all the different sources, is the  
1194 sum in quadrature of each source.

1195 To study the systematic effect we repeat the measurement by varying one parameter at  
1196 a time. A Barlow [49] check has been performed for each measurement to verify whether it  
1197 is due to a systematic effect or a statistical fluctuation. Let each measurement be indicated  
1198 by  $(y_i \pm \sigma_i)$  and the central value (default measurement) by  $(y_c \pm \sigma_c)$ , one can define  $\Delta\sigma_i$   
1199 (Eq. 9).

$$\Delta\sigma_i = \sqrt{(|\sigma_i^2 - \sigma_c^2|)} \quad (9)$$

1200 Then we calculate  $n_i = \Delta y_i / \Delta\sigma_i$ , where  $\Delta y_i = |y_c - y_i|$ . If  $n_i \leq 1.0$  then the effects  
1201 are due to the statistical fluctuation and if  $n_i > 1.0$  we apply consistency check. Since  
1202 the alternate and default measurements are not statistically independent, an alternate  
1203 measurement which is statistically consistent with the default measurement should not be  
1204 used in calculating a systematic uncertainty. The difference between the two measurements  
1205 is  $\Delta = y_c - y_i$ . The difference in quadrature of the uncertainties is calculated by Eq. 9. It  
1206 could be possible to check if  $\Delta < \sigma$  and exclude such cases from the systematic uncertainties.  
1207 However, there can be statistical fluctuations for which  $\Delta > \sigma$ . If the variations between the  
1208 default and alternate measurements are purely statistical, the distribution of  $\Delta/\sigma$  should  
1209 be a Gaussian with a mean value that is consistent with zero and a deviation  $\sigma$  consistent  
1210 with unity. In this analysis, if the mean value is less than 0.1 and  $\sigma$  is less than 1, the  
1211 variation passes the consistency check.

1212 Only the measurements which passed the Barlow check ( $n_i > 1$ ) are used to determine  
1213 the systematic uncertainty. For measurements  $N > 2$ , the systematic uncertainty has been  
1214 determined as the RMS (eqn. 10) of the available measurements. If  $N=2$ , the absolute  
1215 difference is assigned as systematic uncertainty.

$$\delta y_{syst.} = \sqrt{\frac{1}{N} \sum_i (y_i - \bar{y})^2} \quad (10)$$

1216 Here  $N$  is the total number of available measurements including  $y_c$  and  $\bar{y}$  is the average  
1217 of value of the measurements. The measurement did not pass Barlow check, zero systematic  
1218 uncertainty has been assigned to the value.

1219 By suing the way as explained above, all the main contributions to the systematic un-  
1220 certainty of particle spectra have been studied. In particular those that comes from signal  
1221 extraction, topological and kinematical selection cuts, track quality selection and  $n\sigma$  TPC  
1222 PID variation. the meaning of each source of systematic uncertainty studied is described  
1223 in the following:

1224

### 1225     **Signal extraction**

1226 We have extracted the signal with varying the yield calculating method which contains  
1227 the method of signal extraction by integrating the Voigtian fit function and bin counting.  
1228 We also have varied the normalisation range which is related to the invariant mass region  
1229 where the mixed events distribution is scaled to subtract the combinatorial background  
1230 and different background estimator such as Like-Sign distribution and polynomial fit was  
1231 taken account into the systematic source of signal extraction. The systematic uncertainty  
1232 from signal extraction is sum in quadrature of three sources.

1233

### 1234     **Topological selection**

1235 To evaluate the stability of the chosen set of values for the topological cuts, loose and tight  
1236 cuts have beed defined in order to vary by  $\pm 10\%$  respectively. The parameters are changed  
1237 once at a time. Total systematic uncertainty from topological selection is calculated by  
1238 summation in quadrature of nine sources.

1239

### 1240     **TPC $N_{cluster}$ selection**

1241 The selection performed for the daughter tracks of the cascade is that  $N_{cluster}$  is larger  
1242 than 70 and the value has been varied to 60 and 80 in order to estimate the systematic  
1243 uncertainty due to this selection.

1244

### 1245     **TPC $dE/dx$ selection**

1246 In order to evaluate any potential effect due to the TPC  $dE/dx$  selection ( $U_{PID}$ ), the  $N_\sigma$   
1247 selection was varied with  $N = 2.5$  and  $3.5$ .

1248

### 1249      **$p_T$ shape correction**

1250 As described in Section 5.2, due to the different shape of the measured and generated  
1251  $\Xi(1530)^0$  spectra, we have applied reweighing procedure to the generated spectra to have  
1252 same shape and this correction is added into contributor of systematic uncertainty as  
1253  $p_T$  shape correction.

1254

### 1255     **Mass window range selection**

1256 In order to select  $\Xi^\pm$  which is daughter particle of  $\Xi(1530)^0$ , we apply the mass window

1257  $\pm 7$  MeV/ $c^2$  around  $\Xi(1530)^0$  mass on  $\Lambda\pi$  invariant mass distribution. The boundaries has  
1258 been varied to  $\pm 6$  MeV/ $c^2$  and  $\pm 8$  MeV/ $c^2$  to estimate systematic uncertainty.

1259

### 1260     **Vertex range selection**

1261 The distribution of vertex-z is shown in Fig.22. The cut on  $|Vz|$  was varied from the nominal  
1262  $\pm 10$ cm to  $\pm 9$ cm,  $\pm 11$ cm.

1263

### 1264     **Material Budget and hadronic cross section**

1265 A possible source of uncertainty comes from the description of the material, active (detecting area)  
1266 or dead (structure and cable), that the particles cross during their travel in  
1267 the MC with respect to the real material present in the detector. Such description could  
1268 affect the reconstruction efficiency in different aspects (e.g. multiple scattering, energy  
1269 loss). The value estimated by  $\Xi$  analysis [24] has been used in this study which gives 4%  
1270 systematic uncertainty. In case of systematic uncertainty from hadronic cross section, we  
1271 have inherited the value studied in previous measurement[50] which amount is 1%.

1272

### 1273     **Tracking efficiency**

1274 Systematic uncertainties from tracking efficiency from ITS + TPC combined track were  
1275 assigned as 3% in p–Pb and 4% in Pb–Pb collision system.[50]  
1276 (<https://twiki.cern.ch/twiki/bin/view/ALICE/TrackingEfficiencyCharged>)

1277

1278 Finally, total systematic uncertainty is sum in quadrature of sources listed above. Figure  
1279 47 and Figure 48 show the total systematic uncertainty in minimum bias event and  
1280 different multiplicity classes in p–Pb collisions, respectively. Again, Figure 49 and Figure  
1281 50 present the total systematic uncertainty in minimum bias event and different centrality  
1282 classes in Pb–Pb collisions.

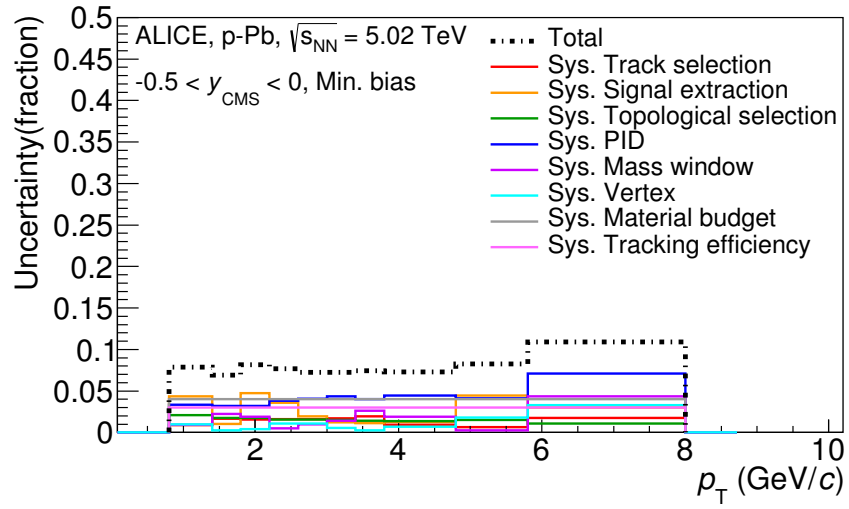


Figure 47: Summary of the contributions to the systematic uncertainty in minimum bias events in p–Pb collisions. The dashed black line is the sum in quadrature of all the contributions.

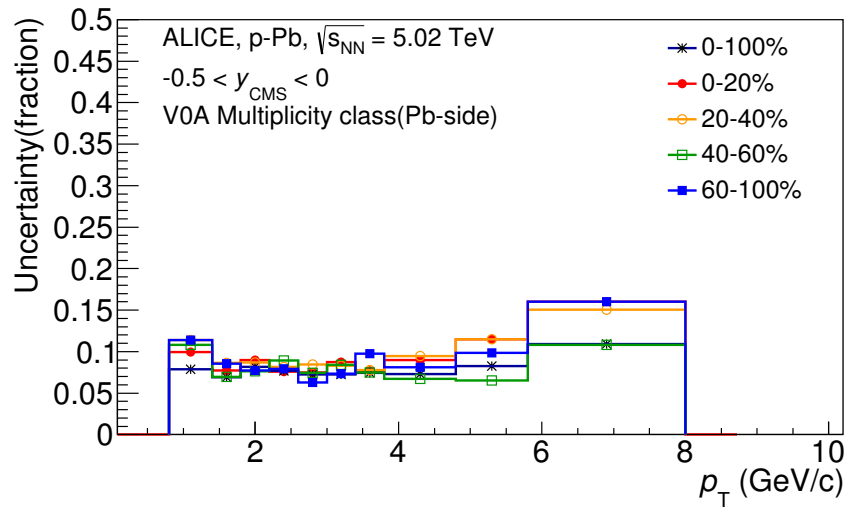


Figure 48: Systematic uncertainties for each multiplicity classes in p–Pb collisions.

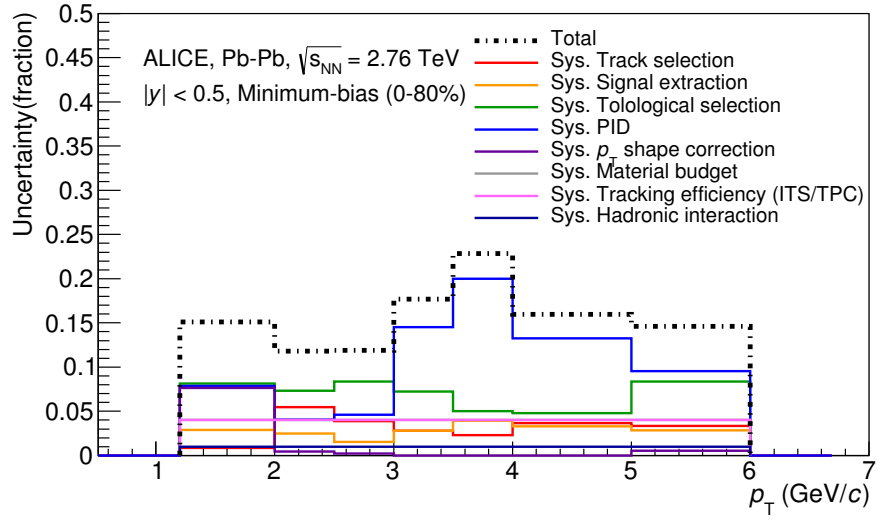


Figure 49: Summary of the contributions to the systematic uncertainty in minimum bias events in Pb–Pb collisions. The dashed black line is the sum in quadrature of all the contributions.

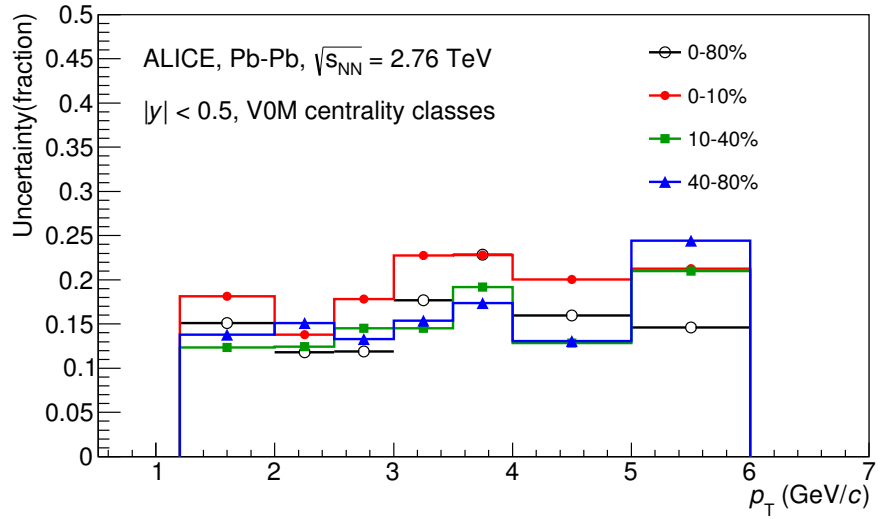


Figure 50: Systematic uncertainties for each multiplicity classes.

Source of uncertainty	p-Pb	Pb-Pb
<i>p</i> <sub>T</sub> -dependent		
Tracking efficiency	3%	4%
Tracks selection	1-2%	1-5%
Topological selection	1-2%	5-8%
PID	3-7%	4-20%
Signal extraction	1-5%	1-4%
<i>p</i> <sub>T</sub> shape correction	-	0-8%
Mass window ( $\Xi^\pm$ )	4%	-
Vertex selection	3%	-
<i>p</i> <sub>T</sub> -independent		
Hadronic interaction	-	1%
Material budget	4%	4%
Branching ratio	0.3%	0.3%
Total	8-12%	9-25 %

Table 11: Summary of the systematic uncertainties on the differential yield,  $d^2N/(dp_T dy)$ . Minimum and maximum values in all  $p_T$  intervals and multiplicity classes in p–Pb, centrality classes in Pb–Pb are shown for each source.

1283 **5.5  $\Xi(1530)^0$  transverse momentum spectra**

1284 The raw yield shown in Figure 45 and 46 have been corrected for efficiency as described  
 1285 in section 5.2. The measured spectra for  $(\Xi(1530)^0 + \bar{\Xi}(1530)^0)/2$  are reported in Figure  
 1286 51 for p–Pb collisions and Figure 52 for Pb–Pb collisions. The statistical and systematic  
 1287 uncertainties are reported respectively as the error bars and the boxes on the plot. The  
 1288 corrected yields for p–Pb collisions are measured with  $0.8 < p_T < 8.0$  GeV/c while the  
 1289 yields for Pb–Pb collisions are obtained with  $1.2 < p_T < 6.0$  GeV/c due to difficulty of  
 1290 signal extraction in low and high  $p_T$  region.

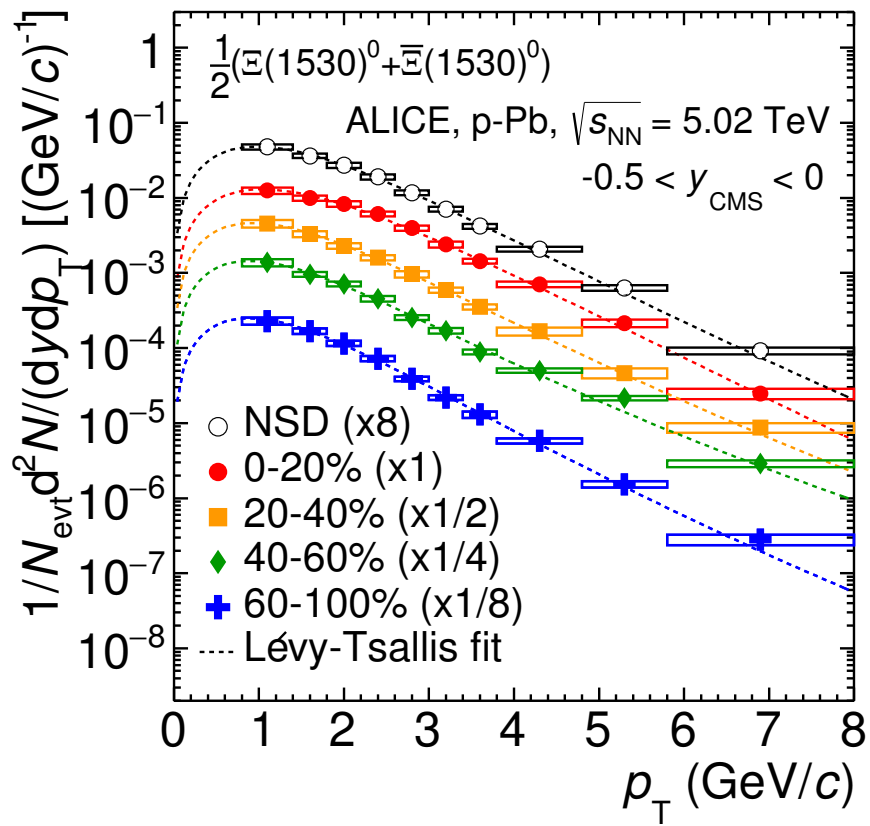


Figure 51: Corrected yields as function of  $p_T$  in NSD events and multiplicity dependent event classes in p-Pb collision system. Statistical uncertainties are presented as bar and systematical uncertainties are plotted as boxes.

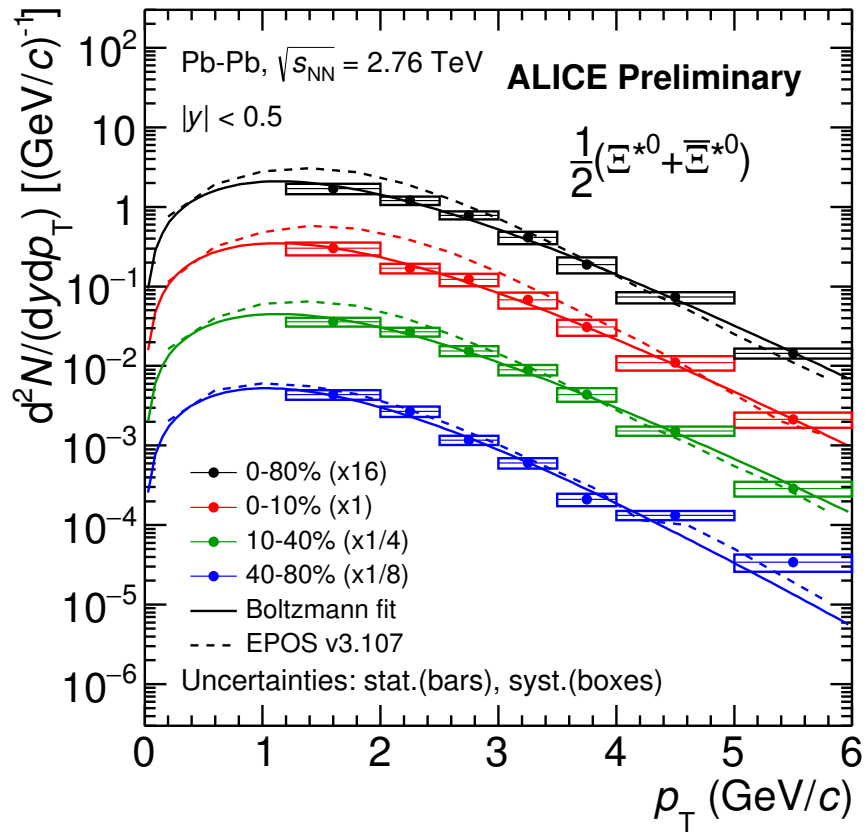


Figure 52: Corrected yields as function of  $p_T$  in different centrality classes in  $\text{Pb-Pb}$  collision system. Statistical uncertainties are presented as bar and systematical uncertainties are plotted as boxes.

## 1291 6 Further results and discussion

1292 The transverse momentum distributions of double-strange hyperon resonances,  $\Xi(1530)^0$   
1293 , produced in p–Pb collisions at  $\sqrt{s_{\text{NN}}}= 5.02$  TeV and Pb–Pb collisions at  $\sqrt{s_{\text{NN}}}= 2.76$   
1294 TeV were measured in the mid-rapidity range and they have been already presented in  
1295 Chapter 5. From the measurement, the  $\langle p_{\text{T}} \rangle$  and integrated particle yield ratios with  
1296 system size have been obtained. In the present Chapter these results are compared with  
1297 model predictions and discussed in connection with the following topics:

- 1298 • Mean transverse momentum studies
- 1299 • Study of particle production mechanism in hadronic phase
- 1300 • Study of strangeness enhancement

1301 Most of the theoretical aspects related to these topics and, in particular, the description  
1302 of the models already have been addressed in Chapter 2.

### 1303 6.1 Mean transverse momentum

1304 Figure 53 shows the mean transverse momentum  $\langle p_{\text{T}} \rangle$  as a function of mean charged-  
1305 particle multiplicity density  $\langle dN_{\text{ch}}/d\eta_{\text{lab}} \rangle$  at midrapidity. The results for  $\Xi(1530)^0$  are  
1306 compared with those for other hyperons observed in p–Pb collisions at  $\sqrt{s_{\text{NN}}}= 5.02$  TeV [5,  
1307 7].

1308 Increasing trends from low to high multiplicities are observed for all hyperons. The  
1309 mean transverse momenta increase by 20% as the mean charged-particle multiplicity in-  
1310 creases from 7.1 to 35.6. This result is similar to the one obtained for the other hyperons.  
1311 Furthermore, a similar increase has been observed also for  $K^{\pm}$ ,  $K_S^0$ ,  $K^*(892)^0$  and  $\phi$  [6],  
1312 whereas protons are subject to a larger ( $\sim 33\%$ ) increase in the given multiplicity range,  
1313 as discussed also in Ref. [5].

1314 In all multiplicity classes, the  $\langle p_{\text{T}} \rangle$  follows an approximate mass ordering:

- 1315 •  $\langle p_{\text{T}} \rangle_{\Lambda} < \langle p_{\text{T}} \rangle_{\Xi^-} \simeq \langle p_{\text{T}} \rangle_{\Sigma^{*\pm}} < \langle p_{\text{T}} \rangle_{\Xi^{*0}} < \langle p_{\text{T}} \rangle_{\Omega^-}$

1316 The  $\langle p_{\text{T}} \rangle$  of  $\Sigma^{*\pm}$  looks systematically lower than the  $\langle p_{\text{T}} \rangle$  of  $\Xi^-$ , despite the larger mass  
1317 of  $\Sigma^{*\pm}$ . The uncertainties, however, are too large to draw any conclusion on possible hints  
1318 of violation of the mass hierarchy. This hierarchy of mass-ordering, also including  $D^0$  and  
1319  $J/\psi$  in the comparison, is displayed in Figure 54. Note, however, that the  $D^0$  and  $J/\psi$   
1320 were measured in different rapidity ranges:  $|y_{\text{CMS}}| < 0.5$  [9] ( $|y_{\text{CMS}}| < 0.9$  [10]) for  $D^0$   
1321 ( $J/\psi$ ) in pp and  $-0.96 < y_{\text{CMS}} < 0.04$  [9] ( $-1.37 < y_{\text{CMS}} < 0.43$  [11]) for  $D^0$  ( $J/\psi$ ) in  
1322 p–Pb, and the results for  $D^0$  and  $J/\psi$  in p–Pb collisions are for the 0–100% multiplicity  
1323 class. This mass dependence is observed in both p–Pb and pp collisions. It was observed  
1324 also by the STAR collaboration [51] in MB pp, MB d–Au and central Au–Au collisions.

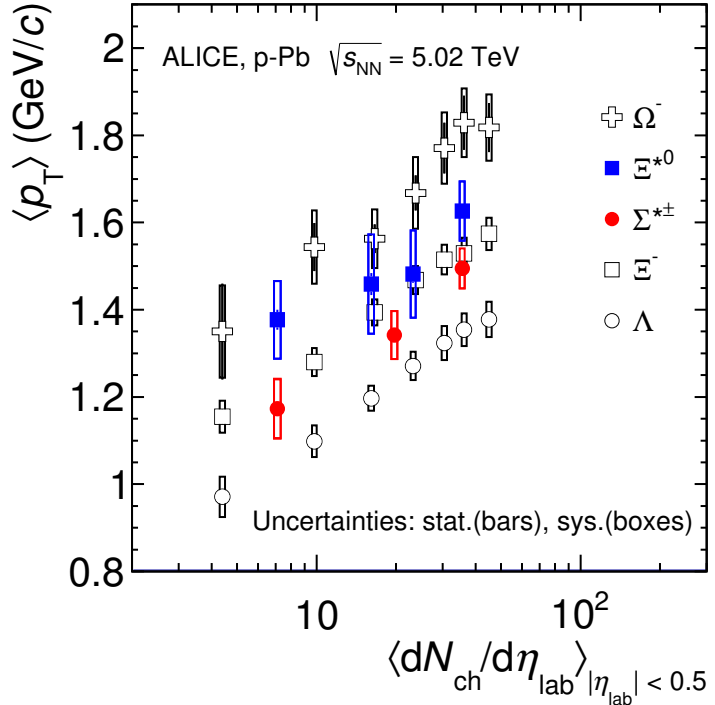


Figure 53: Mean transverse momenta  $\langle p_T \rangle$  of  $\Lambda$ ,  $\Xi^-$ ,  $\Sigma^{*\pm}$ ,  $\Xi^{*0}$  and  $\Omega^-$  in p–Pb collisions at  $\sqrt{s_{NN}}=5.02$  TeV as a function of mean charged-particle multiplicity density  $\langle dN_{ch}/d\eta_{lab} \rangle$ , measured in the pseudorapidity range  $|\eta_{lab}| < 0.5$ . The results for  $\Lambda$ ,  $\Xi^-$  and  $\Omega^-$  are taken from [5, 6, 7]. Statistical and systematic uncertainties are represented as bars and boxes, respectively. The  $\Omega^-$  and  $\Xi^-$  points in the 3rd and 4th lowest multiplicity bins are slightly displaced along the abscissa to avoid superposition with the  $\Xi(1530)^0$  points.

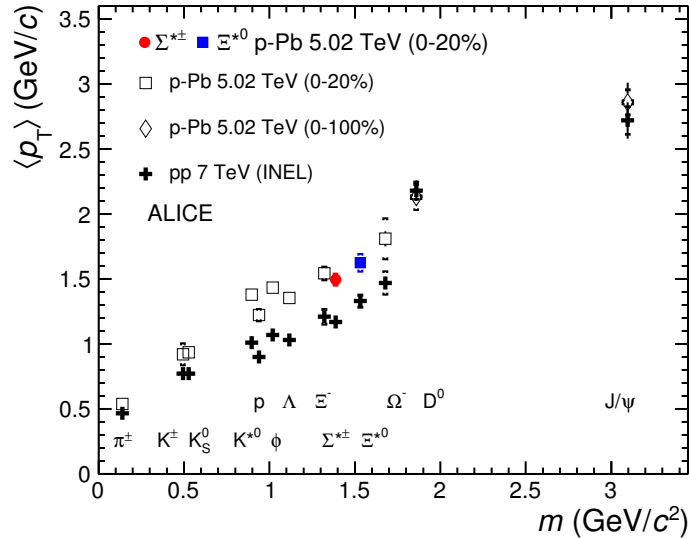


Figure 54: Mass dependence of the mean transverse momenta of identified particles for the 0 – 20% V0A multiplicity class and with  $-0.5 < |y_{\text{CMS}}| < 0$  in p–Pb collisions at  $\sqrt{s_{\text{NN}}} = 5.02$  TeV [5, 7], and in minimum-bias pp collisions at  $\sqrt{s} = 7$  TeV [8] with  $|y_{\text{CMS}}| < 0.5$ . Additionally,  $D^0$  and  $J/\psi$  results are plotted. The  $D^0$  and  $J/\psi$  were measured in different rapidity ranges:  $|y_{\text{CMS}}| < 0.5$  [9] ( $|y_{\text{CMS}}| < 0.9$  [10]) for  $D^0$  ( $J/\psi$ ) in pp and  $-0.96 < y_{\text{CMS}} < 0.04$  [9] ( $-1.37 < y_{\text{CMS}} < 0.43$  [11]) for  $D^0$  ( $J/\psi$ ) in p–Pb. Note also that the results for  $D^0$  and  $J/\psi$  in p–Pb collisions are for the 0–100% multiplicity class.

1325 Furthermore, for the light-flavour hadrons, the mean transverse momenta in p–Pb col-  
1326 lisions are observed to be consistently higher than those in pp collisions at 7 TeV. The  
1327 situation for the charm hadrons is different, where  $\langle p_T \rangle$  appears compatible between both  
1328 colliding systems. The discrepancy is likely due to different production mechanisms for  
1329 heavy and light flavours and to a harder fragmentation of charm quarks. Specifically, the  
1330 fact that  $\langle p_T \rangle$  remains similar in pp and in p–Pb is consistent with an  $R_{p\text{Pb}}$  ratio com-  
1331 patible with unity at all  $p_T$ [9] for  $D^0$ , and/or with the effects of shadowing in p–Pb which  
1332 reduces the production at low  $p_T$  and thus increasing the overall  $\langle p_T \rangle$  for  $J/\psi$  [11]; the  
1333 small  $p_T$ hardening expected in pp when going from 5.02 to 7TeV is apparently not enough  
1334 to counter-balance the situation.

1335 Because of small decrease of the  $\langle p_T \rangle$  for proton and  $\Lambda$  relative to those for  $K^{*0}$  and  
1336  $\phi$ , two different trends for mesons and baryons have been suggested [52]. Even including  
1337  $D^0$  and  $J/\psi$ , as shown in Figure 54, a different trend for mesons and baryons cannot be  
1338 convincingly established.

1339 **6.2 Particle yield ratios**

1340 **6.2.1 Integrated yield ratios of excited to ground-state hadrons**

1341 The integrated yield ratios of excited to ground-state hyperons [53, 5, 8, 7] with the same  
1342 strangeness content, for different collision systems and energies, are shown in Figure 55  
1343 as a function of system size. The ratio of  $\Xi(1530)^0$  to  $\Xi$  is flat across the system and  
1344 it complements the information derived from other resonance measurement for different  
1345 lifetime which are shown in Figure 56.

1346 The short-lived resonances( $\rho$ ,  $K^*$  and  $\Lambda^*$ ) which exhibit suppression from peripheral to  
1347 central lead-lead collisions and with respect to thermal model in central lead-lead collisions.  
1348 Currently favored explanation of is dominance of elastic re-scattering of decay daughters  
1349 over regeneration in the hadronic phase.

1350 The constant behavior of the yield ratios of excited to ground-state hyperons with same  
1351 strangeness content ( $\Xi(1530)^0$  and  $\Phi$ ) indicates that neither regeneration nor re-scattering  
1352 dominates with increasing collision system size because of its longer-lifetime.

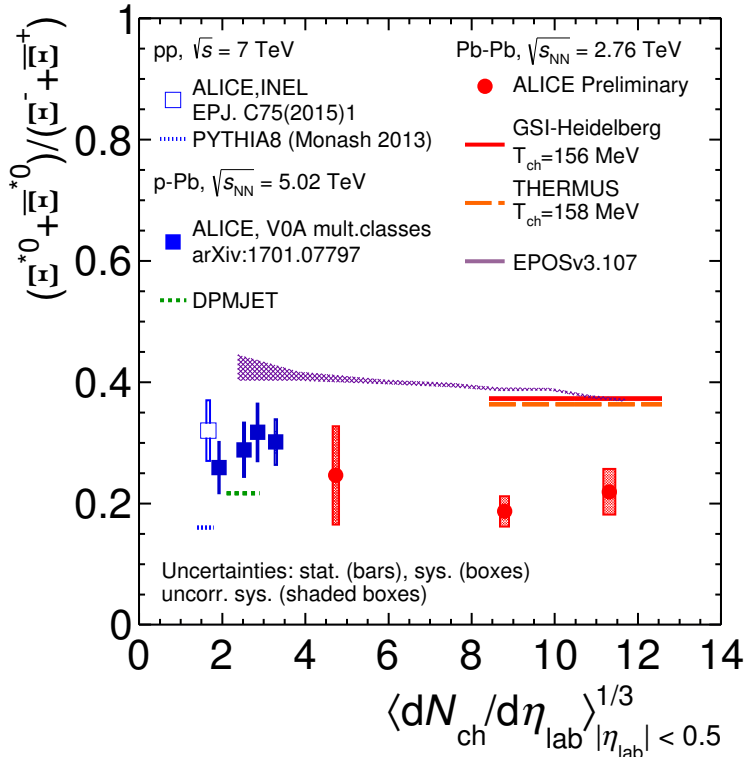


Figure 55: Ratio of  $\Xi(1530)^0$  to  $\Xi^-$  measured in pp [8], p–Pb [5, 7] and Pb–Pb collisions as a function of  $\langle dN_{ch}/d\eta_{lab} \rangle$  measured at midrapidity. Statistical uncertainties (bars) are shown as well as total systematic uncertainties (hollow boxes) and systematic uncertainties uncorrelated across multiplicity (shaded boxes). A few model predictions are also shown as lines at their appropriate abscissa.

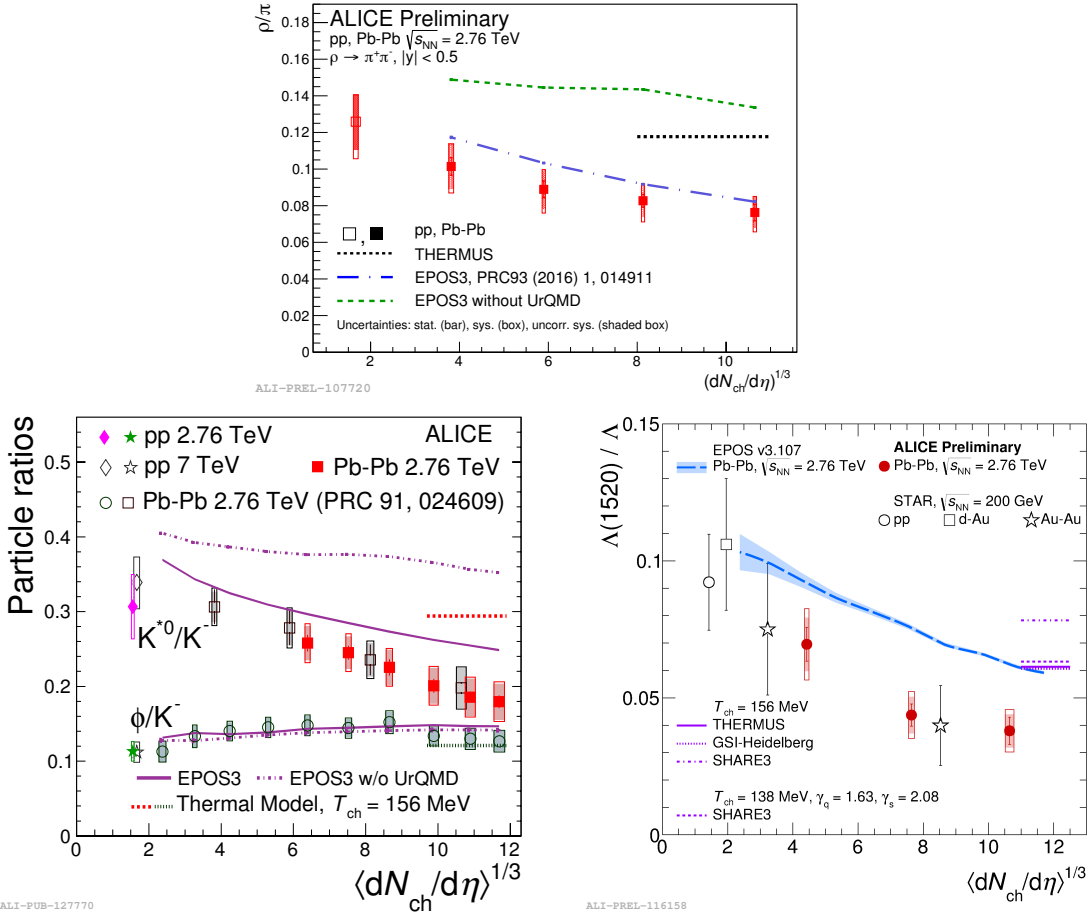


Figure 56: Ratio of  $\rho/\pi$ (Up),  $K^*/K$ ,  $\phi/K$ (Left bottom) and  $\Lambda^*/\Lambda$  with system size measured at mid-rapidity. Statistical uncertainties (bars) are shown as well as total systematic uncertainties (hollow boxes) and systematic uncertainties uncorrelated across multiplicity (shaded boxes). A few model predictions are also shown as lines at their appropriate abscissa.

1353    **6.3 Integrated yield ratios to pion**

1354    The integrated yield ratios of excited hyperons to pions are shown in Figure 57 to study  
1355    the evolution of relative strangeness production yields with increasing collision system  
1356    size. The ratio of  $\Xi(1530)^0$  to  $\Xi$  is observed to be increase from pp to p–Pb collisions  
1357    system and then, decrease from peripheral to central Pb–Pb collision. The QCD-inspired  
1358    predictions like PYTHIA for pp [54] and DPMJET for p–Pb [47] clearly underestimate  
1359    the observed yield ratios, while the statistical one seems to be comparable with results  
1360    from high multiplicity in p–Pb but the ratio in Pb–Pb is below with respect to the model.  
1361    The results in pp and p–Pb collisions are consistent with previous observation of ground-  
1362    state hyperons to pion ratios. The Figure 58 presents particle yield ratios to pions of  
1363    strange and multi-strange hadrons normalized to the values measured in pp collisions. As  
1364    shown in the Figure 58, the  $\Xi(1530)^0$  to pion ratios follow the trend of  $\Xi \pi$  as function of  
1365     $\langle dN_{ch}/d\eta_{lab} \rangle$  and indicate that the strangeness enhancement observed in p–Pb collisions  
1366    depends predominantly on the strangeness content, rather than on the hyperon mass.

1367    The Figure 59 also shows the hyperon-to-pion ratios and compared with model predic-  
1368    tions. The

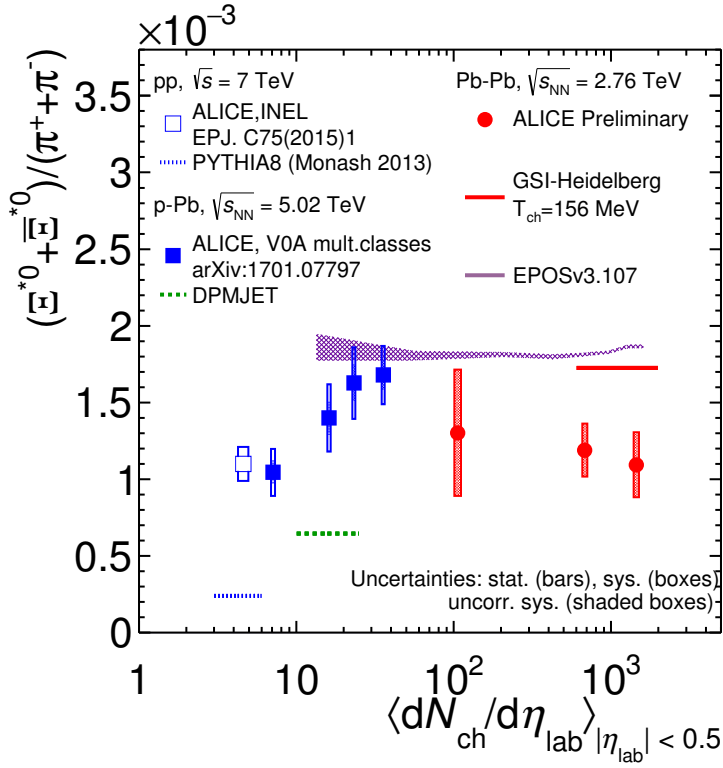


Figure 57: Ratio of  $\Xi(1530)^0$  to  $\pi^\pm$ , measured in pp [12] and p–Pb [8] collisions, as a function of the average charged particle density ( $\langle dN_{ch}/d\eta_{lab} \rangle$ ) measured at mid-rapidity. Statistical uncertainties (bars) are shown as well as total systematic uncertainties (hollow boxes) and systematic uncertainties uncorrelated across multiplicity (shaded boxes). A few model predictions are also shown as lines at their appropriate abscissa.

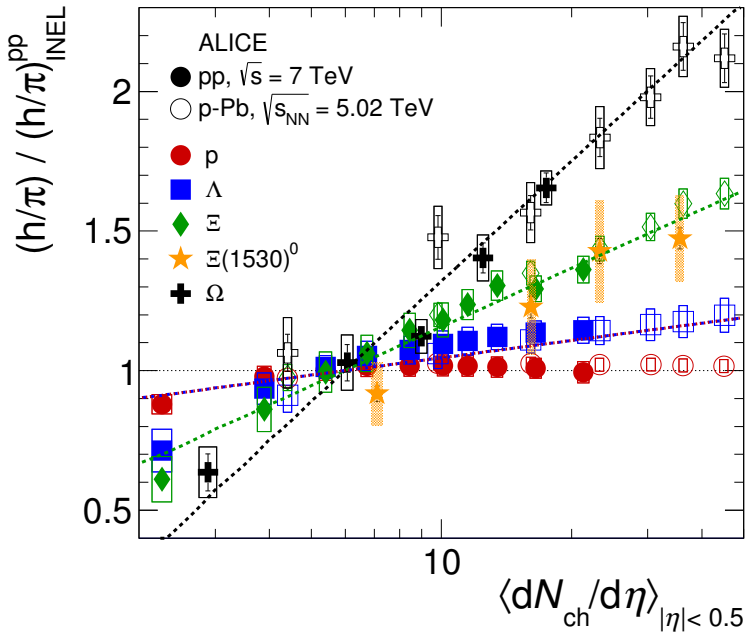


Figure 58: Particle yield ratios to pions of strange and multi-strange hadrons normalized to the values measured in  $pp$  collisions, both in  $pp$  and in  $p$ -Pb collisions. The common systematic uncertainties cancel in the double-ratio. The empty boxes represent the remaining uncorrelated uncertainties. The lines represent a simultaneous fit of the results with the empirical scaling formula in Equation ??.

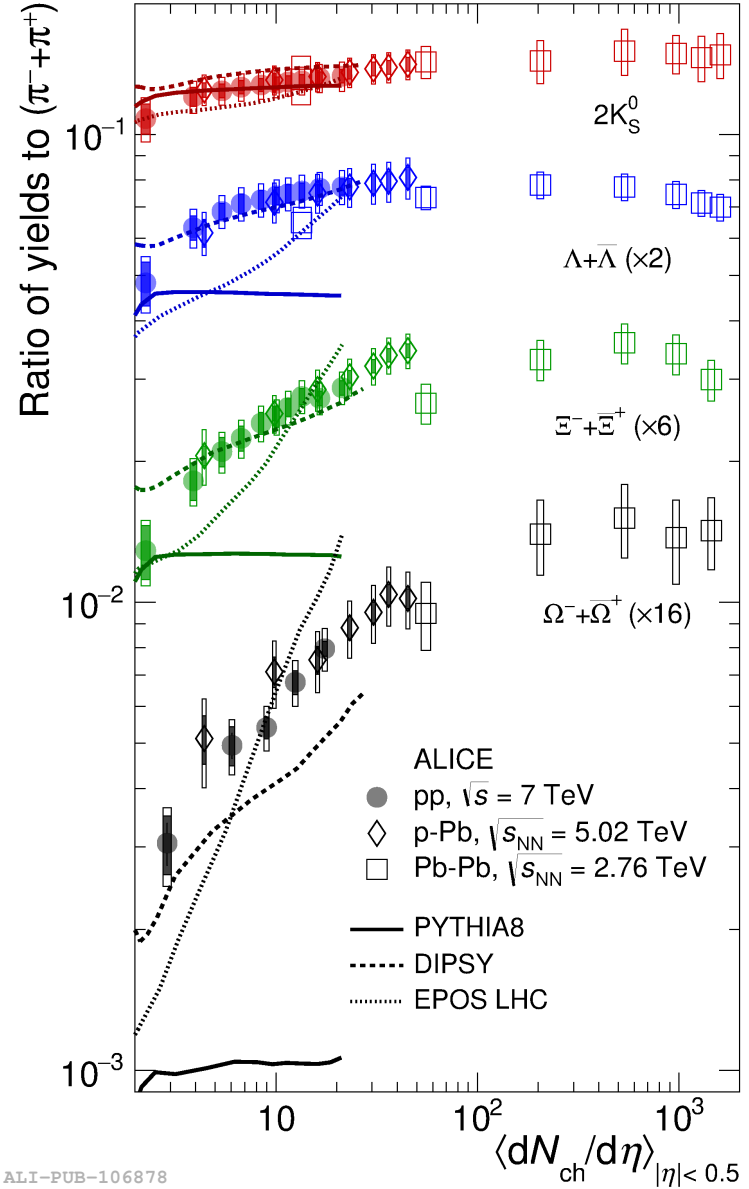


Figure 59:  $p_T$ -integrated yield ratios of strange and multi-strange hadrons to  $(\pi^+ + \pi^-)$  as a function of  $\langle dN_{ch}/d\eta_{lab} \rangle$  measured in the rapidity interval  $|\eta| < 0.5$ . The empty and dark-shaded boxes show the total systematic uncertainty and the contribution uncorrelated across multiplicity bins, respectively. The values are compared to calculations from MC models and to results obtained in Pb–Pb and p–Pb collisions at the LHC.

1369 **References**

- 1370 [1] **Particle Data Group** Collaboration, K. Olive *et al.*, “Review of Particle Physics,”  
1371 *Chin. Phys. C* **38** (2014) 090001.
- 1372 [2] P. Braun-Munziger, “Chemical equilibration and the Hadron-QGP phase transition,”  
1373 *In Nuclear Physics A* **681** (2001) 119–123.
- 1374 [3] “TE-EPC-LPC LHC units,”.  
1375 <http://te-epc-lpc.web.cern.ch/te-epc-lpc/machines/lhc/general.stm>.
- 1376 [4] **ALICE** Collaboration, K. e. a. Aamodt, “Alignment of the ALICE Inner Tracking  
1377 System with cosmic-ray tracks,” *JINST* **5** (2010) P03003.
- 1378 [5] **ALICE** Collaboration, J. Adam *et al.*, “Multiplicity dependence of pion, kaon,  
1379 proton and lambda production in p–Pb collisions at  $\sqrt{s_{NN}} = 5.02$  TeV,” *Phys. Lett.*  
1380 **B728** (2014) 25–38, [arXiv:1307.6796 \[nucl-ex\]](https://arxiv.org/abs/1307.6796).
- 1381 [6] **ALICE** Collaboration, J. Adam *et al.*, “Production of  $K^*(892)^0$  and  $\phi(1020)$  in  
1382 p–Pb collisions at  $\sqrt{s_{NN}} = 5.02$  TeV,” *Eur. Phys. J.* **C76** (2016) 245,  
1383 [arXiv:1601.7868 \[nucl-ex\]](https://arxiv.org/abs/1601.7868).
- 1384 [7] **ALICE** Collaboration, J. Adam *et al.*, “Multi-strange baryon production in p–Pb  
1385 collisions at  $\sqrt{s_{NN}} = 5.02$  TeV,” *Phys. Lett.* **B758** (2016) 389–401,  
1386 [arXiv:1512.07227 \[nucl-ex\]](https://arxiv.org/abs/1512.07227).
- 1387 [8] **ALICE** Collaboration, B. Abelev *et al.*, “Production of  $\Sigma(1385)^{\pm}$  and  $\Xi(1530)^0$  in  
1388 proton-proton collisions at  $\sqrt{s} = 7$  TeV,” *Eur. Phys. J.* **C75** (2015) 1,  
1389 [arXiv:1406.3206 \[nucl-ex\]](https://arxiv.org/abs/1406.3206).
- 1390 [9] **ALICE** Collaboration, J. Adam *et al.*, “ $D$ -meson production in p–Pb collisions at  
1391  $\sqrt{s_{NN}} = 5.02$  TeV and in pp collisions at  $\sqrt{s} = 7$  TeV,” *Phys. Rev. C* **94** (2016)  
1392 054908, [arXiv:1605.07569 \[nucl-ex\]](https://arxiv.org/abs/1605.07569).
- 1393 [10] **ALICE** Collaboration, B. Abelev *et al.*, “Inclusive  $J/\psi$  production in pp collisions  
1394 at  $\sqrt{s} = 2.76$  TeV,” *Phys. Lett.* **B718** (2012) 295–306, [arXiv:1203.3641 \[hep-ex\]](https://arxiv.org/abs/1203.3641).
- 1395 [11] **ALICE** Collaboration, J. Adam *et al.*, “Rapidity and transverse-momentum  
1396 dependence of the inclusive  $J/\psi$  nuclear modification factor in p–Pb collisions at  
1397  $\sqrt{s_{NN}} = 5.02$  TeV,” *JHEP* **06** (2015) 55, [arXiv:1503.07179 \[nucl-ex\]](https://arxiv.org/abs/1503.07179).
- 1398 [12] **ALICE** Collaboration, J. Adam *et al.*, “Measurement of pion, kaon and proton  
1399 production in proton-proton collisions at  $\sqrt{s} = 7$  TeV,” *Eur. Phys. J.* **C75** (2015)  
1400 226, [arXiv:1504.00024 \[nucl-ex\]](https://arxiv.org/abs/1504.00024).

- 1401 [13] F. Halzen and A. Martin, “Quarks and Leptons: an introductory course in modern  
 1402 particle physics,” *By John Wiley and Sons* (1984) .
- 1403 [14] T. K. Nayak, “Heavy Ions: Results from the Large Hadron Collider,” *Pramana* **79**  
 1404 (2012) 719–735.
- 1405 [15] S. Wheaton, J. Cleymans, and M. Hauer, “THERMUS: A Thermal model package  
 1406 for ROOT,” *Comput. Phys. Commun.* **180** (2009) 84–106, [arXiv:hep-ph/0407174](https://arxiv.org/abs/hep-ph/0407174)  
 1407 [hep-ph].
- 1408 [16] S. O. T. P. K. W. H.J. Drescher, M. Hladik, “Parton-Based Gribov-Regge Theory,”  
 1409 *Phys. Rept.* **350** (2001) 93–289, [hep-ph/0007198](https://arxiv.org/abs/hep-ph/0007198).
- 1410 [17] T. P. M. B. K. M. K. Werner, Iu. Karpenko, “Event-by-event simulation of the  
 1411 three-dimensional hydrodynamic evolution from flux tube initial conditions in  
 1412 ultrarelativistic heavy ion collisions,” *Phys. Rev.* **C82** (2010) 044904.
- 1413 [18] I. K. T. P. K. Werner, B. Guiot, “Analyzing radial flow features in p-Pb and p-p  
 1414 collisions at several TeV by studying identified-particle production with the event  
 1415 generator EPOS3,” *Phys. Rev.* **C89** (2014) 064903.
- 1416 [19] K. Werner., “Analyzing radial flow features in p-Pb and p-p collisions at several TeV  
 1417 by studying identified-particle production with the event generator EPOS3,” *Phys.*  
 1418 *Rev. Lett.* **98** (2007) 152301.
- 1419 [20] S. B. et al., “Microscopic Models for Ultrarelativistic Heavy Ion Collisions,” *Prog.*  
 1420 *Part. Nucl. Phys.* **41** (1998) 255.
- 1421 [21] M. B. et al., “Relativistic Hadron-Hadron Collisions in the Ultra-Relativistic  
 1422 Quantum Molecular Dynamics Model,” *J. Phys.* **G25** (1999) 1859–1896.
- 1423 [22] M. Gell-Mann and Y. Ne’eman, “The Eightfold Way,” *By W.A. Benjamin* (1964) .
- 1424 [23] J. Rafelski and B. Mller, “Strangeness Production in the Quark-Gluon Plasma,”  
 1425 *Phys. Rev. Lett.* **48** (1982) 1066–1069.
- 1426 [24] **ALICE** Collaboration, B. Abelev *et al.*, “Multi-strange baryon production at  
 1427 mid-rapidity in Pb-Pb collisions at  $\sqrt{s_{\text{NN}}} = 2.76$  TeV,” *Phys. Lett.* **B728** (2014)  
 1428 216–227, [arXiv:1307.5543](https://arxiv.org/abs/1307.5543) [nucl-ex].
- 1429 [25] L. Evans and P. Bryant, “LHC Machine,” *JINST* **3** (2008) S08001.
- 1430 [26] “ALICE Technical Proposal,” *In CERN-LHCC-95-71* (1995) .
- 1431 [27] “ATLAS Technical Proposal,” *In CERN-LHCC-94-43* (1994) .

- 1432 [28] “CMS Technical Proposal,” *In CERN-LHCC-94-38* (1994) .
- 1433 [29] “LHCb Technical Proposal,” *In CERN-LHCC-98-004* (1998) .
- 1434 [30] “Technical Proposal for CERN LHCf Experiment,” *In CERN-LHCC-05-032* (2005) .
- 1435 [31] “Total Cross Section, Elastic Scattering and Diffraction Dissociation at the LHC,”  
1436 *In CERN-LHCC-99-007* (1999) .
- 1437 [32] **ALICE** Collaboration, K. Aamodt *et al.*, “The ALICE experiment at the CERN  
1438 LHC,” *JINST* **3** (2008) S08002.
- 1439 [33] **ALICE** Collaboration, L. B. et al, “Definition of the ALICE coordinate system and  
1440 basic rules for sub-detector components numbering,” *In Internal Note  
1441 ALICE-INT-2003-038* (2003) .
- 1442 [34] **ALICE** Collaboration, J. e. a. Alme, “The ALICE TPC, a large 3-dimensional  
1443 tracking device with fast readout for ultra-high multiplicity events,” *In Nuclear  
1444 Instruments and Method in Physics Research* **A622** (2010) 316–367.
- 1445 [35] “Technical Design Report on Forward Detectors: FMD, T0 and VZERO,” *In  
1446 CERN-LHCC-2004-025* (2004) .
- 1447 [36] R. Glauber, “Lectures in Theoretical Physics,” *By Interscience Publishers.* **1** (1959)  
1448 315.
- 1449 [37] A. S. K.C. Chung, C.S. Whang and G. Pech, “Transverse and forward energy  
1450 distributions in untra-relativistic heavy-ion collisions by an absorption model,”  
1451 *Physics Review* **C57** (1998) 847–856.
- 1452 [38] **ALICE** Collaboration, J. Adam *et al.*, “Centrality dependence of particle  
1453 production in p–Pb collisions at  $\sqrt{s_{\text{NN}}} = 5.02$  TeV,” *Phys. Rev.* **C91** (2015) 064905,  
1454 [arXiv:1412.6828 \[nucl-ex\]](https://arxiv.org/abs/1412.6828).
- 1455 [39] **ALICE** Collaboration, B. Abelev *et al.*, “Centrality determination of Pb–Pb  
1456 collisions at  $\sqrt{s_{\text{NN}}} = 2.76$  TeV with ALICE,” *Phys. Rev.* **C88** (2013) ,  
1457 [arXiv:1303.0737 \[nucl-ex\]](https://arxiv.org/abs/1303.0737).
- 1458 [40] “ALICE Technical Design Report of the Trigger, Data Acquisition, High-Level  
1459 Trigger, Control system,” *In CERN-LHCC-2003-062.* (2003) .
- 1460 [41] “The Grid - Blueprint for a New Computing Infrastructure,” *By Morgan Kaufmann  
1461 Publishers.* (1999) .
- 1462 [42] e. a. Bagnasco. S, “AliEn: ALICE Environment on the GRID,” *In Jounal of Physics:  
1463 Conference Series* **119** (2008) n.062012.

- 1464 [43] R. Brun and F. Rademakers, “ROOT - An object oriented data analysis framework,”  
 1465     *In Nuclear Instrument and Methods in Physics Research Section A* **389** (1997)  
 1466     81–86.
- 1467 [44] **ALICE** Collaboration, B. Abelev *et al.*, “Performance of the ALICE Experiment at  
 1468     the CERN LHC,” *Int. J. Mod. Phys. A* **29** (2014) 1430044, [arXiv:1402.4476](#)  
 1469     [nucl-ex].
- 1470 [45] **ALICE** Collaboration, B. Abelev *et al.*, “Pseudorapidity Density of Charged  
 1471     Particles in p–Pb Collisions at  $\sqrt{s_{\text{NN}}}= 5.02$  TeV,” *Phys. Rev. Lett.* **110** (2013)  
 1472     032301, [arXiv:1210.3615](#) [nucl-ex].
- 1473 [46] **ALICE** Collaboration, K. Aamodt *et al.*, “Strange particle production in  
 1474     proton-proton collisions at  $\sqrt{s}= 0.9$  TeV with ALICE at the LHC,” *Eur. Phys. J.*  
 1475     **C71** (2011) 1594, [arXiv:1012.3257](#) [nucl-ex].
- 1476 [47] S. Roesler, R. Engel, , and J. Ranft, “The Monte Carlo Event Generator  
 1477     DPMJET-III, Advanced Monte Carlo for Radiation Physics, Particle Transport  
 1478     Simulation and Applications,” *Conference Proceedings, MC2000, Lisbon, Portugal,*  
 1479     October 23–26 (2000) 1033–1038, [hep-ph/0012252](#).
- 1480 [48] R. Brun, F. Carminati, and S. Giani, “GEANT detector description and simulation  
 1481     tool,” *CERN-W5013* (1994) .
- 1482 [49] R. Barlow, “Systematic Errors: Facts and Fictions,” *Presented at Advanced*  
 1483     *Statistical Techniques in HEP, Durham, March 2002* (2002) 333p,  
 1484     [hep-ex/0207026v1](#).
- 1485 [50] **ALICE** Collaboration, B. Abelev *et al.*, “Centrality dependence of  $\pi$ ,  $K$  and  $p$   
 1486     production in Pb–Pb collisions at  $\sqrt{s_{\text{NN}}}= 2.76$  TeV,” *Phys. Rev. C* **88** (2013) ,  
 1487     [arXiv:1301.4361](#) [nucl-ex].
- 1488 [51] **STAR** Collaboration, B. I. Abelev *et al.*, “Hadronic resonance production in d–Au  
 1489     collisions at  $\sqrt{s_{\text{NN}}}= 200$  GeV measured at the BNL Relativistic Heavy-Ion Collider,”  
 1490     *Phys. Rev. C* **78** (2008) 044906, [arXiv:0801.0450](#) [nucl-ex].
- 1491 [52] A. Velásquez, “Mean  $p_{\text{T}}$  scaling with  $m/n_q$  at the LHC: Absence of (hydro) flow in  
 1492     small systems?,” *Nucl. Phys. A* **943** (2015) 9–17, [arXiv:1506.00584](#) [hep-ph].
- 1493 [53] **ALICE** Collaboration, B. Abelev *et al.*, “Multi-strange baryon production in pp  
 1494     collisions at  $\sqrt{s}= 7$  TeV with ALICE,” *Phys. Lett. B* **712** (2012) 309,  
 1495     [arXiv:1204.0282](#) [nucl-ex].
- 1496 [54] T. Sjöstrand, S. Mrenna, and P. Skands, “A brief introduction to PYTHIA 8.1,”  
 1497     *Comput. Phys. Comm.* **178** (2008) 852–867, [arXiv:0710.3820](#) [hep-ph].

<sup>1498</sup> **Acknowledgements**